Differentiating Top-Quark - Photon Coupling: Inclusive and Differential Cross-Section Measurements of Top-Quark Pair Production in Association with a Photon in the Single Lepton Channel in pp Collisions Data at $\sqrt{s} = 8\,\text{TeV}$ with the ATLAS Experiment

DISSERTATION
zur Erlangung des Grades eines Doktors
der Naturwissenschaften
"Doctor rerum naturalium"
der Naturwissenschaftlich-Technischen Fakultät
der Universität Siegen

vorgelegt von
Naim Bora Atlay, M.Sc.
aus Mersin

Siegen, 2017

Referent:	Prof. Dr. rer. nat. Ivor Fleck, Universität Siegen
Koreferent:	Prof. Dr. rer. nat. Kevin Kröninger, Technische Universität Dortmund
Weitere Prüfer:	
Prüfer:	Prof. Dr. rer. nat. Claus Grupen, Universität Siegen
Prüfer:	Prof. Dr. rer. nat. Wolfgang Kilian, Universität Siegen

Datum der Disputation	13. Juli 2017

Gedruckt auf alterungsbeständigem holz- und säurefreiem Papier.

Inclusive and Differential Cross Section Measurements of Top-Quark Pair Production in Association with a Photon in the Single Lepton Channel in pp Collisions Data with a Luminosity 20.2 fb^{-1} at $\sqrt{s} = 8$ TeV with the ATLAS Experiment

by Naim Bora Atlay, M. Sc.

Abstract

This thesis presents measurements of inclusive and differential production cross sections of top- anti-top-quark pairs in association with an additional prompt photon ($t\bar{t}\gamma$) in the single lepton final state at the LHC analysing data recorded by the ATLAS detector. The data analysed corresponds to 20.2 fb−1 of integrated luminosity recorded during 2012 at a center-of-mass energy of $\sqrt{s} = 8$ TeV. The cross.section is measured with a template fit method. Background processes are estimated with data driven and Monte Carlo based methods. The differential cross section is measured as a function of transverse momentum and pseudo-rapidity of the photon. A total of 1256 and 1816 candidate $t\bar{t}\gamma$ events are observed in the electron and muon channel, respectively. Both inclusive and differential measurements are performed in a fiducial phase space within the detector acceptance. The differential measurements are performed as a function of transverse momentum and pseudo-rapidity of the photon. The inclusive $t\bar{t}\gamma$ production cross section times the branching ratio (BR) is measured to be

$$\sigma_{t\bar{t}\gamma} \times \mathrm{BR} = 71.4 \pm 13.0 \text{ fb}$$

in the electron channel. The measured cross section in the muon channel reads

$$\sigma_{t\bar{t}\gamma} \times \mathrm{BR} = 70.0 \pm 9.8 \text{ fb}.$$

The results are in agreement within the uncertainties with the corresponding standard model predictions at next-to-leading order.

Messungen der inklusiven und differentiellen Wirkungsquerschnitte der Entstehung des Top-Quark-Paares unter Photonbeteiligung im Einzel-Leptonen-Kanal bei einer Schwerpunktsenergie von $\sqrt{s} = 8\,\text{TeV}$ mit $20.3\,\text{fb}^{-1}$ von Proton-Proton Kollisions-Daten aufgezeichnet vom ATLAS Detektor

von M.Sc. Naim Bora Atlay

Zusammenfassung

Die Messungen der inklusiven und differentiellen Wirkungsquerschnitte der Entstehung eines Top-Quark-Paares unter Abstrahlung eines zusätzlichen Photons ($t\bar{t}\gamma$) im Einzel-Leptonen-Kanal wird vorgestellt. Die Messungen wurden mit Hilfe einer Template-Fit-Methode unter Verwendung eines Datensatzes mit einer integrierten Luminosität von $20.2\,\text{fb}^{-1}$ von Proton-Proton Kollisions-Daten aufgezeichnet vom ATLAS Detektor durchgeführt. Die Messung der differentiellen Wirkungsquerschnitte wurde als Funktion von transversalem Impuls und Pseudo-Rapidät des Photons durchgeführt. Verschiedene Untergrund-Beiträge wurden mit datengestützten Verfahren oder mit der Hilfe von Monte-Carlo-Daten untersucht. Es wurden insgesamt 1256 $t\bar{t}\gamma$-Kandidaten im Elektron- und 1816 Kandidaten im Myon-Kanal beobachtet. Die Messung des inklusiven Wirkungsquerschnitts liefert ein Ergebnis von

$$\sigma^{\text{fid}}_{t\bar{t}\gamma} \times \text{BR} = 71.4 \pm 13.0 \text{ fb}$$

für das Elektron-Kanal und

$$\sigma^{\text{fid}}_{t\bar{t}\gamma} \times \text{BR} = 70.0 \pm 9.8 \text{ fb}$$

für das Myon-Kanal. Die Messungen sind in guter Übereinstimmung mit theoretischen Vorhersagen im Rahmen der experimentellen und theoretischen Unsicherheiten.

I may be wrong and you may be right,
and by an effort, we may get nearer to the truth [1].

Contents

List of Figures

List of Tables

Chapter 1

Introduction

In 1995, collaborations of the two experiments at Tevatron, CDF and D0, announced the discovery of long-awaited but well expected missing piece of the Standard Model (SM), the top-quark [2, 3]. The particle was theorised in 1964 to explain charge-parity violation in Kaon decays [4]. Its experimental observation, however, had to wait for a long time. The reason was to this long wait is its enormous mass. A collider with a collision energy strong enough to produce such a heavy particle was not achieved before Tevatron. This high mass of the top-quark was an obstacle in front of its discovery but it's the very same feature that makes the top-quark a quite versatile particle for the test of the SM.

The high mass of the top-quark is a consequence of its strong Yukawa coupling to the Higgs boson and because of this strong coupling, the top-quark is believed to be an important actor in the *Electroweak Symmetry Breaking* (EWSB). The high mass of the top-quark leads to another interesting feature: Due to this high mass, the top-quark has an extremely short lifetime (i.e. $\sim 10^{-25}$ s) which makes the top-quark the only "*free*" quark since its lifetime is shorter than the QCD hadronisation scale. Namely, all quarks of the SM except for the top-quark form bound-states due to *QCD confinement* immediately after their production while the top-quark decays before it hadronises. This is a very profitable feature because investigation of the decay products of the top-quark provides a lot of information, since its all properties are passed to the decay products through its decay.

However, although the discovery of the top-quark will be a quarter century old in a couple of years, some of its properties are still waiting to be fully understood, such as top quark's couplings to the vector bosons. Among these couplings, the coupling to the photon, which is subject of this thesis, is of importance for setting constrains on the models hypothesising composite top-quarks [5] or excited top-quarks, i.e. $t^* \to t\gamma$. Any deviation from the SM prediction of this coupling, i.e. $t\gamma$ vertex, would imply hints for new physics beyond the SM (BSM). Theoretical works [6, 7, 8] on anomalous couplings of the top-quark predict deviations from the SM.

The first step in to understanding of the $t\gamma$ vertex starts with the cross-section measurement of processes with the $t\gamma$ vertex. Top-quark pair ($t\bar{t}$) production with an additional photon in the final state is one of these processes. Although it is experimentally impossible to isolate events with a true $t\gamma$ vertex, the measurement presented here attempts to select events with $t\gamma$ vertex and measure a cross-section of this process. The most recent result on the $t\bar{t}\gamma$ cross-section is published by ATLAS [9]. The measurement presented here is in parallel with the latest result, since I was also a member of the

analysis team at the time of writing this thesis. The measurement presents both an inclusive and differential, as a function of photon transverse momentum and pseudo-rapidity, cross-section measurements in a certain fiducial phase space. A number of cross-section measurements of this process have been performed with both 7 TeV and 8 TeV collisions data by the ATLAS and CMS collaborations [10, 11].

The next chapter provides an overview of the top-quark. The third chapter delivers the description of the ATLAS detector, the experimental setup used to collect the data analysed. The following chapter gives the definition of physical objects which is then followed by the description of selection used to select the signal events. The strategy of the analysis given in chapter 6. The strategy is followed by the core of the analysis, the template fit measurement extracting the cross section, in chapter 7. The systematics uncertainties and the results are given in chapters 8 and 10, respectively. The thesis then concludes with a summary.

Note the natural units, i.e. $\hbar = c = 1$, and the electron(or proton) electric charge, i.e. $e = \pm 1$, throughout the thesis.

Chapter 2

The top-quark at hadron colliders

The brief theoretical and experimental overviews of the top-quark given in this chapter are based on the successfully established Standard Model of particle physics.

2.1 Top-quark production

The production of the top-quarks at hadron colliders, either as single quarks or as quark-anti-quark pairs, occurs through two of the three interactions of the SM: electroweak and strong interactions. Example Feynman diagrams representing these two kinds of production processes are presented in figures 2.3 and 2.2. The single production is suppressed at hadron colliders and shortly summarised in section 2.1.2.

2.1.1 Pair production of top-quarks

Pair production of top-quarks is possible via two different processes in terms of ingoing particles: quark-anti-quark($q\bar{q}$) annihilation and gluon-gluon(gg) fusion. At the LHC, as it is a proton-proton collider, the $q\bar{q}$-annihilation is suppressed since anti-quarks are present only as *sea-quarks*. Representative Feynman diagrams are presented in figure 2.2.

Unlike lepton collisions, where the colliding particles are point-like particles, hadron collisions are interactions of their constituents. A proton is a quite complex object consisting of three *valance quarks*(uud), gluons binding the valence quarks together and the *sea-quarks* from the splitting of the gluons. The total momentum of a proton is distributed between these constituents and therefore each carries only a fraction of the total momentum. A distribution of momentum fractions carried by constituents of a proton is presented in figure 2.1. As a consequence, hadron collisions are essentially a bunch of interactions carrying different fractions of momenta. Hadron collisions can be, therefore, factored into collisions of partons carrying high momentum, i.e. hard interaction or scattering, and of partons carrying low momentum, i.e. soft interactions. The physics of hadron collisions is therefore described by perturbative QCD, where the collisions are factored into perturbative and non-perturbative terms by the so-called factorisation scale. Therefore, the inclusive cross-section for top-quark pair production at a pp-collider can be expressed as follows [13]:

$$\sigma^{pp\to t\bar{t}}(s, m_t) = \sum_{i,j=q,\bar{q},g} \int dx_i dx_j f_i(x_i, \mu_F^2) f_j(x_j, \mu_F^2) \cdot \hat{\sigma}^{ij\to t\bar{t}}(\hat{s}, m_t, \mu_F^2, \mu_R^2, \alpha_s). \quad (2.1)$$

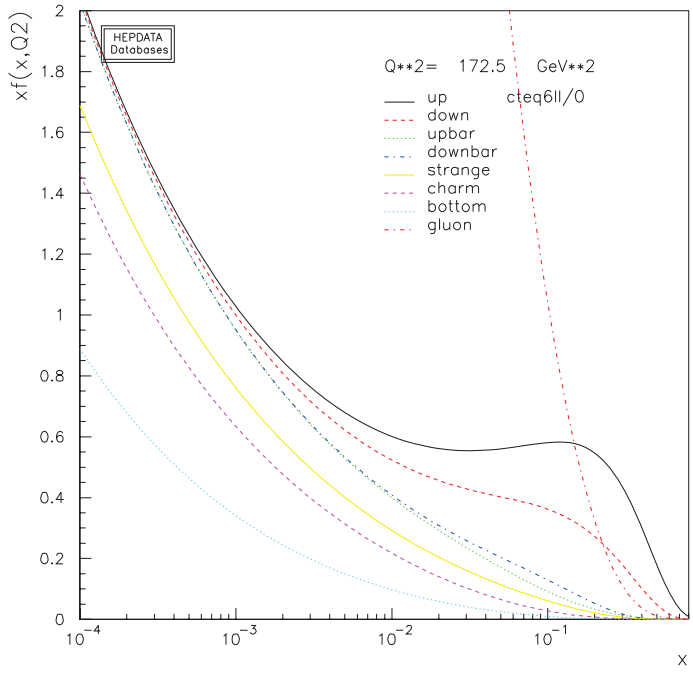

Figure 2.1.: Parton density functions of all partons as a function of the fractional proton momentum for the the dataset CTEQ6L1 at the energy of top mass, i.e. $Q = m_t = 172.5$ GeV. The gluons dominate the parton distribution functions up to high x, while at the region close to x=1 valance quarks becomes dominant what consequently makes the $t\bar{t}$ production via $q\bar{q}$ annihilation dominant at Tevatron. At the LHC, however, since the gluons dominant up to high x and since anti-quarks exist only as sea-quarks, $t\bar{t}$ production via gg fusion is becomes dominant. [12]

The cross-section depends on the center-of-mass energy squared of the collider, $s{=}4E^2_{beam}$, and on the top-quark mass, m_t. The sum considers all contributing quarks and gluons. $f_{i(j)}(x_{i(j)}, \mu_F^2)$ are the proton *parton distribution functions* (PDFs), each of which is a function of the momentum fraction carried by the parton $x_{i(j)}$ and of the factorisation scale μ_F. The partonic cross-section at the LO, $\hat{\sigma}^{ij\to t\bar{t}}$ depends on the partonic center-of-mass energy, $\hat{s} = x_i x_j s$, m_t, μ_F, renormalisation scale, μ_R, and the strong coupling constant, α_s. The dependence of the partonic cross-section and the PDF on μ_F arises from absorbing uncanceled collinear initial state singularities into the PDF. The dependence on μ_R of the partonic cross-section, computed in truncated perturbation theory, arises in particular from the definition of the renormalised coupling α_s, which is usually done in the $\overline{MS}$-scheme [13]. Theoretical works for the top-quark pair production are available at NNLL and NNLO [14, 15, 16, 17, 18]. Representative Feynman diagrams of the top-quark pair production processes are presented in figure 2.2.

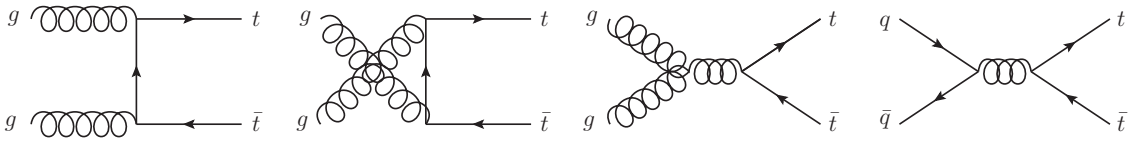

Figure 2.2.: Representative Feynman diagrams for $t\bar{t}$ production at the LO order QCD (α_s^2).

2.1.2 Single production of top-quarks

Single top-quarks are produced through the electroweak interaction. The single production occurs almost exclusively through Wtb vertex and in three modes:
t-channel: This mode occurs via scattering of a space-like W-boson and bottom-quark.
s-channel: In this mode, the quark and the anti-quark of one of the first two isospin-doublet generations annihilate into a time-like W-boson that subsequently decays into a tb-pair.
Wt-channel: This mode is an associated sort of production where the top-quark is produced together with a real W-boson.
An example Feynman diagram representing each production channel is presented in figure 2.3.

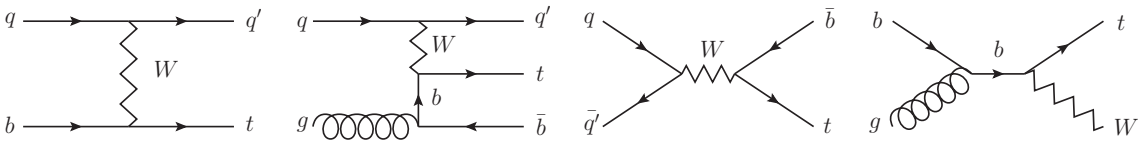

Figure 2.3.: Representative Feynman diagrams for single top-quark production at leading order QCD. From the left, the first two diagram represents the t-channel production as flavour excitation and as W-gluon fusion respectively. The third diagram is the s-channel production and the last one is the Wt-channel production.

2.2 Top-quark decay

The top-quark decays almost exclusively (99.8%) into a W-boson and a bottom-quark. Decay of the top-quark into a $W-boson$ and a down-quark or a strange-quark is strongly excluded by the CKM matrix elements $V_{td} = 0.00359 \pm 0.00016$ and $V_{ts} = 0.0415^{+0.0010}_{-0.0011}$ [19]. The total decay width of the top-quark at NLO excluding the $t \to W(d,s)$ decays is expressed by the following expression [13]:

$$\Gamma_t = \frac{G_F m_t^3}{8\pi\sqrt{2}} |V_{tb}|^2 \left(1 - \frac{m_W^2}{m_t^2}\right)^2 \left(1 + 2\frac{m_W^2}{m_t^2}\right) \left[1 - \frac{2\alpha_s}{3\pi}\left(\frac{2\pi^2}{3} - \frac{5}{2}\right)\right], \tag{2.2}$$

with the Fermi coupling constant, $G_F = 1.16637 \times 10^{-5}$ GeV^{-2}, the W boson mass m_W, and the top mass m_t. With m_t=172.5 GeV, the width is calculated to be Γ_t=1.33 GeV and this large decay width corresponds to the aforementioned very short lifetime, $\tau_t = 1/\Gamma_t \sim 10^{-25}$ s which is shorter than the QCD hadronisation time (Λ_{QCD}), i.e., $\tau_{had} \sim 1$ fm$/c \sim 3 \cdot 10^{-24}$ s. This implies that the top-quark decays before it gets confined in a *toponium* bound-state by passing its spin information to its daughter particles. Additionally, this also enables the possibility of studying the polarisation of the W-boson from the top-quark.

Depending on the further decay of the daughter W-boson, the decay channels of the top-quark pair production are categorised into three channels as follows:
Hadronic channel ($t\bar{t} \to W^+bW^-\bar{b} \to q\bar{q}'bq''\bar{q}'''b$): Both daughter W-bosons decay hadronically. This leads to a final state with up to six jets which makes the analyses of this channel a great challenge since it is quite an effort to distinguish between this final state and multi-jet environment of a pp-collider. The branching ratio of this channel is 46.2%.
Dileptonic channel ($t\bar{t} \to W^+bW^-\bar{b} \to \bar{l}\nu_l b l'\bar{\nu}_{l'}\bar{b}$): Both daughter W-bosons decay leptonically into a lepton-neutrino pair. In contrast to the hadronic channel, this final state is a very clean signal with two b-jets, yet the branching ratio of this channel (dilepton: e, μ, τ) is very small, 10.3%. Considering only the first two lepton generations, the branching ratio goes down to 6.45%. The existence of two neutrinos in the final state and low statistics due to the small branching ratio are drawbacks of this channel.
Semileptonic channel ($t\bar{t} \to W^+bW^-\bar{b} \to q\bar{q}'bl\bar{\nu}_l\bar{b} + \bar{l}\nu_l bq\bar{q}'\bar{b}$): One of the daughter W-bosons decays hadronically while the other decays leptonically. The branching ratio, considering all lepton generations, is almost as high as the hadronic channel, 43.5%, and the presence of a high-p_T lepton together with a high missing transverse energy makes this channel more distinctive in comparison to the other two channels. Indeed, most of the analyses of top pair production are performed in this channel including this thesis. A representative Feynman diagram of this decay channel can be seen in figure 2.4. A pie-chart of the branching ratios of the top-quark pair decay is presented in figure 2.5.

2.3 Top-quark properties

2.3.1 Mass

The mass of the top-quark, as all other fermion masses are, is one of the free parameters of the SM. A combination of direct measurements of its mass from the two experiments, Tevatron and the LHC, is measured to be 173.34±0.76 GeV [21]. This uncertainty corresponds to a precision of 0.44%. The top-quark is not only the heaviest particle but also the particle with the most precise mass measurement. Figure 2.6 presents a collection of

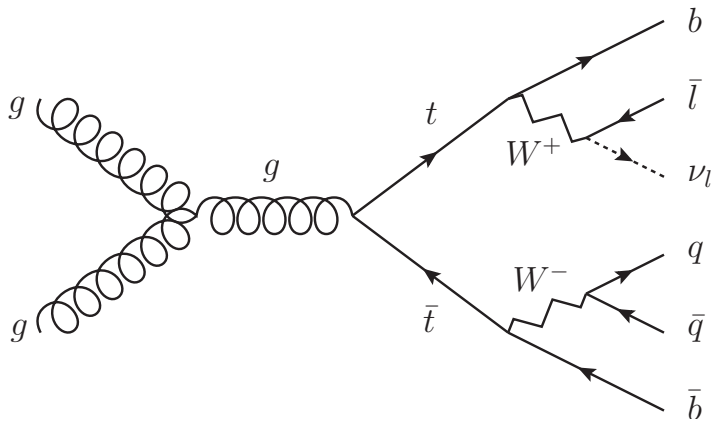

Figure 2.4.: A representative feynman diagram for the semileptonic decay channel of a $t\bar{t}$ pair.

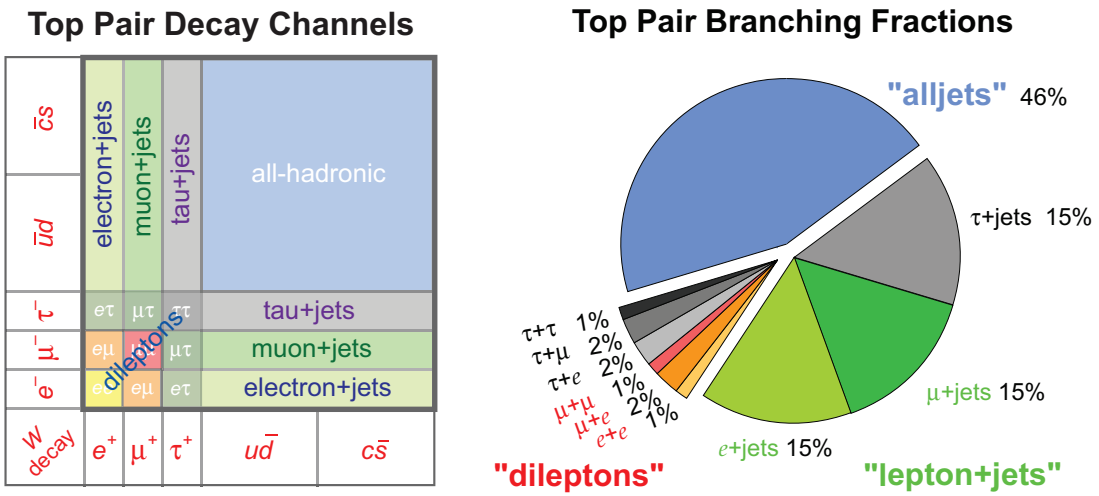

Figure 2.5.: The top-quark pair decay channels and a pie chart representing the top-quark decay branching fractions. The $t\bar{t}$ decay is categorised by the decay particles of the W-boson into three channels as: hadronic, semileptonic or lepton+jets and dileptonic channels [20].

top-quark mass measurements performed by the ATLAS and CMS collaborations as well as a world combination result (i.e. combinations of ATLAS, CMS, CDF, and D0 collaborations) from March 2014. Apart from the direct measurement of the top-quark mass,

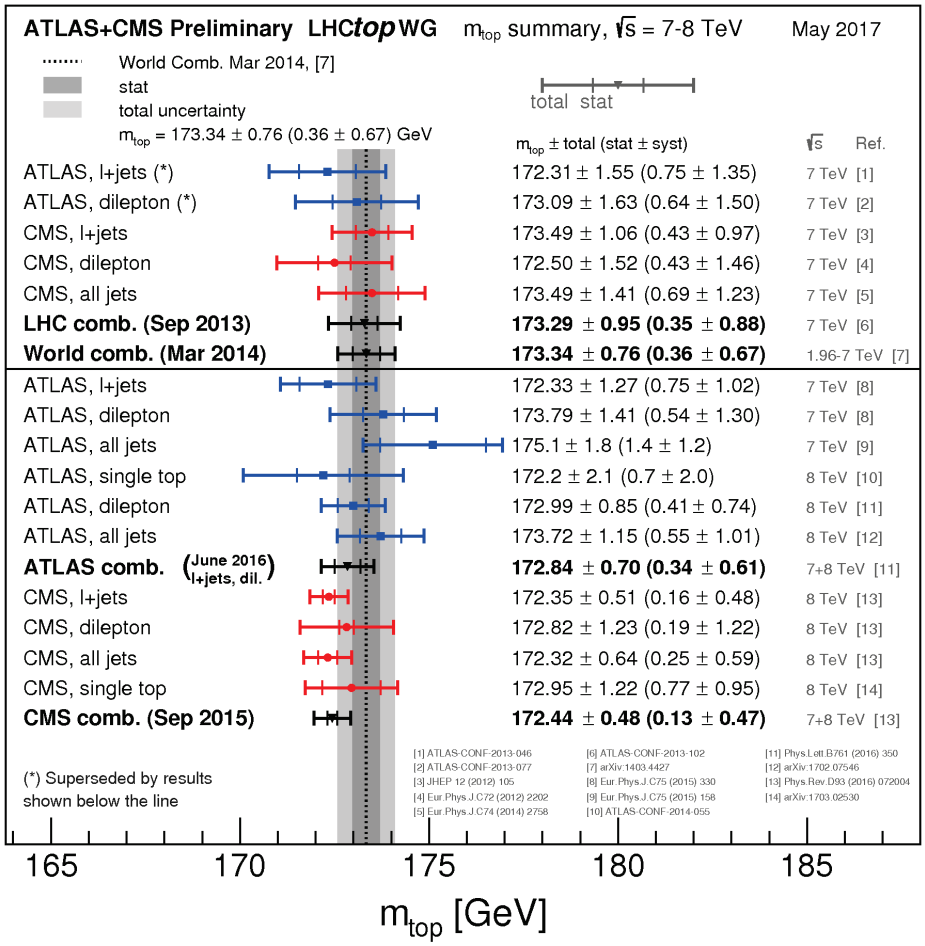

Figure 2.6.: Summary of the ATLAS and CMS direct m_{top} measurements. The results are compared with the LHC and Tevatron+LHC m_{top} combinations. For each measurement, the statistical uncertainty, the jet scale factor (JSF) and b-jet scale factor (bJSF) contributions (when applicable) as well as the sum of the remaining uncertainties are reported separately. The JSF, bJSF contributions are statistical in nature and apply to analyses performing in-situ (top quark pair base) jet energy calibration procedures. The results below the line are results produced after the LHC and Tevatron+LHC combinations were performed. [22]

indirect constraints on the top-quark mass are possible by measuring the parameters of the electroweak theory. The mass of the W-boson can be written in terms of other quantities of the electroweak theory [23]:

$$m_W^2 = \frac{\pi\alpha}{sin^2\theta_W\sqrt{2}G_F(1-\Delta r)} \tag{2.3}$$

where α is the electromagnetic coupling, $\sin^2\theta_W = (1-m_W^2/m_Z^2)$ and finally Δr represents contributions from higher order EW loop diagrams. The Δr include contributions from the top-quark and bottom-quark loops as well as loops involving Higgs boson in the W-boson propagator. The top-quark loops contributing to Δr depend quadratically on m_t. As a consequence, precision measurements of the these EW parameters could set constraints on top-quark mass. A recent measurement for an indirect constrain is performed by a group of several collaborations and is found to be $m_t = 179^{+11.7}_{-8.7}$ GeV [24]. Fits to the EW parameters can also be used to put indirect constrains on the Higgs boson mass exploiting the direct precise measurement of the top-quark mass.

Another inference which could be inferred by the measurement of top-quark mass is the violation of CPT(Charge-Parity-Time) symmetry [25]. Namely, a difference between the mass of the top-quark and anti-top-quark would indicate the violation of CPT symmetry. Direct measurement of $t-\bar{t}$ mass difference is possible since top-quark has a very short lifetime. The latest $t-\bar{t}$ mass difference measurement performed by the ATLAS experiment shows that the difference is $\Delta m = m_t - m_{\bar{t}} = 0.67 \pm 0.61(stat.) \pm 0.41(syst.)$GeV [26] which is consistent with the CPT invariance.

2.3.2 Electric charge

The SM predicts the electric charge of the top-quark is to be $+2/3e$ as it is the isospin partner of the b-quark. The electric charge of the top-quarks is proportional its electromagnetic coupling, e.g., $t\gamma$ vertex. This makes the precise measurement of top-quark electric charge an important tool to rule out its anomalous couplings [27]. Precise measurement of top-quark charge is important, since indirect measurement of the top-quark charge is possible by measuring the charges of its decay products. Dileptonic and semileptonic decay channels of the top-quark are preferred for this measurement since the charge is dissolved into jets during hadronisation in the hadronic channel. The hypothesis suggesting an exotic charge of -4/3e is excluded by measurements at Tevatron at 95% confidence level [28, 29], as well as at the ATLAS experiment [30].

2.3.3 R parameter

The decays of the top-quark into a W-boson and a quark of either the first or the second generation isospin doublets are suppressed by the CKM matrix [4, 31] elements: $t \to Ws$(BR$\sim$0.2%) and $t \to Wd$(BR$\sim$0.005%). As a consequence, the value of the quantity R,

$$R = \frac{\mathrm{BR}(t \to Wb)}{\mathrm{BR}(t \to Wq)} \tag{2.4}$$

is predicted to be nearly 1. A deviation from this value would be an indication of a fourth generation isospin doublet and a measurement [32] from the D0 collaboration yielded a value smaller than unity by 2.5 standard deviations.

2.3.4 Spin correlation

As pointed out earlier in this chapter, the spin information of the top-quark is passed to its decay products through its decay. This enables the measurement of the spin correlation between the top- and anti-top-quark exploiting the angular correlation of their decay products. Once again, deviations from the angular distributions predicted by the SM would indicate new physics. In the SM, the angular distributions of the decay products

of a polarised sample of top-quarks are described by the following formula:

$$\frac{1}{N}\frac{dN}{d\cos(\theta_i)} = \frac{1}{2}(1 + \alpha_i \cos(\theta_i)), \tag{2.5}$$

where θ_i is the angle between the direction of the decay particle in the top-quark rest frame and the spin quantisation direction, and α_i is a coefficient expressing the spin analysing power of the decay particle. The values of α_i for the charged leptons and down-type quarks are close to 1 what makes them the most effective spin analysers. But since it is a quite difficult task to distinguish between up- and down-type quarks experimentally, the dilepton decay channel is the preferred option for the spin correlation measurement.

In order to quantify the spin correlation, a coefficient is defined which is the ratio of the difference of $t\bar{t}$ events, where the spins of the top-quarks are aligned, to those, where they have opposite alignment for a given frame of reference. The coefficient is described as:

$$A = \frac{N(\uparrow\uparrow) + N(\downarrow\downarrow) - N(\uparrow\downarrow) - N(\downarrow\uparrow)}{N(\uparrow\uparrow) + N(\downarrow\downarrow) + N(\uparrow\downarrow) + N(\downarrow\uparrow)}. \tag{2.6}$$

The parameter A depends on the reference direction that is used to define the spin direction of the top- and anti-top-quark, conventionally referred to as spin-analysing-basis. A measurement performed by the ATLAS collaboration [33] presented that the correlation coefficient parameter,$A = 0.38 \pm 0.04$, to be in agreement with the SM prediction.

2.3.5 W-polarisation

Another consequence of top-quark's almost exclusive decay into a W-boson and b-quark is the opportunity to study the $t \to Wb$ vertex by measuring the polarisation of the W-boson. The top-quark decays through the weak interaction with a $V - A$ structure where $V(A)$ is the vector (axial vector) contribution to the vertex. In top-quark decay, the polarisation of the W-boson can be either longitudinal(i.e. helicity = 0), or left- or right-handed (helicity=$\pm$1) with the corresponding partial widths, $\Gamma_{0,R,L}$. However, neglecting the b-quark mass, Γ_R should be zero at tree level. The helicity fractions, $F_i = \Gamma_i/\Gamma$ where $\mathrm{F}_0 + \mathrm{F}_R + \mathrm{F}_L = 1$, at NNLO QCD are predicted as follows: $F_0 = 0.687 \pm 0.005$, $F_0 = 0.311 \pm 0.005$ and $F_0 = 0.0017 \pm 0.0001$ [34].

The experimental measurements of the helicity fractions are performed by studying the shape of $cos\theta^*$ which is the angle between the direction of the charged lepton from the W-boson and the reversed direction of the b-quark from the top-quark where both are boosted into the W-boson rest frame. With this definition of $cos\theta^*$, the differential decay rate can be written as

$$\frac{1}{\Gamma}\frac{d\Gamma}{d\cos\theta^*} = \frac{3}{8}(1 + \cos\theta^*)F_R + \frac{3}{8}(1 - \cos\theta^*)F_L + \frac{3}{8}(1 - \cos\theta^*)F_0. \tag{2.7}$$

The helicity fractions can also be studied by measuring the angular asymmetries $A_\pm$, which are defined as:

$$A_\pm = \frac{N(\cos\theta^* > z) - N(\cos\theta^* < z)}{N(\cos\theta^* > z) + N(\cos\theta^* < z)}. \tag{2.8}$$

where $z = \mp(2^{2/3} - 1)$. The asymmetries A_+ and A_- depend only on F_R and F_L respectively. The asymmetries A_+ and A_- at NNLO QCD are predicted by the SM to be $A_+ = 0.537 \pm 0.004$ and $A_- = -0.841 \pm 0.006$ [34]. The most precise measurement of the helicity fractions to date are presented by the ATLAS collaboration: $F_0 = 0.709 \pm 0.019$, $F_L = 0.299 \pm 0.015$ and $F_R = 0.008 \pm 0.014$ [35].

2.4 Top-quark pair production in association with a photon

As mentioned in the introduction of this chapter, the precise measurement of the top-quark's couplings to vector gauge bosons is of great importance for the test of the SM. In the following, first a brief mathematical structure of top-quark's coupling to neutral vector bosons, i.e. $t\bar{t}V$ vertex, is given. Then, as being the subject of this thesis, only the production mechanism of pair production of the top-quark with an additional photon is summarised.

2.4.1 $t\bar{t}V$ vertex

The mathematical description of the most general Lorentz-invariant $t\bar{t}V$ vertex can be written in terms of ten form factors [36]. However, the number of the form factors in the description reduces to four, if the neutral vector boson and the top quarks are on-shell and the the function of the vertex gets the following form:

$$\Gamma_{\mu}^{t\bar{t}V}(k^2,q,\bar{q}) = -ie\left[\gamma_{\mu}(F_{1V}^{V}(k^2)+\gamma_5 F_{1A}^{V}(k^2)) + \tfrac{\sigma_{\mu\nu}}{2m_t}(q+\bar{q})^{\nu}(iF_{2V}^{V}(k^2)+\gamma_5 F_{2A}^{V}(k^2))\right] \quad (2.9)$$

where e is the electric charge of the proton, m_t is the top-quark mass, $q(\bar{q})$ is the four-momenta of the outgoing top - anti-top-quark pair, and $k^2 = (q+\bar{q})^2$. In the low energy limit, i.e. $k^2 = 0$, the terms $F_{1V}^{V}(0)$ and $F_{1A}^{V}(0)$, are the $t\bar{t}V$ vector and axial vector form factors. If the neutral vector boson is a photon, the coefficients $F_{2V}^{\gamma}(0)$ and $F_{2A}^{\gamma}(0)$ are related to the magnetic and electric dipole form factors, g_t and d_t^{γ} through the following relations:

$$F_{2V}^{\gamma}(0) = Q_t\frac{g_t-2}{2}\,, \quad (2.10)$$

$$F_{2A}^{\gamma}(0) = \frac{2m_t}{e}\,d_t^{\gamma}\,, \quad (2.11)$$

where Q_t is the electric charge of the top-quark. The relations can be adapted for $t\bar{t}Z$ vertex through the weak magnetic and weak electric dipole moments, g_t^Z and d_t^Z. At tree level in the standard model,

$$F_{1V}^{\gamma,\mathrm{SM}} = -Q_t\,, \quad (2.12)$$

$$F_{1V}^{Z,\mathrm{SM}} = \frac{1}{4\sin\theta_{\mathrm{W}}\cos\theta_{\mathrm{W}}}\left(1-\frac{8}{3}\sin^2\theta_{\mathrm{W}}\right)\,, \quad (2.13)$$

$$F_{1A}^{Z,\mathrm{SM}} = \frac{1}{4\sin\theta_{\mathrm{W}}\cos\theta_{\mathrm{W}}}\,, \quad (2.14)$$

$$F_{2V}^{\gamma,\mathrm{SM}} = F_{2V}^{Z,\mathrm{SM}} = F_{2A}^{\gamma,\mathrm{SM}} = F_{2A}^{Z,\mathrm{SM}} = F_{1A}^{\gamma,\mathrm{SM}} = 0\,, \quad (2.15)$$

where θ_W is the weak mixing angle. Next-to-leading order corrections to $F_{1V,A}V$ are at the order of $\mathcal{O}(10^{-3}-10^{-2})$ [37] whereas the magnetic and weak magnetic dipole form factors $F_{2V}V$ are also subject to corrections of the same magnitude [38]. The electric and weak electric dipole form factors, however, do not receive such contributions. Any deviation from this prediction, therefore, could be interpreted as an indication of physics beyond the SM.

2.4.2 Radiative $t\bar{t}$ production

As already pointed out, top-quark pair production at the LHC is dominated by gg-fusion($\sim$90%). The remaining 10% is shared between $q\bar{q}$ annihilation through g, Z and γ. Since the production via g within this 10% is the dominating process, the possibility of direct probing top-quark - photon coupling via $q\bar{q} \to \gamma \to t\bar{t}$ process is almost completely excluded, although it is an allowed process at the LHC. Other than this process, there are two processes of top-quark pair production in association with a photon: the radiative production, $pp \to t\bar{t}\gamma \to l^{\pm}\nu b\bar{b}jj\gamma$, and the radiative decay, $pp \to t\bar{t} \to l^{\pm}\nu b\bar{b}jj\gamma$.

In the radiative top-quark pair production via gluon fusion, the photon can only be radiated off one of the top quarks. In the quark anti-quark annihilation, the photon can also be radiated off one of the incoming quarks. In this process, the top quark is assumed as a stable particle, which means the photon is radiated off a virtual (off-mass shell) top-quark. Feynman diagrams for radiative top-quark production processes are shown in figure 2.7.

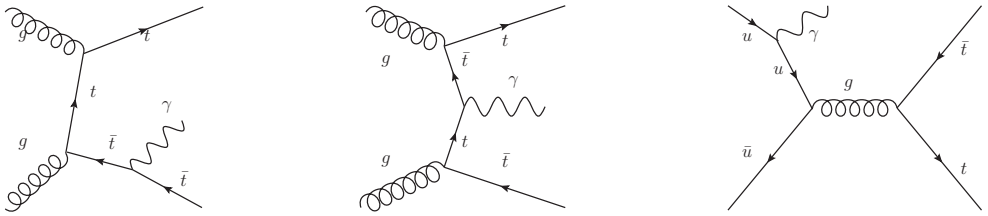

Figure 2.7.: Representative Feynman diagrams for radiative top-quark pair production.

2.4.3 Radiative $t\bar{t}$ decay

In the radiative top-quark decay, the photon can be radiated off an on-mass shell top-quark as well as the bottom-quark, off the W-boson from the top-quark decay and off the leptons from the W-boson decay. Only photons radiated off the top quark have importance for the top quark charge measurement. Feynman diagrams for the radiative top quark decay processes are shown in figure 2.8. Experimentally, it is not possible to distinguish between the radiative top quark production and the radiative top quark decay. Only the full event, which is determined by the final state, can be detected.

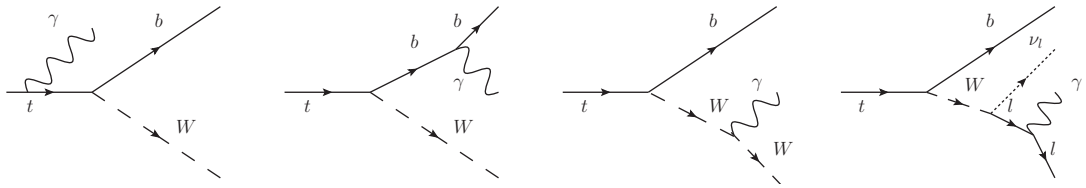

Figure 2.8.: Representative Feynman diagrams for radiative top-quark decay.

2.4.4 Traces of anomalous $t\bar{t}\gamma$ couplings

Since top-quark pairs at the LHC are produced via gluon fusion, the initial state radiation of photons is suppressed and this yields a very sensitive photon transverse momentum distribution to anomalous $t\bar{t}\gamma$ couplings which can be inferred from figure 2.9. At high p_T^{γ} region, distributions for non-standard vector and axial vector couplings have similar

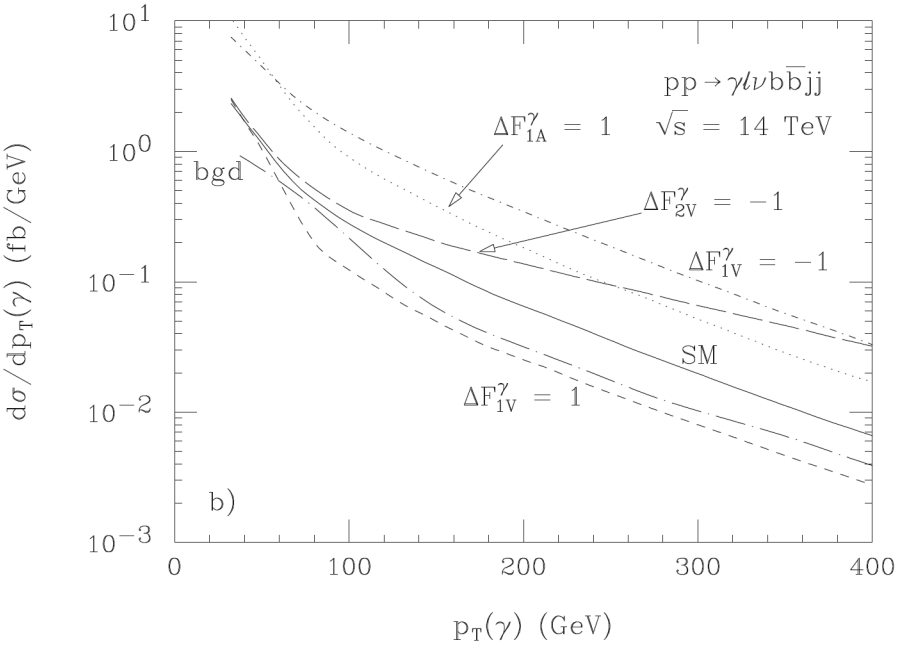

Figure 2.9.: Differential cross-section of $t\bar{t}\gamma$ production in the semileptonic channel as a function of the photon transverse momentum for at the LHC at $\sqrt{s}$ =14 TeV [39]. The continuous curve labelled as SM corresponds to the Standard Model prediction of the $t\bar{t}\gamma$ cross-section, while the dotted and dashed curves correspond to the $t\bar{t}\gamma$ cross-section with anomalous $t\gamma$ couplings. For each curve only, one coupling is allowed to deviate and the labels $\Delta F^{\gamma}_{1(2),V}(\Delta F^{\gamma}_{1(2),A})$ indicate the differences with respect to the SM of the vector (axial-vector) form-factors $F^{\gamma}_{1(2),V}(F^{\gamma}_{1(2),A})$.

behaviour to that of the SM prediction. However, at low p_T^γ region the shape of the SM and non-standard distributions differ, as it can be most explicitly observed with $\Delta F_{1V}^\gamma = 1$ in figure 2.9. This change in the shape of distributions at low p_T^γ rises up from the contribution of radiative top-quark decays which can contribute only this region. This is because the SM and non-standard helicity amplitudes interfere differently for $t\bar{t}\gamma$ and $t\bar{t}$ productions because of the radiation in the former production. The signal cross-section could be therefore either increased or decreased by non-standard vector or axial vector couplings since the interference effects of helicity amplitudes could be constructive or destructive.

Chapter 3

Experimental Apparatus

The data analysed for the analysis of this thesis was collected by the ATLAS detector (**A** **T**oroidal **L**HC **A**pparatu**S**), which is one of the high energy physics experiments constructed on the LHC (**L**arge **H**adron **C**ollider) located at CERN (**C**onseil **E**uropéen pour la **R**echerche **N**ucléaire) on the Franco-Swiss border near Geneva.

3.1 CERN

Founded in 1954 by twelve European states aiming for a collaborative work on fundamental nuclear research, the CERN accelerator complex is today the largest particle physics laboratory in the world (commonly referred to as the European Laboratory for Particle Physics) with twenty-two member states. With over six-hundred institutes and universities around the world having access to use its facilities, CERN welcomes half of the world's particle physicists for their research [40].

The accelerator complex at CERN is a chain of accelerators with increasingly higher energies. Each accelerator injects the beam into the next one which takes over to bring the beam to an even higher energy. The LHC, the last and the most powerful element of the chain, accelerates each particle beam up to a record energy and provides the detectors located on it with collisions. While the LHC is the main focus of research at CERN, experiments at other accelerators and facilities both on-site and off play an important role in the laboratory's activities [41].

CERN has contributed a great deal to our understanding of matter, which attracted Nobel Prizes as well as Nobel Laureates several times [42, 43]. Along with contributions to fundamental physics, the laboratory has also contributed to technical development with remarkable examples such as the World Wide Web and positron emission tomography (PET) [44, 45].

3.2 The Large Hadron Collider

The Large Hadron Collider (LHC) is a circular superconducting hadron collider installed in a 26.7 km long tunnel, with eight arcs and eight straight sections, that was constructed between 1984 and 1989 for the Large Electron-Positron Collider (LEP), which completed its mission in 2000. The tunnel lies on an inclined plane between 45 m and 170 m below the surface. Due to the stringent limit on space in the tunnel, the LHC has the "two-in-one" superconducting magnet design which was proposed originally for cost savings in 1971 at

the Brookhaven laboratory. A schematic view of the cross section of the LHC is presented in figure 3.1.

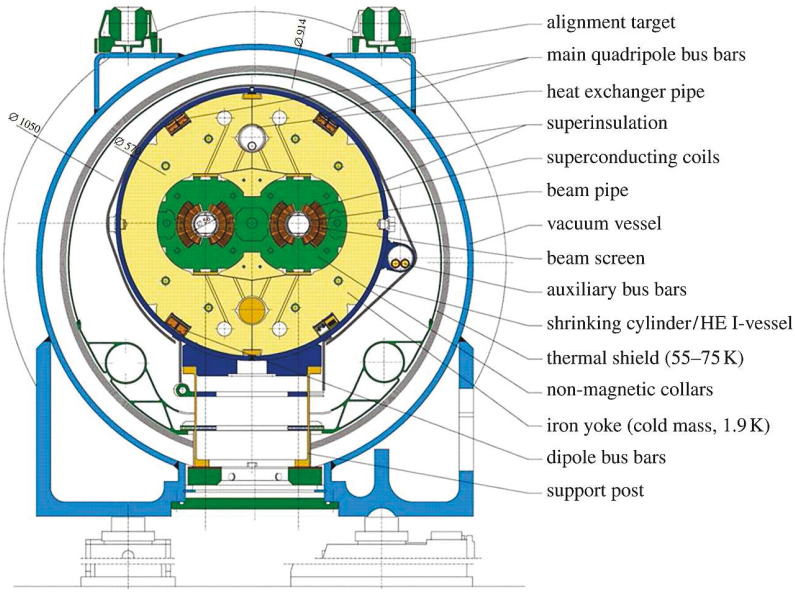

Figure 3.1.: Cross sectional schematic view of the LHC cryodipole (lengths in mm)[10].

Two counter circulating beams are stored in two separate pipes, accelerated and collided at four collision points at which four main experiments are located: two multi-purpose detectors ATLAS [10] and CMS [11], at Point 1 and Point 5 respectively, ALICE [46], at Point 2, investigating the quark-gluon plasma in heavy ion collisions and LHCb [47], at Point 8, focussing on *b*-physics. The caverns at Point 5 and 8 were constructed for the LEP while the caverns at Point 1 and 2 were constructed for the LHC. The machine is designed to accelerate protons and heavy ions, in particular lead nuclei. In addition to the four main experiments, the LHC has two more experiments: TOTEM (Total Elastic and Diffractive Cross-Section Measurement)and LHCf (Large Hadron Collider forward Experiment). The TOTEM detector measures the total proton-proton cross-section and studies elastic scattering and diffractive dissociation. LHCf is an experiment specialised for the forward region of the collisions and investigates the energy distribution of emitted particles which is important for the understanding of cosmic ray phenomena [49], [50]. The TOTEM and LHCf experiments share caverns at Point5 and Point1, respectively.

3.2.1 Injection Chain

As mentioned before, the proton beam is not accelerated by the LHC itself from rest to collision energy. The beam is pre-accelerated through a chain of accelerators with increasingly higher energies. Each accelerator injects the beam into the next one which takes over to bring the beams to an even higher energy until the beam is injected into the LHC. The pre-acceleration begins in a linear accelerator called Linac2 that is fed with a beam of protons. These protons are obtained from hydrogen atoms of which electrons are stripped off their nuclei by an electric field. Linac2 accelerates the beam to the energy of 50 MeV. The beam is then injected into the Proton Synchrotron Booster (PSB), which accelerates the protons to 1.4 GeV. The PSB is followed by the Proton Synchrotron (PS)

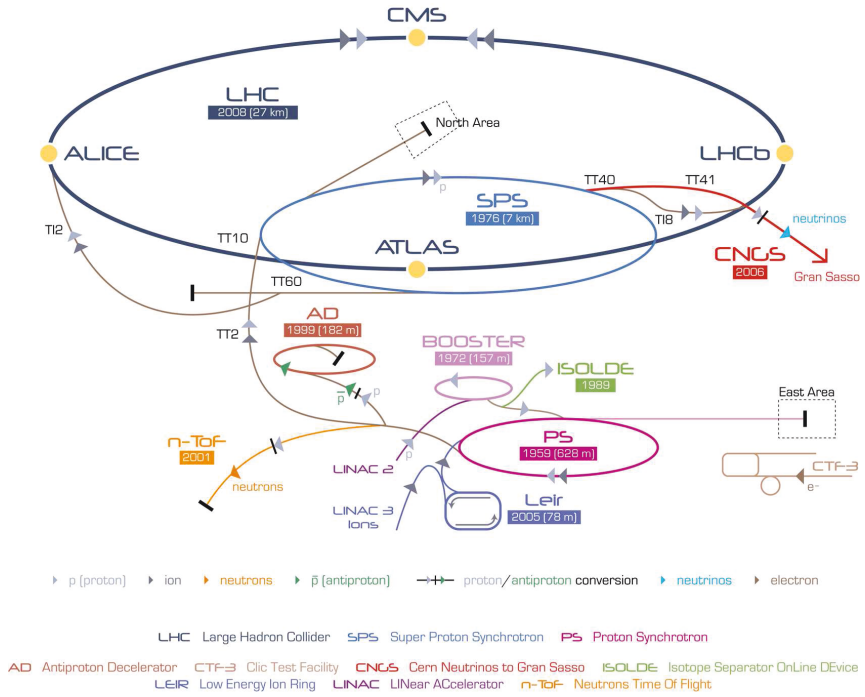

Figure 3.2.: The CERN accelerator complex, showing all particle accelerators situated at CERN. The LHC accelerator chain comprises (with increasing energy): Linac2 → Proton Synchrotron Booster → Proton Synchrotron Super Proton → Synchrotron LHC [48].

which brings the beam to 25 GeV. The last link of the pre-accelerator chain is the Super Proton Synchrotron (SPS) where the beam is accelerated to 450 GeV before it's injected into the LHC to hit the collision energy. The pre-acceleration path of the beam can be followed in figure 3.2.

3.2.2 Design

The LHC, most powerful collider ever built, is designed to accelerate proton beams, with 2808 bunches per proton beam and up to 10^{11} protons per bunch, and with a nominal bunch spacing of 25 ns, up to a centre-of-mass energy of 14 TeV. This design leads to 40 million collisions per second. The number of events per second produced in the LHC collisions is calculated by:

$$\frac{dN_{\text{event}}}{dt} = \mathcal{L} \cdot \sigma_{\text{event}} \tag{3.1}$$

where σ_{event} is the cross section for the event of interest and $\mathcal{L}$ is the machine luminosity which depends only on the machine parameters and, considering a Gaussian beam distribution, can be formulated as:

$$\mathcal{L} = \frac{N_b^2 \, n_b \, f_{\text{rev}} \gamma}{4\pi \epsilon_n \beta^*} F \tag{3.2}$$

where N_b is the number of particles per bunch, n_b the number of bunches per beam, f_{rev} the revolution frequency, γ the relativistic gamma factor, ϵ_n the normalised beam emittance, β^* the beta function at the collision point and F is the geometric luminosity

reduction factor due to the crossing angle at the interaction point. It is formulated as:

$$F = \left(1 + \left(\frac{\Theta_c \sigma_z}{2\sigma^*}\right)\right)^{-\frac{1}{2}}, \tag{3.3}$$

with Θ_c is the full crossing angle at the interaction point, σ_z the root mean square (RMS) bunch length and σ^* is the transverse RMS beam size at the interaction point. These equations assume equal parameters for both beams [51]. The LHC collides also heavy ions, in particular lead nuclei, at 5.5 TeV per nucleon pair at a design luminosity of $\mathcal{L}$=10^{27}cm^{-2}s^{-1} at the end of each year after proton runs end.

The ATLAS and CMS experiments aim at a peak luminosity of $\mathcal{L}$=10^{34}cm^{-2}s^{-1} where the designed peak luminosity of the LHCb experiment is $\mathcal{L}$=10^{32}cm^{-2}s^{-1}. The LHC has a dedicated experiment, TOTEM, for the detection of protons from elastic scattering at small angles which aims at a peak luminosity of $\mathcal{L}$=10^{32}cm^{-2}s^{-1} with 156 bunches. The ALICE experiment aims at a peak luminosity of $\mathcal{L}$=10^{27}cm^{-2}s^{-1}.

The LHC accelerates the beams using radio frequency (RF) cavity systems at a frequency of 400 MHz and the beams are kept on their circular paths utilising superconducting magnets. For this, the LHC makes use of a well-proven technology based on niobium-titanium alloy (NbTi) superconductors that are cooled down to a temperature below 1.9 K using superfluid helium for operating magnetic field of 8.33 T [51]. An important element of the LHC is its vacuum system which is a set of three vacuum components: the insulation vacuum for magnets, the insulation vacuum for superfluid helium distribution, and the beam vacuum. The operating pressure of the insulation vacua at cryogenic temperatures is around 10^{-6} mbar, while requirements for the beam pipe vacuum are much more stringent due to the required beam lifetime and background at the experiments. At cryogenic temperature, the requirements are expressed as gas densities normalised to hydrogen, taking into account the ionisation cross sections for each gas species. Equivalent hydrogen gas densities should remain below 10^{15} H_2 m^3 to ensure the required 100 hours beam lifetime where in the interaction regions around the experiments, the densities will be below 10^{13} H_2 m^3 to minimise the background. In the room temperature parts of the beam pipe vacuum system, the pressure should be in the range 10^{-10} to 10^{-11} mbar [10].

3.2.3 Performance

In 1994, the member states of CERN have decided to start the construction of the LHC in 2000 after the shutdown of the LEP. The initial plan was to start to run the LHC for collisions at the centre-of-mass energy of 10 TeV before upgrading the machine to run at the design energy, 14 TeV. However, during the construction it was decided to lower down the initial start up collision energy to 7 TeV in order to avoid magnet quenches.

In September 2008, the first proton beams were injected into the LHC but nine days after the first injection, a fault occurred in an electrical bus connection in the region between a dipole and a quadrupole. This fault caused a mechanical damage and release of helium into the tunnel, which postponed the LHC programme by more than a year [52]. The LHC has recorded the first test collisions at the injection energy in November 2009 and the first collisions at the desired start up collision energy, 7 TeV, on March 30^{th} 2010 [53]. On October 18^{th} 2011, the LHC concluded recording data at 7 TeV with a remarkable performance. The first inverse femtobarn -approximately 10^{12} proton-proton collisions was reached on June 17^{th} 2011 and by the end of data recording at 7 TeV almost six femtobarns of data were delivered by the LHC [54]. At the end of data recording at 7 TeV, a long shutdown was planned to upgrade the machine for the collisions at design

centre-of-mass energy, 14 TeV. However, exiting hints of new physics observed with the 7 TeV data postponed the long shutdown to record more data for one more year to turn those hints into a discovery. The LHC then started to operate accordingly and delivering collision at a new record energy of 8 TeV on April 5^{th} 2012 [55]. The data taking at 8 TeV took place for almost for a year and on February 16^{th} 2013 were the beams extracted from the LHC completing "Run 1" before the first long shutdown with an amount of delivered $\mathcal{L}$=22.8 fb^{-1} data, of which $\mathcal{L}$=20.2 fb^{-1} is suitable for physics at the ATLAS experiment. [56]. After two years of intense maintanance over 2013 and 2014, on April 5^{th} 2015, the LHC was back in operation again with test beams at 450 GeV. On June 3^{rd} 2015, the LHC has recorded the first collision at 13 TeV and data recording for RunII has started which has continued until November 4^{th} 2015. After a technical stop, the LHC has started recording data on March 26^{th} 2016 until October 25^{th} 2016 when the heavy ion collisions started.

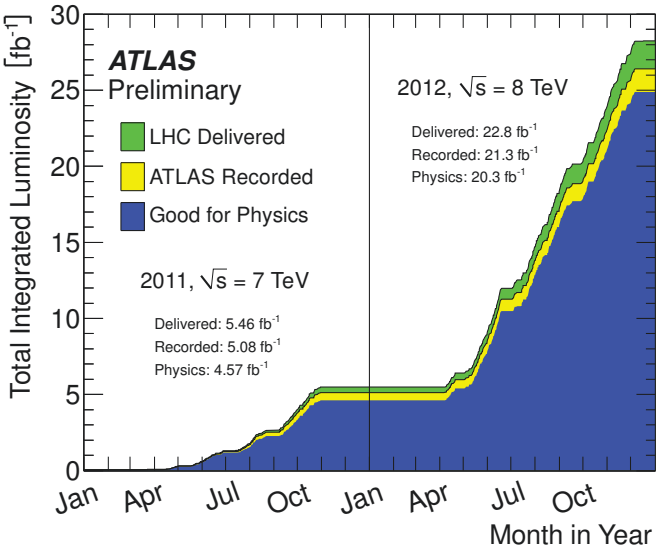

Figure 3.3.: Cumulative luminosity versus time delivered (green), recorded by ATLAS (yellow), and certified to be good quality data (blue) during stable beams and for pp collisions at 7 and 8 TeV centre-of-mass energy in 2011 and 2012. [57]

Figure 3.3 shows how the integrated luminosity accumulated during 2011 and 2012. The analysis of this thesis makes use of the proton-proton collisions recorded at 8 TeV by ATLAS. Due to the high instantaneous luminosity, 20.7 interactions per crossing occurred in average which is also referred to as pile-up. The pile-up has two components: Interactions from the same bunch crossing, *in-time* pile-up and interactions from previous crossings, *out-of-time* pile-up. The luminosity-weighted distribution of the pile-up is shown in figure 3.4.

3.3 The ATLAS Detector

The ATLAS detector is a general purpose detector with a versatile physics potential ranging from precise measurements of the Standard Model parameters to searches of new physics phenomena. Motivated by this reason, ATLAS is designed to detect and measure momenta and energies of leptons, photons and jets in an almost full coverage in terms of

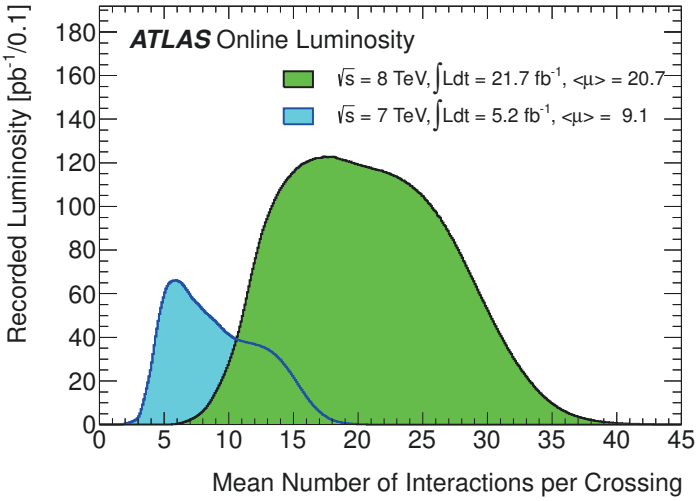

Figure 3.4.: The luminosity-weighted distribution of the mean number of interactions per crossing for the 2011 and 2012 data. [57]

solid angle around the interaction point.

This is achieved by designing the detector in four different components. The skeleton of ATLAS is formed by its magnet system. The other three components are structured accordingly. The innermost component is designed to detect tracks of charged particles as well as precise position of primary and secondary vertices. The second component, calorimetry, consists of two different calorimeters and is used to measure energy deposits of electron, photons and hadrons. The last and the outermost component is the muon system. All three components consist of central and forward regions providing a hermetic coverage around the collision point. Central regions of the detector components have a barrel form. Forward regions contain both barrel-shaped and end-cap components.

3.3.1 Coordinate System

The ATLAS detector uses a right-handed coordinate system (ϕ, η, z) with the interaction point being the origin of the system and where the azimuthal angle ϕ and the pseudo-rapidity η are defined with respect to x-, y- and z-axes. Here, the z-axis is defined by the beam pipe where the x-axis points to the centre of the LHC and y-axis points upwards. The azimuthal angle ϕ is the angle in the x-y plane and the pseudo-rapidity η is an approximation of rapidity, y[1], being defined in terms of the polar angle θ which is the angle in the y-z plane. The pseudo-rapidity is formulated as follows:

$$\eta = -\ln \tan(\frac{\theta}{2}) \tag{3.4}$$

Distance differences in terms of pseudo-rapidity are Lorentz invariant under boosts along the beam direction. For this reason, the distance between two physical objects in

[1]In experimental particle physics, the rapidity is defined as: $y = 1/2\ln(E + p_z/E - p_z)$ where p_z is the momentum component along the beam axis.

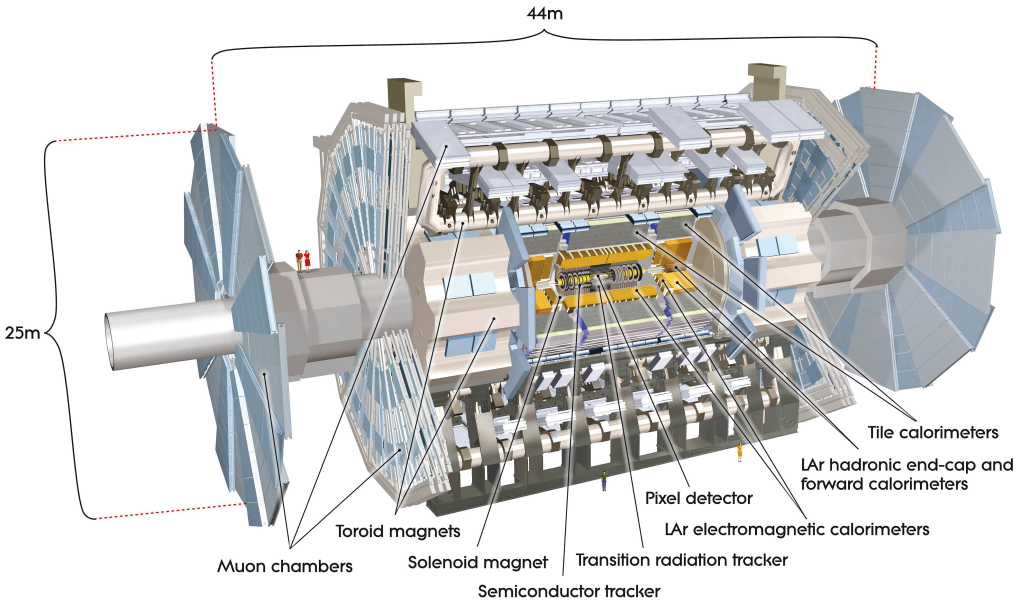

Figure 3.5.: Cut-away view of the ATLAS detector. The dimensions of the detector are 25 m in height and 44 m in length. The overall weight of the detector is approximately 7000 tons. [10]

the detector is defined in terms of pseudo-rapidity and azimuthal angle as follows:

$$\Delta R = \sqrt{(\Delta\eta)^2 + (\Delta\phi)^2}. \tag{3.5}$$

Furthermore, because of this very same reason, the energies and momenta of particles are expressed in the transverse plane $(x - y)$ which are referred to as transverse momentum, p_T, or transverse energy, E_T. They are formulated as follows:

$$p_T = \sqrt{p_x^2 + p_y^2} = \mid p \mid sin\theta \quad \text{and} \quad E_T = \mid E \mid \sin\theta. \tag{3.6}$$

The ATLAS detector is not designed to detect weakly-interacting neutral particles, such as neutrinos. They traverse throughout the detector without leaving any trace behind. Therefore, their kinematics are inferred and calculated exploiting the imbalance in the momentum conservation in the transverse plane and referred to as the missing energy $\not{E}_T$[2].

3.3.2 Magnet System

The momentum of a charged particle is determined by measuring the curvature of its trajectory through the magnetic field of ATLAS. This field is maintained by a system of four superconducting magnets: one solenoid and three toroids (one barrel and two end-caps). Except for some parts of the muon chamber, the magnet system encloses all components of the detector to bend the charged particles. The solenoid magnet provides

[2]The imbalance is in fact in terms of momentum. However, since neutrinos are considered as massless (or to have a tiny mass), the missing momentum equals to energy and therefore referred to as missing energy. Details are described in chapter 4).

a magnetic field for the inner detector while the barrel and end-cap toroidal magnets provides the magnetic field for the muon system. The system operates at 4.5 K.

The Solenoid

The solenoid is aligned on the beam axis and covers the space between 1.22 m $< r <$ 1.32 m of the detector geometry and a distance of 5.8 m along the z-axis between the inner detector and the electromagnetic calorimeter. To further reduce passive detector material, it is assembled inside the same vacuum vessel as the calorimeter. It provides a 2 T axial magnetic field for the ID, while minimising the radiative thickness in front of the barrel EM calorimeter.

The Toroids

The barrel toroid consists of eight coils, each encased in racetrack oval and stainless-steel vacuum vessels, having an overall size of 25.3 m in length with 9.4 m and 20.1 m of inner and outer diameters respectively. The barrel toroid provides its magnetic field in a cylindrical volume surrounding the calorimeters and both end-cap toroids. It produces a magnetic field of approximately 0.5 T.

Each end-cap toroid consists of a single cold mass built up from eight flat, square coil units and eight keystone wedges. They are bolted and glued together to form a rigid structure to withstand the Lorentz forces. Each end-cap toroid has an inner and an outer diameters of 1.65 m and 10.7 m respectively. The end-cap toroids provide a magnetic field of 1 T and they are rotated by 22.5 degrees to ensure optimal bending power in the transition region.

The conductor and coil-winding technology is essentially the same in the barrel and end-cap toroids and is based on winding a pure Al-stabilised Nb/Ti/Cu conductor.

3.3.3 Tracking

The ATLAS experiment has to deal with a large track density, which is approximately 1000 emerging particles from the interaction point every 25 ns. This turns the tracking system into a keystone component to achieve the momentum and vertex resolution requirements needed by the benchmark physics processes. The innermost component of ATLAS, the inner detector (ID), is designed to cover this requirement and consists of three independent but complementary sub-detectors. It utilises two silicon based trackers, Pixel detector and Semiconductor Tracker (SCT), in conjunction with the straw tubes of the Transition Radiation Tracker (TRT). The Pixel Detector and the SCT are designed to reconstruct charged particle tracks down to a p_T of 0.5 GeV. They cover the full ϕ angle and provide tracking in the region of $|\eta| < 2.5$. The ID also provides some rudimentary particle identification using transition radiation information in the TRT. The layout of the ATLAS ID is illustrated in figure 3.6.

Precision Tracking

The precision tracking detectors, the Pixel and the SCT, are arranged in concentric cylinders around the beam axis in the barrel region while in the end-cap regions they are located on disks perpendicular to the beam axis.

The pixel layers are segmented in $R - \phi$ and z with typically three pixel layers crossed by each track where the first layer is just 5 cm away from the beam line. Being

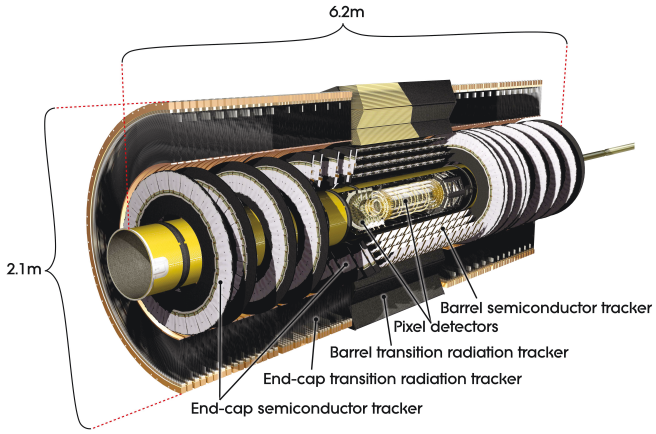

Figure 3.6.: Cut-away view of the ATLAS inner detector. [10]

the closest component to the beam line, the pixel detector is responsible to provide a highly precise measurement of the impact parameter of the tracks as well as the information needed to identify particles such as τ-leptons and jets from heavy quarks. To fulfil this, the Pixel Detector is designed to have the highest granularity among all detector components containing 80 per cent of all read-out channels of ATLAS. Around 80.4 million readout channels are shared between 1744 pixel sensors, each with 46080 pixels, and with a minimum (maximum) pixel size in R-$\phi \times z$ of 50×400 μ m^2 (50×600 μm^2). The intrinsic measurement accuracies in the barrel region are 10 μm (R-ϕ) and 115 μm (z) and ion the end-caps are 10 μm (R-ϕ) and 115 μm (R).

The Semiconductor Tracker is based on the same physics principles and material as the Pixel Detector. The difference is the use of larger stereo strip sensors rather than small rectangular pixels. The innermost layer is about 25 cm away from the beam pipe. In the barrel region, the SCT utilises small-angle (40 mrad) stereo strips to measure both coordinates, with one set of strips in each layer parallel to the beam direction, measuring $R - \phi$, and with the innermost layer being about 25 cm away from the beam pipe. Each set of strips consists of two 6.4 cm long daisy-chained sensors with a strip pitch of 80 mm. In the end-cap region, strips are aligned perpendicular to the beam line with a set of stereo strips at an angle of 40 mrad. The mean pitch of the strips is also approximately 80 μm. The intrinsic accuracies per module in the barrel are 17 μm ($R - \phi$) and 580 μm (z) and in the disks are 17 μm ($R - \phi$) and 580 μm (R). The total number of readout channels in the SCT is approximately 6.3 million.

Transition Radiation Tracking

The outermost component of the inner detector is the Transition Radiation Tracker. As the name explains itself, this component makes use of *tracks* left behind by photon *radiations* from charged particles that are *transiting* two media with different dielectric constants. Unlike the two silicon-based components, this component makes use of straw-tube technology. Each tube is filled with a mixture of XeO_2CO_2 gas surrounding a 31 μm tungsten wire at the centre. Charged particles emerging from the collision traverse the straw-tubes leaving a trace of ionised gas behind. The information for track reconstruction is then provided as free electrons from the ionised gas drift towards the wire at the centre by the electric field applied. The TRT is not as precise as the silicon-based components of the

ID in terms of the track measurement. However, a rudimentary particle identification is possible, since electrons from the hard interaction have low mass and high energies and tend to create a higher number of photons than heavier particles, such as charged pions which create less transition radiation.

The 4 mm diameter straw-tubes provide around 36 hits per track within $|\eta| < 2.0$. The TRT only provides $R-\phi$ information with an intrinsic accuracy of 130 μm per straw. The straws are parallel to the beam line and are 144 cm long with their wires divided into two halves, approximately at η=0. At the end-caps, the straws are perpendicular to the beam line and have a length of 37 cm. The TRT is read out with an approximate number of channels of 351000.

3.3.4 Calorimetry

Calorimeters are designed to measure energy of the most of neutral and charged particles such as photons, electrons and hadrons. The ATLAS calorimetry makes use of a method that depends on the absorption of the traversing particle energy in a passive absorber material with a high number of protons in the nucleus followed by the read-out of the signal, which caused by the absorbed energy, by an active detector material. This method is referred to as *sampling* (and correspondingly *sampling calorimeters*) since only a sample of the absorbed energy is measured.

The ATLAS calorimetry consists of two different calorimeters. The inner component of the calorimetry is the electromagnetic calorimeter and has a fine granularity in the central region of the detector which provides a high resolution for energy measurements of photons and electrons. Around the electromagnetic calorimeter and in the forward region is the hadronic calorimeter which provides information for precision measurements of jets and missing transverse energy, despite its coarser structure. The hadronic calorimeter in the forward region covers the detector space up to $|\eta| < 4.9$ to ensure the detection of all particles which are detectable in order for the measurement of the missing energy. The ATLAS calorimetry is capable of measuring particle energies over a range from a few GeV up to several TeV. A schematic view of the ATLAS calorimetry is illustrated in figure 3.7.

The Electromagnetic Calorimeter (ECAL)

The ECAL consists of three regions, one barrel ($|\eta| < 1.475$) and two end-caps ($1.375 < |\eta| < 3.2$), each being housed in their own cryostat. The barrel calorimeter is divided into two identical halves separated by a small gap of 4 mm at z=0, while each end-cap calorimeter is mechanically divided into two coaxial wheels. The ECAL uses liquid argon(LAr) as the active material and lead observer plates over its overall region. The ECAL is designed adopting an accordion-like architecture which provides complete symmetry in the azimuthal angle without any crack. The region up to $|\eta| <=2.5$ is devoted to precise measurement and the ECAL is segmented in three longitudinal layers over this region. The first layer is finely segmented along η, but the first layer in the edge zones of the barrel and end-caps has a coarser granularity. The second layer collects the largest fraction of the energy of the electromagnetic shower which enhances the information needed to distinguish between particles such as photons and neutral π-mesons as well as electrons/positrons and charged π-mesons. The third layer collects only the tail of the electromagnetic shower and is therefore less segmented in η. The ECAL is read out with an approximate channel number of 190000. The details of the granularity for each region are given in figure 3.8.

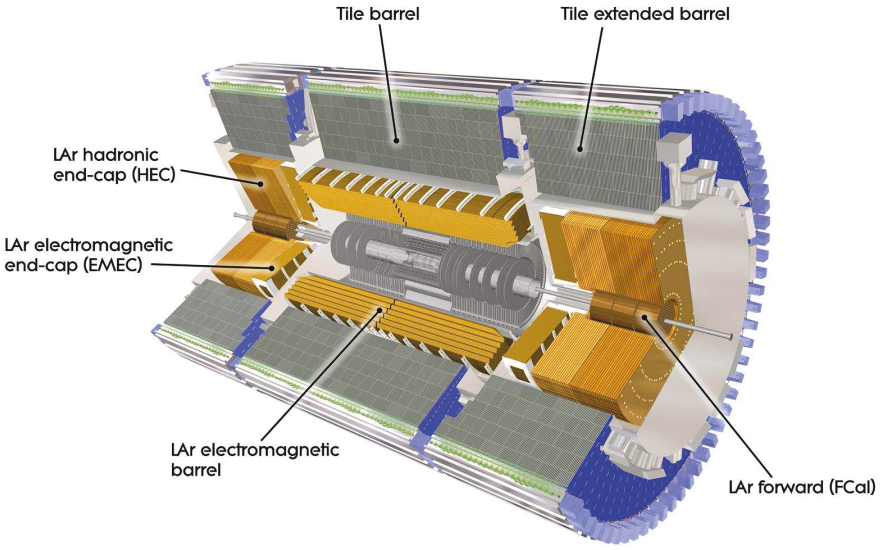

Figure 3.7.: An overview of the calorimetry at the ATLAS detector. [10]

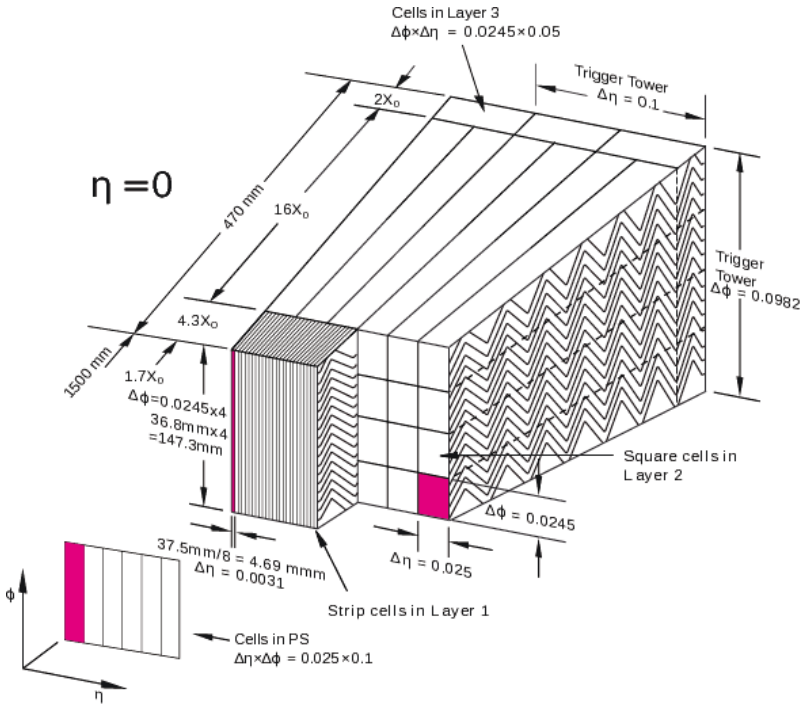

Figure 3.8.: Sketch of a barrel module of the ECAL showing the different layers. The granularity in η and ϕ of the cells of each of the three layers and of the trigger towers is also shown. [10]

The Hadronic Calorimeter

Energy measurement of particles that interact via the strong interaction with the nuclei of the material is handled in the hadronic calorimeter at ATLAS. The central region ($|\eta| < 1.7$) is equipped with a sampling calorimeter using scintillating tiles and iron plates while the forward region (up to $|\eta| < 4.9$) is designed as a combination of a LAr hadronic end-cap calorimeter (HEC) and LAr forward calorimeters.

Placed directly outside the ECAL and being a sampling calorimeter with steel as the passive material and scintillating tiles as the active material, the hadronic tile calorimeter consists of a barrel part ($|\eta| < 1.0$) and two extended barrels ($0.8 < |\eta| < 1.7$) that are azimuthally divided into 64 modules. The tile calorimeter is longitudinally segmented in three layers with approximate thicknesses of 1.5, 4.1 and 1.8 interaction lengths (λ) for the barrel and 1.5, 2.6, 3.3 λ for the extended barrels. The total thickness at the outer edge of the tile-instrumented region is 9.7 λ at η=0. The scintillating tiles are read out on both sides by wavelength shifting fibres into two separate photomultiplier tubes.

The hadronic LAr calorimeters are implanted in the same cryostat as the ECAL end-caps. On each side of the detector, the hadronic end-cap calorimeter (HEC) covers the region of $1.5 < |\eta| < 3.2$ while a dedicated forward calorimeter (FCAL) in the very forward region close to the beam pipe covers the region of $3.1 < |\eta| < 4.9$. Both end-cap and forward hadronic calorimeters utilise the same manner and active material as the LAr ECAL. The HEC consists of two independent wheels at both end-caps, located just behind the end-cap ECAL. Each wheel is built from 32 identical wedge-shaped modules and longitudinally divided into two segments for a total of four layers per end-cap. The wheels closest to the collision point are built from 25 mm parallel copper plates, while those further away are built from 50 mm copper plates. The copper plates are interleaved with 8.5 mm LAr gaps, providing the active medium. The FCal is integrated into the end-cap cryostats. This integration provides advantages in terms of uniformity of the calorimetric coverage as well as reduced radiation background levels in the muon spectrometer. The FCAL has a depth of around ten interaction lengths and consists of three modules in each end-cap: the first is made of copper and optimised for the electromagnetic measurements, while the other two are made of tungsten and measure predominantly the energy of hadronic interactions. Each module consists of a metal matrix, with regularly spaced longitudinal channels filled with the electrode structure consisting of concentric rods and tubes parallel to the beam axis.

3.3.5 Muon Spectrometry (MS)

The muon spectrometry is situated as the outermost component of ATLAS since muons traverse throughout the detector. The reconstruction of the muon momentum is based on the deflection of muons tracks in the magnetic field generated by the large superconducting air-core toroid magnets instrumented with trigger and high-precision tracking chambers: Monitored Drift-Tube Chambers (MDTs), Cathode Strip Chambers (CSCs), Resistive Plate Chambers (RPCs) and Thin Gap Chambers (TGCs). The former two are used for the tracking measurements, while the latter two are used for triggering. In order for the deflection of muons, magnets are configured in such a way that they provides a magnetic field which is mostly orthogonal to the muons trajectories, while minimising the degradation of resolution due to multiple scattering. With this configuration, magnetic bending is provided by the large barrel toroid over the range $|\eta| < 1.4$ while for the region $1.6 < |\eta| < 2.7$ by two smaller end-cap toroids and over the transition region ($1.4 < |\eta| < 1.6$) by a combination of barrel and end-cap toroids. In the barrel region,

tracks are measured in chambers arranged in three cylindrical layers around the beam axis while in the transition and end-cap regions, the chambers are installed in planes orthogonal to the beam, also in three layers. The MS is designed for a momentum resolution of $\Delta p_T/p_T < 1 \times 10^{-4} \times p/\text{GeV}$ for momenta larger than 300 GeV. For smaller momenta, the resolution is limited to a few per cent by multiple scattering in the magnet and detector structures, and by energy loss fluctuations in the calorimeters.

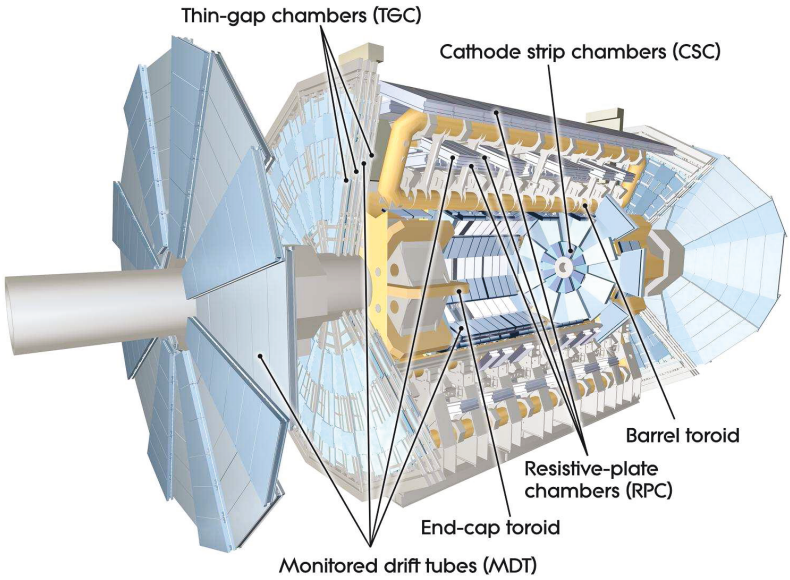

Figure 3.9.: Cut-away view of the ATLAS muon system. [10]

Monitored Drift-Tube Chambers

In the MDTs, muons are detected by the use of aluminium tubes with a diameter of 30 mm which are filled with an $ArCO_2$ mixture at 3 bar. The electrons of the ionised gas are collected at the central tungsten-rhenium (W-Re) wire with a diameter of 50 mm, using a potential of 3080 V. The MDTs are installed in three layers of chambers in the full barrel region (up to $|\eta|$ <=2.0) and the innermost layer of the end-cap wheels, except for the innermost layer which is equipped with a CSC. The resolution per tube is about 80 μm and 35 μm per chamber.

Cathode Strip Chambers

The CSCs are multi-wire proportional chambers filled with $ArCO_2CF_4$ mixture, where the cathode is segmented in strips. They are designed to operate where the particle fluxes are highest. They are capable of providing a position resolution down to 60 μm per wire pitch. Located at approximately 7 m away from the interaction point, they occupy the radial region of $2.0 < |\eta| < 2.7$ and are read out with a close total number of strips of 67000.

Resistive Plate Chambers

The RPCs, a gaseous parallel-plate detector with a typical space-time resolution of the order of 1 cm×1ns, provide trigger signals in the barrel region ($|\eta| < 1.05$). They consist of two resistive plates, made of bakelite, which are parallel to one another with a space of 2 mm in between filled with a gas mixture of $C_2H_2F_4$. Each bakelite is read out via two orthogonal strips using capacitive coupling. One layer of the strips is situated in parallel to the MDT wires, the other orthogonally. This design allows a complementary measurement of both η and ϕ position of the track. The RPCs are read out digitally.

Thin Gap Chambers

The TGCs are multi-wire proportional chambers consisting of two cathode plates with a space of 2.8 mm in between filled with a gas mixture of CO_2 and C_5H_{10}, and equipped with an anode wire placed in between the cathodes with a distance of 1.8 mm to the next wire. The TGCs operate in the region of $1.5 < |\eta| < 2.4$ and are optimised to create fast signals due to a short drift time. The anode wires are situated in parallel to the MDT wires, while the readout strips of the cathode plates are situated orthogonally in order to achieve additional information in ϕ.

3.3.6 Trigger System

At the bunch-crossing rate of 40 millions per second, each containing on average 23 interactions at design luminosity of the LHC, the interaction rate is 10^9 interactions per second. A trigger system therefore is probably the most crucial element of any LHC experiment, since it is the mechanism that takes a decision every 25 ns to select events with rare predicted physics processes efficiently from these 10^9 interactions while rejecting well-known and high statistics processes at low momenta, referred to as minimum bias events, because even for the extensive computing resources of ATLAS this is a huge amount of interactions to cope with in terms of both reading out the detector and recording.

The ATLAS experiment copes with this issue with a trigger system composed of three levels: level-one (L1), level-two (L2) and event filter (EF). The L1 is a hardware based stage, while the L2 and the EF are software based and are collectively referred to as the High Level Trigger (HLT).

The most interesting physics processes have designated signatures: such as large missing transverse energy, highly energetic jets or leptons. The trigger system is designed to make use of this fact with an increasing precision and granularity at each level. At the end of this chain, the event storage rate is limited to approximately 200 Hz with the average event size is 1 Mb.

L1 Trigger System

The L1 trigger is designed to perform an efficient identification of the basic characteristics of 'interesting' physics such as high transverse-momentum muons, electrons, photons, jets, and tau-leptons decaying into hadrons, as well as large missing and total transverse energy by exploiting the information from a subset of detectors. High transverse-momentum muons are identified using trigger chambers in the barrel and end-cap regions of the spectrometer. Calorimeter selections make use of reduced-granularity information from all the calorimeters. A trigger menu made up of combinations of trigger selections is then implemented by the central trigger processor which processes the results from the L1

muon and calorimeter triggers. Pre-scaling of trigger menu items is also available, allowing optimal use of the bandwidth as luminosity and background conditions change.

Through the process described above, the L1 trigger reduces the data rate to 75 kHz and to makes a decision about the importance of an event within an approximate decision time of 2 μm. Events passing the L1 trigger selection are then transferred to the next stages of the detector-specific electronics and subsequently to the data acquisition via point-to-point links. In each event, the L1 trigger also defines one or more Regions-of-Interest (RoIs), i.e. the geometric coordinates in η and ϕ, of those regions within the detector where its selection process has identified interesting features. The RoI data include information on the type of feature identified and the criteria passed, e.g. a threshold. This information is subsequently used by the high-level trigger.

High Level Trigger

The L2 trigger performs more sophisticated reconstruction of physics objects than the L1, since it makes use of information from all three main components of ATLAS: the ID, calorimetry and muon system. Despite the more sophisticated reconstruction software algorithms, the L2 is still able to constrain the decision time to shorter than 40 ms. The L2 trigger reduces the rate of events from 75 kHz to the order of 1 kHz. The final and the most complex level of the trigger system is the EF. The EF is therefore designed to take decision within a relatively long time, 1 s to reconstruct events. Its algorithms make use of the full detector information and often the reconstruction performance is comparable to the offline reconstruction algorithms. The EF reduces the trigger rate from a few kHz to a few hundred Hz. Following the HLT decision the events are written to disk.

L1 trigger is a great thing to have in the ATLAS detector. It'S function is the first level triggering of the produced data. It performs a very efficient triggering and delivers the triggered data to the second level trigger, which is called High level trigger. This is a ver sophisticated trigger. Despite the more sophisticated reconstruction software algorithms, the L2 is still able to constrain the decision time to shorter than 40 ms. The L2 trigger reduces the rate of events from hundreds of kHz to the order of 1 1 kHz.

The final and the most complex level of the trigger system is the EF. The EF is therefore designed to take decision with in a relatively long time, 1 s to reconstruct events. Its algorithms make use of the full detector information and often the reconstruction performance is comparable to the offline reconstruction algorithms. The EF reduces the trigger rate from a few kHz (i.e. below 3.5 kHz) to 200 Hz. Following the HLT decision, the event rates are written to disk.

Chapter 4

Physical Objects

As partially described in the previous chapter, particles leave traces of electronic signals behind when they traverse the detector. This first part of chapter will describe how these signals are reconstructed and identified as physical objects. Since the subject of this work involves the cross section measurement of top-quark pair production in the *lepton+jets* channel, only physical objects, which are relevant to this final state, are described. These objects are electrons, muons, photons, jets and missing transverse energy.

The second part of the chapter provides the descriptions of the data from the ATLAS detector and simulations used in the analysis.

The recommended offline selection of the physical objects are given here [58].

4.1 Jets

Quarks and gluons (partons), physics objects of the QCD, are central concepts at high-energy collisions. They, however, are not observable. What the detectors detect are instead collimated bunches of hadrons produced by fragmented and hadronised partons, so-called jets, from the collisions.

4.1.1 Reconstruction and Calibration

Jet objects are reconstructed using a sequential recombination based jet clustering algorithm (k_T and Cambridge). The idea of this algorithm is based on the principle of taking the hardest object[1] (particle, calorimeter tower) in the event as a seed of an iterative search for a stable cone, which will be then considered as a jet. The algorithm then removes all the particles contained in that cone of jet from the event record and the procedure starts over with the hardest available remaining seed. The process is repeated until no seeds remain. The key feature of this algorithm is to be an infrared and collinear (IRC) safe algorithm which means that the jet reconstruction is dependent neither on infrared nor on collinear radiations from gluons. In other words, jet boundaries determined with this algorithm are resilient with respect to soft radiation, but flexible with respect to hard radiation. The reconstruction is performed using two distance parameters: d_{ij} between entities (particles and pseudo-jets) i and j, and d_{iB} between an entity i and the beam B. The entities i and j are recombined if d_{ij} is identified as the smallest distance. If, however, d_{iB} is the smallest distance, the entity i is deleted from the list of entities. The procedure

[1] Reconstruction of jets makes use of clustering of energy deposits into so-called TopoClusters [59].

starts over to identify all distances and is repeated until no entity is left [60].

The jet clustering algorithm used in this analysis is the anti-k_t algorithm which is an extended version of afore-mentioned clustering algorithms. Its extension relative those lies in the definition of distance measures:

$$d_{ij} = \min\left(k_{ti}^{2p}, k_{tj}^{2p}\right)\frac{\Delta_{ij}^2}{R^2}, \tag{4.1}$$

$$d_{iB} = k_{ti}^{2p}, \tag{4.2}$$

where k_{ti}, y_i and ϕ_i denote respectively the transverse momentum, rapidity and azimuth of particle i, and Δ_{ij} is defined as the quadratic sum of rapidity and azimuth differences of the entities ($\sqrt{(y_i - y_j)^2 + (\phi_i - \phi_j)^2}$). The parameter R is the radius parameter of the cone and the parameter p regulates the relative power of the energy versus the geometrical scales Δ_{ij} [60]. Different values of p corresponds to behaviours of different clustering algorithms. The k_t algorithm is recovered by $p = 1$, where $p = 0$ is special and recovers the Cambridge/Aachen. The $p = -1$ corresponds to the anti-k_t algorithm.

The distance between a hard and a soft particle is generally smaller than that the distance between similarly separated soft particles. This can be inferred from equation 4.1. The distant measure is dominated by the momentum of the hard entity when the value of $p = -1$ is inserted which implies that soft entities are more likely to be recombined with hard entities rather than with the soft entities [60]. For this analysis, the radius parameter of $R = 0.4$ is used for jet clustering. [61].

The jets are calibrated using the so-called *local cluster weighing* (LCW) method [61]. This method calibrates clusters individually *prior* to jet finding and reconstruction by using the properties of them such as the energy density in the cells forming them, the fraction of their energy deposited in the different calorimeter layers and the cluster isolation and its depth in the calorimeter. The localness of the method originates from the choice that corrections are applied to the cluster energy to account for the energy deposited in the calorimeter excluding the clusters and energy deposited in material before and in between the calorimeters. The reconstruction procedure described above is performed using these calibrated clusters, and a final correction is applied to the jet energy to account for jet-level effects. The resulting jet calibration is denoted as LCW+JES from here on.

4.1.2 Selection

As described earlier, the jets are fairly complex physics objects composed of many particles. This fact makes the reconstruction of jets vulnerable and sensitive to a couple of factors such as out-of-time energy depositions, calorimeter hardware problems, LHC beam gas interactions and cosmic ray induced showers. These factors can lead to reconstruction of the so-called *bad jets*.

First step of selecting jets is to identify these bad jets by applying a set of jet quality criteria described in detail elsewhere [62, 63]. On top of the jet quality criteria, a cut on the jet vertex fraction is applied to reduce the effect of in-time pile-up. The jet vertex fraction (JVF) [64] is defined as the fraction of the total transverse momentum of the jets associated tracks that is contributed by tracks from the PV. This JVF helps to estimate the contribution of multiple interactions, providing a discriminant for jets in form of a probability of the jet to not have been generated by pile up interactions.

Jets fulfilling the quality criteria and being within the kinematic acceptance of $p_T > 25$ GeV and $|\eta| < 2.5$ are selected. Jet candidates are also required to satisfy the optimum working

point for the JVF cut which is found to be 0.5 (R Camacho and S Calvet. Jvf studies for top analyses in 2012 data. Contribution to ATLAS Hadronic Calibration Workshop 2012). At this working point, optimal efficiency of hard scatter jets selection versus rejection of pile-up jets is achieved along with maintenance of an efficient selection of hard scatter jets. In order to avoid duplications of jet candidates with other objects, a doublet of overlap removal is performed. First of these overlap removals is between jets and *good electrons* (cf. section 4.2): The closest jet to a good electron candidate is removed if $\Delta R < 0.2$. The second is between jets and photons: any jet within a cone of $\Delta R = 0.1$ around a *tight photon*(cf. section 4.4) is also removed.

4.1.3 b-Tagging

Identification of jets originating from b-quarks (b-tagging) is a matter of great importance for the sake of background suppressing in top-quark analyses since the top-quark decays almost exclusively into a W-boson and a b-quark.

Algorithms used for tagging jets with b-quarks exploits various specifics of b-quarks such as long lifetime $\mathcal{O}$ (10^{-12} s) relative to light quark jets and large B-hadron mass. The long lifetime of b-flavoured hadrons relative to light quarks yields a significant $c\tau$[1]The distance traversed by a particle defined as multiplication of the speed of light, c, and the lifetime of the particle, τ. which leads to a measurable secondary vertices and impact parameters of the decay products. Two different impact parameters, transverse (d_0) and longitudinal (z_0), are defined as the transverse (r/ϕ-projection) and z-coordinate of a track at the point of closest approach of the track to the primary vertex, respectively. The b-tagging algorithm used in the presented analysis is the MV1 algorithm. This is a neural network-based algorithm that makes use of the output weights of the IP3D, SV1 and JetFitterCombNN taggers [65].

The IP3D is a high-performance tagger that exploits a likelihood ratio technique. By this technique input variables are compared to pre-defined distributions, obtained from MC simulations, for both the b- and light jet hypotheses. The distributions used for the likelihood are two-dimensional histograms of the signed transverse impact parameter significance d_0/σ_{d_0} and the longitudinal impact parameter significance z_0/σ_{z_0} of tracks.

The SV1 tagger is based on use of secondary vertex. The inclusive vertex formed by the daughter particles of the B-hadron can be sought by building all two-track pairs that compose a good vertex using only tracks far enough from the primary vertex but associated to the jet. Then all tracks from the remaining two-track vertices are iteratively combined into a single inclusive vertex excluding the worst track at each iteration until the χ^2 of the vertex fit is sufficiently good. The SV1 tagger exploits three characteristics of the vertex:

- the invariant mass of all tracks associated to the vertex,
- the ratio of the sum of the energies of the tracks in the vertex to the sum of the energies of all tracks in the jet,
- and the number of two-track vertices.

The aforementioned likelihood ratio technique is used to combine the these three characteristics. A two-dimensional distribution of the first two and a one-dimensional distribution of the last characteristics as well as the distance between the jet axis and the line connecting the primary vertex to the secondary one are the inputs to SV1 tagger.

[1] 1

The JetFitterCombNN is a neural network-based combination of the IP3D and JetFitter taggers where the latter is designed to exploit the topology of weak B- and C-hadron decays inside the jet. By default, the neural network is trained to maximise rejection of light jets.

4.1.4 Offline selection

Jet candidates are reconstructed with the anti-k_t [60] (R = 0.4) algorithm starting from topological clusters. The topological clusters are built from the energy deposited in the calorimeter cells and calibrated using the local cluster weighting (LCW) method [61]. This method partially corrects the jet energy response and reduces fluctuations due to the non-compensating nature of ATLAS Calorimetry. Jets are selected with a kinematic acceptance of $p_T > 25$ GeV and $|\eta| < 2.5$. Jets are also required to have a $|\text{JVF}| > 0.5$, which achieves optimal efficiency of hard scatter jets selection versus rejection of pile-up jets, while an efficient selection of hard scatter jets is maintained. The jet vertex fraction is defined as the fraction of the total transverse momentum of the jet's associated tracks that is contributed by tracks from the PV. The closest jet to a good electron candidate is rejected if $\Delta R(e, j) < 0.2$. Furthermore, any jet within a cone of $\Delta R = 0.1$ with respect to a reconstructed *tight* photon described above is also discarded to avoid double-counting photons being also reconstructed as jets.

4.2 Electrons

One of the possible final state particles of the top-quark pair production is an isolated electron with a high transverse momentum. An efficient reconstruction and identification of electrons is of crucial importance since a lot of background contribution with an isolated electrons exist: electrons from heavy flavours and Dalitz decays, and photon conversions originating from neutral pion decays and jets.

4.2.1 Trigger

Electron objects used in this analysis are required to match the lowest non-pre-scaled single electron trigger, `EF_e24vhi_medium1`. These triggers represent a full chain of triggers that are composed of L1 and L2 triggers. `L1_EM18VH`→ `L2_vh_medium1` → `EF_e24vhi_medium1`. In this naming conventions, The `V` component in the L1 name and the The `v` component in the EF name denote a varied threshold. It is effectively a coarse dead material correction applied on a single L1 ECAL trigger threshold. The `H` in the L1 name denote the hadronic core isolation. This cut leads to inefficiency in selecting electron objects with $E_T \gg 200$ GeV in comparison with offline selection cuts. For this reason, another single electron trigger, `EF_e60_medium1` is employed to mitigate the problem. This trigger also recovers some efficiency loss for $E_T > 80$ GeV by removing the cut on the ECAL back energy fraction. The `EF_e24vhi_medium1` trigger contains application of a loose track isolation, $p_T^{cone20}/E_T > 0.1$.

4.2.2 Reconstruction

The reconstruction procedure of electrons [66] is based on information from the ECAL and the ID. The procedure commences with the formation of a preliminary set of seed clusters.

In order for this, formation clusters with energies above 2.5 GeV are formed by the so-called *sliding-window-algorithm*, where a fixed-size *window* defined in $\Delta\eta \times \Delta\phi$ is moved around over the calorimeter cells until finding a position where the energy deposition within the window is maximal. These clusters of energy depositions then form the seed clusters.

The reconstruction of seed clusters is followed by the track reconstruction. For each seed cluster fulfilling loose shower shape requirements of $R_\eta > 0.65$ and $R_{had} > 0.1$ a region-of-interest (ROI) with a cone-size of ΔR=0.3 around the seed cluster barycentre is defined. The collection of these seed cluster ROIs is retained for use in the track reconstruction which is performed in two steps: pattern recognition and track fit. Tracks in these ROIs with a transverse momentum larger than 1 GeV are reconstructed with a pattern recognition algorithm based on Kalman filter-smoother formalism. The tracks are then fitted using the ATLAS Global χ^2 Track Fitter. Next step of the procedure is association of the seed clusters with reconstructed tracks from the ID. This is performed by extrapolating reconstructed tracks from their last measurement point to the second layer of the calorimeter. Tracks are considered as loosely matched to an ECAL cluster if the distance between their impact point η and ϕ coordinates and corresponding η and ϕ coordinates of the seed cluster in that layer is below a certain threshold taking the bending direction of tracks into account. At this point, all electron-track candidates are defined. The track parameters of these candidates, except for the TRT-only tracks, are precisely re-estimated using an optimised electron track fitter, the Gaussian Sum Filter (GSF) algorithm, which is a non-linear generalisation of the Kalman filter algorithm. A better estimate of the electron track parameters is possible with this algorithm, especially of those in the transverse plane, by taking the non-linear bremsstrahlung effects into account. TRT-only tracks and other very rare tracks (about 0.01%) that fail the GSF fit keep the parameters from the Global χ^2 Track Fit. These tracks are then used to perform the final track-cluster matching to build electron candidates and also to provide information for particle identification.

An electron is reconstructed if at least one track is matched to the seed cluster. In a medium with a lot of jet activity, such as proton-proton collisions, matching of more than one track to the same seed cluster is quite possible. Although all tracks assigned to a cluster are stored, the best matched track is to be the primary track which is used to determine the characteristics of the electron and to make a decision for the identification of the electron. For this reason, the determination of the primary track is quite important. To favor the primary electron track and to avoid random matches between nearby tracks in case of cascades due to bremsstrahlung, tracks with at least one hit in the Pixel detector are preferred. If more than one associated track has pixel hits, a further procedure is required involving the distance between the track and the cluster for each of the tracks. Finally, all seed clusters together with their matching tracks are treated as electron candidates. Each of these electron clusters is then rebuilt in all four layers sequentially, starting from the middle layer, using 3×7 (5×5) cells in the barrel (end-caps) of the ECAL accordion calorimeter. The cluster position is adjusted in each layer to take into account the distribution of the deposited energy.

4.2.3 Identification and offline selection

Electrons are identified by means of a selection based on sequential cuts applied on calorimeter, tracking and isolation variables. Depending on fails or passes of the cuts, electrons are classified as *loose*, *medium* or *tight*. In order to take into account the varia-

tion of the electrons characteristics the selection is optimised in ten $|\eta|$ and eleven E_T bins. Definition of said cuts and the requirements for the three groups are given in tables 4.1 and 4.2.

Variable	Description	Symbol
Hadronic leakage	Ratio of E_T in the first sampling of the hadronic calorimeter to E_T of the ECAL cluster (range: $\|\eta\| < 0.8$ and $\|\eta\| > 1.37$)	R_{had1}
	Ratio of E_T in the the hadronic calorimeter and E_T of the ECAL cluster (range: $\|\eta\| > 0.8$ and $\|\eta\| < 1.37$)	R_{had}
Back layer of ECAL	Ratio of the energy in the back layer to the total energy in the ECAL accordion calorimeter	f_3
Middle layer of the ECAL	Lateral shower width $\sqrt{(\Sigma E_i \eta_i^2)/(\Sigma E_i) - ((\Sigma E_i \eta_i)/(\Sigma E_i))^2}$ where E_i is the energy and η_i is the pseudo-rapidity of cell i and the sum is calculated within a window of 3×5 cells	$W_{\eta 2}$
	Ratio of energies in 3×3 versus 3×7 cells centred at the electron cluster energy	R_ϕ
	Ratio of energies in 3×7 versus 7×7 cells centred at the electron cluster energy	R_η
Strip layer of the ECAL	Shower width, $\sqrt{(\Sigma E_i (i - i_{max})^2)/(\Sigma E_i)}$ where i runs over all strips in a window of $\Delta\eta \times \Delta\phi \approx 0.0625 \times 0.2$, corresponding typically to 20 strips in η, and i_{max} is the index of the highest-energy strip	ω_{stot}
	Ratio of the energy difference between the largest and second largest energy deposits in the cluster over the sum of these energies	E_{ratio}
	RRatio of the energy in the strip layer to the total energy in the ECAL accordion calorimeter	f_1
Track quality	Number of hits in the B-layer (discriminates against photon conversions)	$n_{\text{b-layer}}$
	Number of hits in the pixel detector	n_{pixel}
	Number of total hits in the pixel and SCT detectors	n_{si}
	Transverse impact parameter	d_0
	Significance of transverse impact parameter defined as the ratio of d_0 and its uncertainty	σ_{d_0}
	Momentum lost by the track between the perigee and the last measurement point divided by the original momentum	$\Delta p/p$
TRT	Total number of hits in the TRT	n_{TRT}
	Number of hits in the pixel detector	F_{HT}

Table 4.1.: Description of the variables used for the electron identification.

Variable	Description	Symbol
Track-cluster matching	$\Delta\eta$ between the cluster position in the strip layer and the extrapolated track	$\Delta\eta_1$
	$\Delta\phi$ between the cluster position in the middle layer and the extrapolated track	$\Delta\phi_2$
	Defined as $\Delta\phi_2$ but the track momentum is rescaled to the cluster energy before extrapolating the track to the middle layer of the calorimeter	$\Delta\phi_{\text{res}}$
	Ratio of the cluster energy to the track momentum	E/p
Conversions	Veto electron candidates matched to reconstructed photon conversions	isConv

Table 4.1.: Description of the variables used for the electron identification.

Variable	Loose	Medium	Tight
$R_{\text{had}(1)}$	✓	✓	✓
f_3	✗	✓	✓
$W_{\eta 2}$	✓	✓	✓
R_η	✓	✓	✓
R_ϕ	✗	✗	✗
ω_{stot}	✓	✓	✓
E_{ratio}	✓	✓	✓
f_1	✗	✗	✗
$n_{\text{b-layer}}$	✗	✓	✓
n_{pixel}	✓	✓	✓
n_{si}	✓	✓	✓
d_0	✗	✓	✓
σ_{d_0}	✗	✗	✗
$\Delta p/p$	✗	✗	✗
n_{TRT}	✗	✓	✓
F_{HT}	✗	✓	✓
$\Delta\eta_1$	✓	✓	✓
$\Delta\phi_2$	✗	✗	✓
$\Delta\phi_{\text{res}}$	✗	✗	✗
E/p	✗	✗	✓
isConv	✗	✗	✓

Table 4.2.: Definitions of the identification menus in terms of the cuts applied.

The reconstruction of candidates are described in section 4.2.2. The offline selection requires the candidates to be reconstructed within the region of $|\eta_{\text{cl}}| < 2.47$, excluding

the transition region of $1.37 < |\eta_{\text{cl}}| < 1.52$ in the ECAL, and with a transverse energy of $E_T > 25$ GeV. Transverse energy is defined as in terms of the cluster energy and the direction of the candidate by means of the following formula: $E_T = E/\cosh(\eta)$. The candidates are also required to fulfil the `Tight++` criteria: A set of tight isolation cuts is imposed on the candidates aiming for an improvement on the suppression of the multi-jet background. The imposed cuts are a combination of electromagnetic cluster and track isolation cuts and tuned to achieve uniform isolation efficiency with respect to certain offline electron selection over the η_{cl} and E_T spectra. The former is ECAL isolation of $\Delta R = 0.2$ at the working point of 90% efficiency and denoted as `EtCone20@90` and where the latter is a track isolation of $\Delta R = 0.3$ at 90% efficiency and denoted as `PtCone30@90`. Furthermore, in ATLAS it is fairly possible that electrons and jets can spoil each other's reconstruction process. In order to avoid any misidentification of objects, two different overlap removal strategies are followed. The first requires removal of jets that exist within the volume of $\Delta R = 0.2$ around the selected electron. The second requires removal of electrons, in case an additional jet is to be found within the volume of $\Delta R = 0.4$.

4.2.4 Efficiencies and Scale Factors

The efficiency (ϵ) of selected electrons can be factorised into efficiencies of individual requirements that a final electron object is required to have. This factorisation can be formulated as

$$\epsilon = \epsilon_{\text{reco}} \cdot \epsilon_{\text{id}} \cdot \epsilon_{\text{iso}} \cdot \epsilon_{\text{trig}}, \tag{4.3}$$

where the four individual efficiencies denote the reconstruction, identification, isolation and the trigger efficiencies. The reconstruction and identification efficiencies are estimated in data and $Z \to ee$ Monte Carlo samples by the `egamma` working group of the ATLAS collaboration. They are estimated using the Tag&Probe method [67] and translated into scale factors as described in the equation above, which are applied to the Monte Carlo simulated events. The reconstruction efficiency is estimated to be ∼98% and the identification (`Tight++`) efficiency to be ∼80% for isolated electrons from $Z \to ee$ events. The isolation efficiencies, i.e. `EtCone20@90` and `PtCone30@90`, are defined with respect to `Tight++` identification (i.e 90% for `Tight++`), while the efficiencies for the trigger, `EF_e24vhi_medium1 || EF_e60_medium1`, are determined with respect to the combination of `Tight++` and isolation cuts. Scale factors are binned in 2D (η and E_T)utilising the following 1D×1D factorisation

$$\text{SF}_{\eta,E_T} = \text{SF}_{\eta} \times \frac{\text{SF}_{E_T}}{\text{Average SF}}. \tag{4.4}$$

4.2.5 Offline selection

Electron candidates are required to have a p_T larger than 25 GeV and a cluster $|\eta|$ smaller than 2.47. The transition region between the ID and the ECAL, which corresponds to $1.37 < |\eta_{cl}| < 1.52$, is excluded from the η acceptance. Electron candidates are also required to satisfy the `Tight++` criteria as well as the ID-based and the ECAL-based isolation requirements. The ID-based isolation is defined as the scalar sum of all tracks in the ID with a p_T larger than 1 GeV within a cone of $\Delta R = 0.3$ around the electron and denoted as p_T^{cone30}. Similarly, the ECAL-based isolation is defined as the sum of energy deposits in the ECAL within a cone of $\Delta R = 0.2$ around the the electron and denoted as E_T^{cone20}. Both isolation cuts are applied in 9×9 $E_T \times \eta$ bins.

4.3 Muons

4.3.1 Trigger

For this analysis, the triggers to be used for the muon objects are the single muon triggers are `EF_mu24i_tight` and `EF_mu36_tight`. These triggers differ by the p_T threshold, as well as the isolation applied in the `mu24_tight` trigger.

The `mu24i_tight` trigger is designed for selecting muons with a transverse momentum larger than 25 GeV and a loose isolation criterion of $\Sigma_{\Delta R<0.2} p_T^{trk}/p_T < 0.12$. In words, the sum of the tracks transverse momenta in a cone of size 0.2 around the muon is required to be less than 12% of the muon transverse momentum. This criterion is optimised to retain nearly 100% efficiency for selecting well isolated muons from $Z \to \mu\mu$ decay while rejecting slightly over half of the muons from heavy flavour, pion and kaon decays. The to be offline applied mini-isolation is tighter than this isolation. However, this isolation, applied at the trigger level, doesn't affect the analyses.

No isolation requirement is made in the `EF_mu36_tight` trigger.

4.3.2 Reconstruction and Identification

Muons are reconstructed by using information mainly from two sub-detectors, the MS and the ID, and are referred to as *combined muons*.

Stand-alone (SA) muons are reconstructed using only the information from the MS. The parameters of the muon track are determined by extrapolating the information of the track at the interaction point to the point of closest approach to the beam line. They are used to extend the acceptance to the range of $2.5 < |\eta| < 2.7$.

Combined (CB) muons are the main type reconstructed muons. The tracks are reconstructed independently in the ID and MS and combined. The CB candidates have the highest muon purity.

Segment-tagged (ST) muons require a track in the ID in association with at least one local track segment in the MDT or CSC chambers.

Calorimeter-tagged (CaloTag) muons require a track in the ID in association with an energy deposit in the calorimeter compatible with a ionising particle. This type has the lowest purity but muons in the non-instrumented acceptance of the MS are reconstructed by this type.

The reconstruction of the CB muon candidates utilises two independent reconstruction algorithms. The algorithms include different strategies [68], so-called *chains*, both for the reconstruction in the MS and for the ID-MS combination. The latter utilises a chain (Chain 1) that performs a statistical combination of the track parameters for the SA and ID muon tracks using the responding covariance matrices. A second chain (Chain 2) performs a global refit of the muon track using the hits from both the ID and the MS subdetectors. The advantage of using two independent codes is redundancy and robustness in the ATLAS commissioning phase.

The CB algorithm requires a set of quality criteria applied to the ID tracks:

- at least one Pixel detector hit
- at least five SCT hits
- at most two active Pixel or SCT sensors traversed by the track but without hits
- at least nine TRT hits in the region of the full TRT acceptance ($0.1< |\eta| <1.9$)

The above requirements are dropped in the region $|\eta| > 2.5$, where short ID track segments can be matched to SA muons to form a CB muon. In ATLAS top-quark working group only combined muon identification is used.

4.3.3 Offline Selection

The criteria for the muon object selection are optimised by the *Muon Combined Performance* group of the ATLAS collaboration as follows:

- Muons are required to be reconstructed within the detector acceptance, $|\eta| < 2$.
- A cut of $p_T > 25$ GeV is set to be on the plateau of the single muon trigger efficiency.
- Muons must pass the ID track quality cuts defined above.
- The longitudinal impact parameter relative to the primary vertex is required to be less than 2 mm.
- Selected muons are required to be distanced $\Delta R(\mu, j) > 0.4$, where j is any jet with $p_T > 25$ GeV and $|\text{JVF}| > 0.5$.
- The muon is required to pass the *mini-isolation* requirement described below.

Mini-Isolation

At the high energy regime of the LHC, the top-quarks produced can carry large momentum, boosting the top decay products in the lab frame. Such boosting can make the lepton very close to the b-quark in a leptonic top-quark decay. This leads to low efficiency for usual isolation criteria used in 7 TeV analyses. These criteria are needed to be either loosened or removed to maintain a high efficiency in the boosted region. One of the criteria to be removed is the normal calo- and track-based isolation. But the removal of this isolation would cause a problem in terms of rejecting leptons from QCD jets which has a high production rate at the LHC. The so-called *mini-isolation* [58] is the solution at this point which exploits the fact that the angular separation between the decay product is proportional to the mass of the mother particle over its momentum. Unlike the traditional fixed-cone isolation, mini-isolation collects energy around the lepton with a variable cone size. The cone size decreases as the momentum of the lepton increases. As the mass of top quark is much heavier than that of other quarks and gluons, the prompt lepton from boosted top quarks will generally be more separated from the jets, in comparison to non-prompt lepton from QCD jets of a similar energy scale. With proper configuration, the mini-isolation would approximate zero for leptons from boosted top, while counting considerable energy for non-prompt leptons. A track-based mini-isolation is defined as

$$I^l_{mini} = \sum_{tracks} p_T^{track}, \Delta R(l, track) < K_T/p^l_T. \tag{4.5}$$

The tracks are selected with the same criteria as standard fixed-cone track isolation, which is robust against pileup contamination. Calo-based isolation is not considered because calorimeter angular resolution is limited. One configuration, shown to be optimal, is K_T =10 GeV, with a max value of ΔR as 0.4. The optimised cut value is determined to be smaller than 5% of the lepton p_T.

4.4 Photons

4.4.1 Reconstruction

The reconstruction of photons is carried out in parallel with that of electrons since both objects leave very similar signatures behind in the calorimeter. Nevertheless, being a charged particle, the definition of an electron object is rather straightforward where the things are a bit more complicated for photons due to their conversion. For this reason, photons are classified into two categories: unconverted and converted photons. Unconverted photons are not associated with any track, they are simply ECAL clusters. Converted photons are characterised with at least one track originated from a vertex in the ID and associated with a cluster in the ECAL. Therefore, there is a significant similarity between electrons and converted photons. Here discussed only specifics to the converted photon reconstruction since the overall reconstruction algorithm is explained in detail in section 4.2.2.

Converted photons are classified into two groups depending on the number of assigned tracks. Converted photons are typically assigned with two tracks. However, they can be assigned with only one track, in case the track of either electron or positron is failed to be reconstructed. This would be possible either when the transverse momentum of the track is very low or when the tracks of electron and positron are very close to each other ending up with being impossible to be separated adequately.

The first stage of the reconstruction of converted photons is the reconstruction of the conversion vertices within the tracker. The first stage is then followed by the reconstruction and association of conversion vertices to an ECAL cluster. In the former case, conversions with two assigned tracks, conversion vertex is reconstructed using oppositely charged track pairs that are likely to be electrons. This likelihood is based on hits in the TRT and the silicon detectors, and is required to be over a certain threshold. The conversion vertex is then reconstructed by performing a constrained vertex fit with three degrees of freedom and using the five helix parameters of each of the two participating tracks. The constraint of the fit is the requirement for tracks to be parallel at the vertex. The latter case, conversions with only one track, is mostly to occur in the outermost layers of the ID. Therefore, tracks without hits in the b-layer that either have a very high likelihood to be an electron, or have no hits in the TRT, are considered as conversion vertex candidate with a single track. In such cases, the conversion vertex is simply defined to be the coordinates of the first measurement of the track since a vertex fit is not possible to perform.

As in the track matching for electrons, the conversion vertices are matched to the clusters by exploiting an extrapolation of the conversion candidates the second sampling layer of the ECAL. The details of the extrapolation can be read elsewhere [69]. Conversion vertex candidates reconstructed from tracks with hits in the silicon detectors are then considered matched to a cluster if the extrapolated vertex and the cluster centre are closer than 0.05 in both η and ϕ. In case of the extrapolation of a conversion vertex with single track the limit on the size of ϕ window is doubled in the direction of bending. If multiple conversion vertex candidates are matched to the same cluster, the preference is adjusted by considering candidates with more assigned tracks, with more hits in the silicon detectors and with smaller vertex radius.

The final arbitration between the unconverted photon, converted photon and electron hypotheses for the reconstructed ECAL clusters is performed considering the presence or lack of tracks, number and overlap of tracks as well as their hits in the silicon detectors, and the transverse momentum and energy of assigned tracks.

As a result of studies performed using MC simulations, the reconstruction efficiency of prompt photons with E_T >25 GeV is expected to be 96 percent. The rest is incorrectly

reconstructed as electrons. The reconstruction efficiency of photons in the lower transverse momentum region, i.e. a few tens of GeV, is studied using data [70]. The study points to inefficiencies and fake rates that exceed by up to a few per cent the predictions from MC simulation. The reconstruction efficiency for photons in the large transverse energy region, i.e. E_T >150 GeV, decreases as the separation of tracks originating from conversions starts to become a problem.

The final photon energy is measured using ECAL information on the cluster size that depends on the photon classification. In the barrel region, the cluster size used for unconverted photons is $\Delta\eta \times \Delta\phi$=0.075×0.123 while it is $\Delta\eta \times \Delta\phi$=0.075×0.172 for the converted photons to compensate for the opening between the conversion products in the ϕ direction caused by the magnetic field of the ATLAS solenoid. The cluster size in the end-cap is same for all type of candidates and is $\Delta\eta \times \Delta\phi$=0.125×0.123. The calibration performed on the photon energy, which takes upstream energy loss and both lateral and longitudinal leakage into account, shares the same procedure that is used for electrons [70, 67].

4.4.2 Identification

Distinguishing between prompt and background photons with high signal efficiency and background rejection is of great importance. The photon identification strategy makes use of a set of cuts on discriminating variables that characterises the lateral and longitudinal shower development in the ECAL and the shower leakage fraction in the HCAL.

Originating from hard scattering and being emitted before hadronisation time scale, prompt photons are typically isolated since they do not suffer from nearby jet activity. Furthermore, background candidates from Dalitz decays (i.e. $\pi \to \gamma\gamma$) are often characterised by two local energy maxima separated in the finely segmented strips of the first layer, due to small separation between the two photons caused by the solenoid magnet. The typical characteristics of prompt photons differing from background photons are narrower energy deposits in the ECAL and smaller leakage to the HCAL. Both in-time and out-of-time pile-up processes affect the distributions of the discriminating variables for both the prompt and background photons. Pile-up processes lead to low-E_T activity in the detector, energy depositions in the ECAL and consequently an effect that is tendentious to broaden the distributions of the discriminating variables and thus a blurring effect on the separation between prompt and background photon candidates.

The identification of photons are grouped into two, *loose* and *tight*, selections. The *loose* selection is based only on shower shapes in the second layer of the ECAL and on the energy depositions in the HCAL. The *loose* selection is designed aiming for a high prompt-photon identification with respect to reconstruction. The *loose* selection achieves an average efficiency of 98% for both converted and unconverted photons. The corresponding background rejection factor is about 1000[1]. The *tight* photons are selected by processing information from the finely segmented strip layer of the calorimeter on top of the *loose* selection information. This additional information provides good rejection of jets originating from hadrons where a neutral meson carries most of the energy. The *tight* selection criteria are optimised for converted and unconverted photons separately providing an average identification efficiency of about 85% for photons with E_T >40 GeV and a corresponding background rejection factor of 5000 [69]. Taking into account the

[1]The rejection factor is defined as the ratio of the number of initial jets with p_T >40 GeV in the acceptance of the calorimeter to the number of reconstructed background photon candidates satisfying the identification criteria.

different detector geometry over the η region, the selection criteria are different in seven intervals of the reconstructed photon pseudo-rapidity.

4.4.3 Offline selection

Photon candidates are required to have a minimum transverse momentum of 15 GeV within the acceptance of $|\eta_{cl}| < 2.37$ excluding the transition region of the ECAL $1.37 < |\eta_{cl}| < 1.52$. In addition to the OQ flag, *photon cleaning* requirements (LAr quality factor cleaning + a timing cut to reject out-of-time candidates) are applied. For the photon identification, the `PhotonIDTool` is used with cut-menu 2012 for *tight photon identification*, which are both provided by *EGamma Working Group* of ATLAS collaboration.

4.5 Missing Transverse Energy

An important signature of the semi-leptonic and dilepton top-quark pair decay modes is large missing energy $\not{E}_T$ (cf. Section 3.3.1) since the neutrino from the leptonically decaying W-boson traverses throughout ATLAS without being detected. This quantity is also a powerful instrument to distinguish between $t\bar{t}$ events and backgrounds that do not contain $\not{E}_T$ such as Drell-Yan processes.

In the top-quark analyses, the missing energy is computed using an object based reconstruction algorithm that relies on the use of calibrated cells associated with identified high-p_T objects by replacing the initial cell energies with the modified refined calibration. The objects used are electrons, photons, jets and muons denoted as *RefEle, RefGamma, RefJet and RefMuon*. In *RefEle*, cells with cluster corrections at the EM scale are considered. The Jet component *RefJet* includes only LC+JES calibrated cells. In order to avoid any possible double counting, cells associated to multiple objects are resolved by considering only the first association. Jets with low p_T, from 10 GeV to 20 GeV, are grouped into a dedicated term named *SoftJet*. Cells not associated to any high-p_T objects are considered under the term *CellOut* separately. The missing energy can then finally be formulated as the sum of components defined above where *SoftJets and CellOut* terms are collectively referred to as *SoftTerms*.

$$E_{x,y}^{Miss} = E_{x,y}^{Ele} + E_{x,y}^{RefPhoton} + E_{x,y}^{RefJet} + E_{x,y}^{RefSoftJet} + E_{x,y}^{RefMuon} + E_{x,y}^{CellOut}, \qquad (4.6)$$

and the magnitude is given by

$$E_T^{Miss} = \sqrt{(E_x^{Miss})^2 + (E_y^{Miss})^2}. \qquad (4.7)$$

4.6 Data sample

The data analysed in this analysis was collected by the ATLAS detector at the LHC in 2012. The collisions are recorded at a centre-of-mass energy of $\sqrt{s}$ =8 TeV with a bunch spacing of 50 ns between the proton bunches and with 1380 proton bunches per proton beam. The total amount of delivered data luminosity, as can be seen in figure 3.3, is 22.8 fb^{-1} and the recorded data is 21.3^{-1}. However, approximately 5% of the recorded data does not fulfil the data quality requirements. The ultimate amount of data available for physics analysis is 20.2 fb^{-1}.

The data is streamed into three branches by using informations from trigger systems of different components of the detector: `Egamma` stream is triggered by the energy deposits in

the ECAL, `Muon` stream is by the signals in the MS and finally `JetTauEtMiss` stream is by deposits in HCAL. The use of the each stream is depends on the process being analysed which will be pointed out in the flow of the analysis.

4.7 Simulated samples

4.7.1 Signal samples

The signal $t\bar{t}\gamma$ sample is simulated with the matrix element generator MadGraph [71]. The sample is simulated taking only $t\bar{t}$ intermediate state into account as listed below:

- $pp \to t\bar{t} \to \bar{l}\nu_{\bar{l}}bq\bar{q}\bar{b}\gamma$
- $pp \to t\bar{t} \to q\bar{q}bl\bar{\nu}_{l}\bar{b}\gamma$
- $pp \to t\bar{t} \to \bar{l}\nu_{\bar{l}}bl\bar{\nu}_{l}\bar{b}\gamma$

where $q\bar{q}$ pairs are pairs of a quark(anti-quark) and the anti-particle (particle) of its isospin partner, i.e. $u\bar{d}, c\bar{s}, d\bar{u}, s\bar{c}$. The colliding partons are either two gluons or a quark-anti-quark pair and incoming protons are modelled by a LO PDF set, CTEQl1 [72].

All three lepton generations are included in the simulation. All quarks except for b-quark, and electrons are considered as massless.

The muon mass is considered as 0.105 GeV, the tau mass as 1.777 GeV, b-quark mass as 4.7 GeV and finally top-quark mass as 172.5 GeV.

The fine structure constant is considered as 1/137while the strong coupling constant is running. The renormalisation and factorisation scale factors are set to $2m_t$ and the colliding protons are modelled by a LO PDF, CTEQ6L1.

In order to avoid infrared and collinear singularities, the sample is simulated with a set of kinematic cuts:

- Photon p_T threshold of 10 GeV and $|\eta|$ acceptance limit of 5.0.
- Lepton p_T threshold of 15 GeV.
- Minimum ΔR distance of 0.2 between the photon and all other charged particles.

With the setting above, the total cross sections of the simulated sample reads 1190.7 fb. The simulated sample is then matched to PYTHIA [73] fro the further simulations of parton showering and soft interactions(i.e. underlying events). Additional radiations of QED phenomenon is simulated by PHOTOS [74]. Finally, sample is passed to the detector simulation GEANT4 [75] in order to simulate the detector response on the simulated data.

4.7.2 Variation signal samples

Apart from the phase space cuts, the modelling related parameters and tools used in the simulation of the signal sample like the choice of QCD scales, parton shower, PDF set and such are needed to be assigned with systematic uncertainties. In oder to do this, different variations of the signal sample are simulated with same phase space cuts but by varying a parameter or a tool at a time. For instance considering the choice QCD scales, a sample for which the QCD scales are set to m_t, and considering the choice of parton shower a sample which is matched to Herwig/Jimmy is produced. In oder to shorten computing

time, the variation samples are produced with reduced statistics, i.e. half the nominal sample, and a fast simulation of detector modelling, i.e. AltFastII [76], is used. The full list of produced samples is given in Appendix A.

4.7.3 Background samples

The simulations of $W+$ and $Z+\gamma$ samples are performed using SHERPA [77] with up to three jets. The $b-$ and $c-$ quarks are considered massless. The contributions from these processes are normalised to the LO cross sections from SHERPA. An additional $W-$boson sample is simulated using ALPGEN generator with interfacing to PYTHIA.

The single top-quark samples, all three channels, are simulated by POWHEG [78]. The sample for t-channel is simulated with a NLO PDF set, CT10F4, and the samples for the other two channels are simulated with another NLO PDF set, CT10. The parton shower and hadronisation modelling is handled with p2011C tune [79].

The diboson samples, $WW+\gamma$, $WZ+\gamma$ and $ZZ+\gamma$ are simulated using ALPGEN generator and interfaced with Herwig/Jimmy [80, 81] for parton showering.

Chapter 5

Event selection

The selection of signal events is characterised and optimised by taking the topology and kinematics of the signal final state into account. The single lepton $t\bar{t}\gamma$ final state consists of an isolated lepton[1] with a high p_T, high missing transverse energy ($\not{E}_T$) originating from the neutrino coming from the leptonically decaying W-boson, two b-tagged jets and two high p_T jets from the hadronically decaying W-boson and finally an isolated photon with high p_T. Another more important input to the optimisation of the event selection is the physics result pursued. As mentioned in the introduction, the analysis aims for measuring the part of $\sigma_{t\bar{t}\gamma}$, where the photons are radiated off the top-quark and not off its decay products. Motivated by this point, the event selection also includes cuts that are considered to help to enrich the selected signal events with photons radiated off top-quarks.

- The selection starts by requiring a lepton trigger, depending on the data period.
- Presence of a primary vertex with at least four associated tracks is required.
- According to the trigger fired, the events are separated into the electron and muon channels. Depending on this separation, the events must contain either exactly one electron or muon having a threshold p_T of 25 GeV. The electrons and muons are required to be matched to the online trigger object.
- In both channels, presence of at least four jets reconstructed with a p_T larger than 25 GeV and within an η acceptance of 2.5 is required.
- In the electron channel, an $\not{E}_T$ of 30 GeV and a W-boson transverse mass larger than 30 GeV are required. In the muon channel, an $\not{E}_T$ is required to be larger than 20 GeV and the system of $\not{E}_T$ and W-boson transverse mass (m_T^W) is required to be higher than 60 GeV. These high requirements on the $\not{E}_T$ and m_T^W aim to suppress the high level of multi-jet background at the LHC. Multi-jet events are characterised by being balanced on the transverse plane. Therefore, a high $\not{E}_T$ is a good indication of the presence of a process with a neutrino in the final state such as $t\bar{t}$ production with at least one leptonically decaying W-boson. The cut on m_T^W also provides a good distinction power between events with true W-bosons and multi-jet events or Z+jets events.

[1] It can be any of the three charged leptons. However, in this analysis only electrons and muons are considered.

- In order to suppress various backgrounds but mainly W+jets+γ events, at least one b-tagged jet is required.
- Exactly one photon reconstructed with a p_T of at least 15 GeV and within the η acceptance of 2.47 must be present in the event. The transition region between the barrel and end-cap calorimeters are excluded as for the electron objects.
- In the electron channel, the invariant mass of the electron and the photon system is required to be outside a $\pm$5 GeV mass-window around the Z-boson mass, in order to suppress Z+jets events with one of the electrons misidentified as a photon.
- Events with a jet within the cone of ΔR=0.5 around the selected photon are rejected to suppress events with photon radiation from jets.
- For further suppression of events with photon radiation from decay products, the distance between the selected lepton and photon is required to be larger than ΔR=0.7.

This selection yields 1256 and 1816 data candidate events in the electron and muon channels respectively. The MC yields for the signal selection are predicted to be 440$\pm$90 and 720$\pm$140 events with taking a k-factor of 1.90 into account. The cut flows for data candidates are presented in table 5.1. The kinematic distributions of photons from the selected events are presented in figure 5.1, where the data distributions are compared to MC predictions of the signal and the backgrounds.

Table 5.1.: The cut-flow of data candidates in the single electron and single muon channels.

Cuts	μ+jets	e+jet
Initial	705961000	71278800
Trigger	218114000	222497000
Trigger Match	103495000	85735100
At least four jets	510571	467423
$\not\!\!E_T$	446636	321982
$m_T(W)$	409136	263659
At least one b-tagged jet	211073	135133
At least one photon	3788	2831
$\lvert\eta_\gamma\rvert$<1.37 or $\lvert\eta_\gamma\rvert > 1.52$	3788	2831
$p_T(\gamma) > 15$ GeV	2644	2128
Exactly one photon	2591	2101
$\lvert m_{inv}(e\gamma) - M(Z)\rvert > 5$ GeV	2591	1894
$\Delta R(\gamma, \text{jet}) > 0.5$	2023	1546
$\Delta R(\gamma, l) > 0.7$	1816	1256

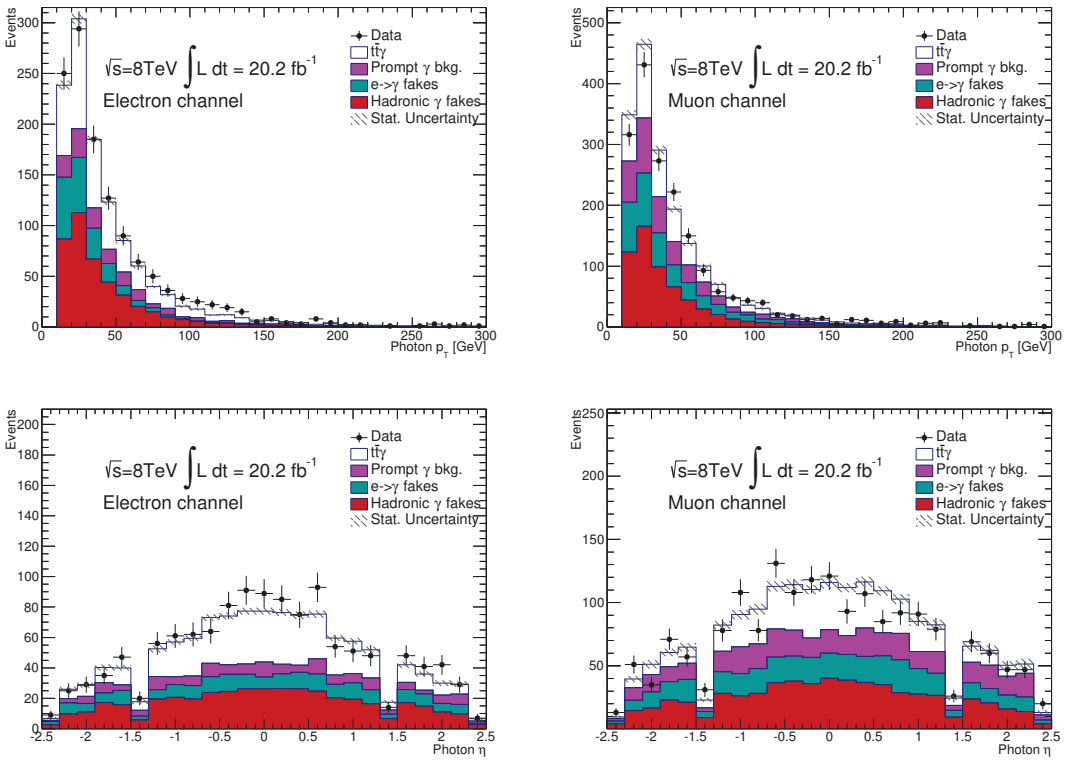

Figure 5.1.: Comparison of data and the expected distributions in the events passing the selection for the single lepton e(left) and μ (right) channel passing the $t\bar{t}\gamma$ selections.The photon p_T and η distributions in the signal region. The hadron fake, $e \to \gamma$ fake, $W\gamma$ and QCD are from data-driven estimation while other backgrounds from MC. The error band includes both statistical and all systematic uncertainties.

Chapter 6

Strategy of the measurement

As it is the case for most high energy physics (HEP) analyses, the strategy of the presented analysis in this thesis is also almost all about distinguishing between signal and background processes. Even a very well optimised event selection is not sufficient to select pure signal events from data. In this measurement for instance, after the event selection around two third of the selected candidate events are background events which have to be estimated and subtracted. For this, one needs to consider the specific features of the signal process being analysed. As mentioned in chapter 5, the signal process of the presented analysis is characterised by an isolated lepton, high missing transverse energy, at least four jets of which at least one is b-tagged and finally an isolated prompt photon with a high transverse momentum. Prompt photons are usually well isolated physics objects since they are produced before the hadronisation process. This feature of photons provide a strong discrimination power between prompt photons and background photons, since most of the background is expected to originate from non-prompt photons. In addition, objects misidentified as photons, *fake photons*, are not well isolated physics objects[1]. Motivated by this reason, the strategy of the analysis is constructed being based on photon isolation. A template fit method is performed by employing RooFit/RooStats framework [82]. The templates to be fitted represent photon isolation distributions of signal and background processes. This chapter discusses the strategy of the cross section measurement.

The chapter starts first with the heart of the strategy, which is the distinction between signal and background photons. Then the construction of the template fit and the modelling of the likelihood function used in the template fit are described. The chapter then continues with the definitions of the cross section and the phase space where the measurement is performed. The chapter finally closes with the motivation and description of the first differential measurement.

6.1 Photon isolation as a discriminator

Probably, the most important point lying in the heart of the strategy is the choice of the discriminant variable used in the template fit, in order for distinguishing between signal and background photons. The photon isolation has been found to distinguish well between the prompt and other types of photons.

Isolation of a photon object, or of an electron, is defined as the scalar sum of either transverse energy or transverse momentum activity within a cone of a certain size around

[1] Backgrounds with prompt photons also contribute but their contribution is estimated separately.

the photon except for the energy or momentum of the photon itself. In order to define isolation of an object in terms of transverse energy, energy deposits in the calorimeter around the object are taken into account, whereas transverse momentum based isolation takes the tracks around the object into account. Transverse energy and transverse momentum isolations are conventionally denoted by $E_T^{cone20/30}$ and $p_T^{cone20/30}$, respectively. The labels in the superscript denote the cone size around the object within which the isolation is calculated. The label $cone20$ indicates the cone size of $\Delta R = 0.2$ and $cone30$ indicates $\Delta R = 0.3$.

A rigorous choice of photon isolation is required, since the photon isolation variable is the discriminator variable in the likelihood fit. Transverse energy isolations depend on the η of the object of which the isolation is calculated, because of the variation in the amount of the material in front of the calorimeter. Objects in the large η region deposit more energy in the ID as they traverse until they reach the ECAL whereas objects in the central region deposit less energy since they have a shorter to distance to reach the ECAL. For this reason, $E_T^{cone20/30}$ isolations are not proper choices for photon isolations.

It is concluded in a number analyses [83, 84] that among those variables p_T^{cone20} is the variable that provides the highest background rejection for a given signal efficiency. Therefore, also in this measurement, p_T^{cone20} is chosen as the isolation discriminator to be used in the template fit. The p_T^{cone20} isolation is calculated by considering tracks having a p_T of at least 1 GeV, at least seven hits in the Pixel and SCT detectors, and a hit in the Pixel b-layer. Tracks associated to conversion vertices closer than 0.1 to the photon in $\eta - \phi$ space are not considered for the isolation calculation. Finally, in order to reduce biases from tracks originating from pile-up interactions, the transverse and longitudinal impact parameters of the tracks with respect to the primary vertex has to be smaller than 1 mm.

6.2 Signal background distinction

There are three different origins of an object that can be seen as a photon by the detector:

Prompt photons: A prompt object is an object that originates from the hard scattering process before the hadronisation of strongly interacting particles starts. In case of the semileptonic channel of top-quark pair production, photons that are radiated off either the incoming quarks or the top quarks or its electrically charged decay products are prompt photons. This type of photon is also the photon object of interest for the final state in this measurement.

Photons faked by electrons: The resemblance of electron and photon objects as well as their reconstruction algorithms are discussed in detail in sections 4.2.2 and 4.4.1. In addition to this resemblance, they are reconstructed from energy deposits in the ECAL by using the same algorithm. As a consequence of this resemblance and the use of the same algorithm, an electron object can be misidentified as a photon, i.e. an electron with a poorly reconstructed track or an electron associated with two tracks, one of which is originated by a close by jet activity. For the details of this misidentification, confer to section 7.2.1.2.

Photons faked by hadrons and by non-prompt photons from decays of hadrons: During the hadronisation process of quarks and jets after the hard interaction, various hadrons such as π^0, η and ρ mesons or baryons are produced. These mesons and baryons can then decay into two or three photons which are eventually seen as photons by the detector. Furthermore, the energy deposit of mesons and baryons themselves can also

fake photons.

Photons with these three different origins differ in isolation. Prompt photons are well isolated objects since they are radiated in the relatively "still" environment before the hadronisation process. Photons faked by electrons also tend to be well isolated but as it will be discussed in section 7.2.4 a remarkable difference from the isolation of prompt photons is observed. Lastly, photons faked by hadrons are not well isolated since they are produced within the busy environment of hadronisation.

Background processes to the signal analysed in this thesis can be categorised in two categories according to the photon types described above:

- Backgrounds with fake photons.
- Backgrounds with prompt photons.

The former category includes all background processes with photons faked by hadrons and electrons while the latter includes background processes with prompt photons. In the template fit, the background processes in the first category, photons faked by hadrons and electrons, are represented by dedicated templates. The background processes of the second category, however, are represented by the same distribution that represents the signal process. This is possible since they all are prompt photons which are not different in terms of their isolation and since all events are selected by the same selection criteria so that they have similar event topologies, e.g. at least four jets requirement.

6.3 Construction of the template fit

The measurement of $\sigma_{t\bar{t}\gamma}$, or any other experimental measurement of a parameter, is an estimation, since the true value is not accessible due to requirement of infinite number of observations. This infers that the precision of a measurement increases with the increasing number of observations. In other words, the measurement estimates a value of $\sigma_{t\bar{t}\gamma}$ as close as possible to the true value given the experimental observations. The measurement is therefore an asymptotic approximation to the true value of $\sigma_{t\bar{t}\gamma}$. While the true value being inaccessible, it is possible, and necessary, to determine an interval of values that contain the true value. This interval is defined as the error of the measurement and often referred to as confidence interval.

Therefore the template fit, of which the output is the estimate($\sigma_{t\bar{t}\gamma}$), has to be constructed by employing a function that describes the observation data. This function is referred to as estimator and its choice is arbitrary. Although the estimator can be arbitrarily chosen, a set of desirable statistical and non-statistical merits of estimators plays a decisive role on this choice. The statistical merits are of more importance and among them the most desirable merit is *minimum loss of information*. In the case of an asymptotic approach, as it is the case in this analysis, the optimal choice to satisfy the merit of minimum information loss is the *maximum likelihood* estimator [85] which is based on a likelihood function.

6.3.1 Modelling of likelihood function

The conditional probability that a real random variable (or a set of N real random variables) $\mathbf{X}$ which is distributed with respect to a probability density function $f(\mathbf{X}|\boldsymbol{\psi})$, where

$\boldsymbol{\psi}$ is a real parameter can be described by a joint probability distribution function of $\mathbf{X}$:

$$P(\mathbf{X}|\boldsymbol{\psi}) = P(X_1, ..., X_N|\boldsymbol{\psi}) = \prod_{i=1}^{N} f(X_i|\boldsymbol{\psi}) \tag{6.1}$$

If the random variable $\mathbf{X}$ is replaced by a set of experimental observations, the P is not a probability distribution function anymore but rather a likelihood function which is conventionally denoted by L:

$$L(\mathbf{X}|\psi) = \prod_{i=1}^{N} f(X_i|\boldsymbol{\psi}) \tag{6.2}$$

The template fit employed in the analysis estimates the parameter of interest, $\sigma_{t\bar{t}\gamma}$, by maximising the likelihood function. The likelihood function employed in the analysis is constructed based on the general description of a likelihood function described above and is formulated as follows:

$$L = \prod_{i,j} P(N_{i,j}|N^s_{i,j} + \sum_b N^b_{i,j}). \tag{6.3}$$

The probability function used here to model the event yield distribution is a Poisson function. The index i denotes the decay channels (e,μ) and the index j denotes the bins of the isolation (p_T^{cone20}) distribution where $N_{i,j}$ is the number of observed data events, $N^s_{i,j}$ is the expected number of signal events and $N^b_{i,j}$ is the number of expected background events in channel i and bin j. The index b for the summation denotes the different sources of backgrounds.

The expected number of signal events, $N^s_{i,j}$, is a function of multiple parameters:

$$N^s_{i,j} = \mathcal{L} \cdot \sigma_i^{fid} \cdot C_i \cdot f^s_{i,j} \tag{6.4}$$

where $\mathcal{L}$ is the integrated luminosity, σ_i^{fid} is the fiducial cross section in channel i, the correction C_i is the ratio of reconstructed events to the number of generated events in the fiducial phase space in channel i and $f^s_{i,j}$ is the fraction of signal events in channel i and bin j. In this parametrisation of $N^s_{i,j}$, the only free parameter is the cross section, σ_i^{fid}. All other parameters are constant.

The number of expected background events is also a function of other parameters, but with a rather simple definition:

$$N^b_{i,j} = N^b_i \cdot f^b_{i,j}. \tag{6.5}$$

Here, N^b_i is the total number of type b background events in channel i and bin j and $f^b_{i,j}$is the fraction of the same type background events in channel i and bin j. In the analysis, there are seven different background sources. In the fit, only one of these backgrounds, the contribution of processes with a photon faked by hadrons, $N^b_i|_{b=hadronicfakes}$ is a free parameter while all others are constant. The likelihood function given in equation 6.3 models only the event yield distribution. Incorporation of systematics into the likelihood function is discussed in the following section. The definition of the estimate, $\sigma_{t\bar{t}\gamma}$, is discussed in further detail in section 6.5.

6.3.1.1 Incorporation of systematic uncertainties into the likelihood

Systematic uncertainties of a measurement are the uncertainties that are not related to the statistics of the measurement in question and should be treated rigorously in order for a reliable and precise evaluation of the confidence interval on the parameter to be measured.

A primitive manner to consider systematic uncertainties is rather a "naive approach" which is a simple propagation of systematic uncertainties into the result. In this approach, a measurement is performed at $\pm 1\sigma$ deviations of a systematic uncertainty and the systematic uncertainty on the measurement is then calculated with numeric error propagation:

$$\sigma_{\mu}(sys) = (\mu_{up} - \mu_{down})/2, \tag{6.6}$$

where μ_{up} and μ_{down} are the $\pm 1\sigma$ deviations of a nominal estimate of a measurement, $\hat{\mu}$. In order to estimate the total systematic uncertainty on the measurement, the procedure is repeated for all systematic uncertainty sources and they are summed quadratically. This approach, however, does not consider the possibility that uncorrelated source of systematic uncertainties could have correlated effects on the measurement and that magnitude of stated systematic uncertainty may be incompatible with measurement result. Furthermore, in this naive approach, the statistical procedure is not considered in the evaluation of uncertainties and it is therefore not based on a rigorous manner. Since the statistical inference of the measurement presented in this thesis is based on a likelihood method, the systematic uncertainties should be incorporated into the likelihood function used to perform the fit.

A "typical" systematic uncertainty consists of a set of parameters, of which the true is not known, a response function that describes the effect of these parameters on the measurement and a distribution of possible values of the parameters. This modelling definition can be concretised by help of an example [86]. Assuming a counting experiment which can be modelled with Poisson distribution as:

$$P(n|s+b) = \frac{(s+b)^n}{n!} e^{-(s+b)} \tag{6.7}$$

where n is the number of observed event count in the experiment and s is the expected number of signal events. The number of background events is denoted by b and, say, it is estimated using some MC simulation and has a negligible statistical uncertainty. But in this case, the number of background events is sensitive to detector simulation since it is estimated using MC simulation [1]. A systematic uncertainty related to some calibration originating from detector simulation can be modelled as follows:

- Say, the effect of the calibration uncertainty is described by a single parameter and this parameter effects energy calibration of some physical objects, e.g. jets, by the same amount.
- The uncertainty assigned on this parameter is a 5% Gaussian uncertainty
- Finally, it is determined that a 1% shift of this calibration effects the acceptance of background by 2%.

This systematic uncertainty with the modelling above can be incorporated in the likelihood

[1] It is also sensitive to theoretical cross section uncertainties but they are simply ignored here to have an unelaborated example.

as a Gaussian product as follows:

$$L(n|s,\alpha) = P(n|s + b(1 + 0.1\alpha)) \cdot G(0|\alpha, 1). \tag{6.8}$$

The parameters n, s and b are defined above. The function that b is multiplied with is the aforementioned *response function*. Here, the response function is normalised for the calibration uncertainty example which indicates that a unit change in α (i.e. a 5% change in the calibration) results in a 10% change on the background acceptance. The Gaussian term in the likelihood is a subsidiary measurement, or conventionally referred to as *constraint term* by physicists, that constrains the parameter α. In this particular example, the subsidiary measurement is the assumed calibration. The value of 1 denotes the unit width of the Gaussian uncertainty on the nominal calibration. The constraint term is a simplified likelihood and represents the calibration measurement of the parameter α. This calibration measurement is based on a data sample. For simplification, the data sample is replaced by a *placeholder* which is 0. The placeholder observable in the constraint term is conventionally referred to as *global observable*. In the example given above, the form of the response function is referred to as *normal response*.

The final form of the likelihood function used in the analysis is a product of equation 6.3 and the Gaussian term of the equation 6.8:

$$L = \prod_{i,j} P(N_{i,j}|N^s_{i,j} + \sum_b N^b_{i,j}) \times \prod_t G(0|\alpha_t, 1). \tag{6.9}$$

where the index t for teh parameter α represents the different systematic uncertainty sources.

6.3.2 Profile likelihood ratio

The confidence interval for the parameter of interest is estimated by a profile likelihood ratio, λ_s, which is defined as follows:

$$\lambda_s(\sigma_{\text{sl}}^{\text{tot/fid}}|p_T^{\text{iso}}) = \frac{\mathcal{L}(\sigma_{\text{sl}}^{\text{tot/fid}}, \hat{\hat{\theta}}, \hat{\hat{N}}_{\text{h-fake}}|p_T^{\text{iso}})}{\mathcal{L}(\hat{\sigma}_{\text{sl}}^{\text{tot/fid}}, \hat{\theta}, \hat{N}_{\text{h-fake}}|p_T^{\text{iso}})}. \tag{6.10}$$

In this ratio, the quantities in the nominator are the unconditional maximum likelihood estimation of the parameters where the quantities in the denominator are the conditional maximum likelihood estimation of the parameters when $\sigma_{\text{sl}}^{\text{tot/fid}}$ is fixed to a certain value. The profile likelihood ratio is evaluated within the RooFit/RooStats framework and then used to determine the upper and lower limit of the cross section within a 68% confidence level.

6.4 Cross section definitions

In order to compare the experimentally measured value of $\sigma_{t\bar{t}\gamma}$with the theoretical prediction, these two values should be equivalent in terms of the phase space in which they are measured and calculated, respectively. This is only possible by defining a certain phase space beforehand where the experimental measurement and theoretical calculation will be performed. This certain phase space is individual for each analysis and mostly defined by experimentalists who perform the measurement. This is because of the constraints originating from the experimental setup and/or features of the signal that is desired to

be measured. But there might be inputs to the definition of this phase space from theory side. Theoretical cross section calculation of a process like $pp \to t\bar{t}\gamma \to b\bar{l}\nu\bar{b}q\bar{q}^{'}\gamma$ is subject to collinear and infrared divergences and some kinematical and geometrical limits, or cuts as it is in HEP community referred to as, are needed to be considered in the calculation to avoid these divergences. In HEP community, these phase spaces are conventionally referred to as *fiducial volume* or *region* and the result as *fiducial cross section*. The presented measurement in this thesis is also performed in a fiducial phase space. The definition of the fiducial phase space is given in section 6.6.

This thesis presents also the first differential measurement of $\sigma_{t\bar{t}\gamma}$ as introduced in chapter 1. The differential measurement is performed as functions of photon transverse momentum and pseudorapidity in five bins for each of these kinematic variables. The choice of the binning for the differential measurement is motivated in section 6.9. The differential measurements are performed in the same fiducial phase space as the total measurement. Section 6.8 is dedicated to details of the differential measurement.

Throughout the thesis, the inclusive fiducial measurement is referred as *inclusive measurement* and correspondingly the result as *inclusive cross section*. The differential cross section, however, is simply referred to as differential measurement.

6.5 Definition of the inclusive cross section

At a collider experiment, the number of scattered events per unit time is defined by formula 3.1:

$$\frac{dN_{\text{event}}}{dt} = \mathcal{L}_{inst} \cdot \sigma_{\text{event}} \tag{6.11}$$

where σ_{event} is the scattering cross section and $\mathcal{L}$ is the machine instantaneous luminosity of the two beams. Integrated over a time interval for a specific process, say $t\bar{t}\gamma$, the formula yields the cross section for the $t\bar{t}\gamma$ process:

$$\sigma_{t\bar{t}\gamma} = \frac{N_{t\bar{t}\gamma}}{\mathcal{L}_{int}} \tag{6.12}$$

where $N_{t\bar{t}\gamma}$ is the number of $t\bar{t}\gamma$ signal events and $\mathcal{L}_{int}$ is the integrated luminosity. This is a very generic cross section formula for any given process. Here, $N_{t\bar{t}\gamma}$ is the number of all $t\bar{t}\gamma$ events including all decay channels. Since the scope this thesis is the cross section measurement in the single lepton channel, $N_{t\bar{t}\gamma}$ is to be replaced the number of $t\bar{t}\gamma$ events in the single lepton channel (electron or muon). In order to rewrite the formula for the single lepton channel, one also needs to consider the branching ratio term for this channel. The formula 6.12 can be rewritten with some additional terms as follows:

$$\sigma^{tot}_{t\bar{t}\gamma,\text{sl}} = \sigma^{tot}_{t\bar{t}\gamma} \times BR_{t\bar{t}\gamma,\text{sl}} = \frac{N_{t\bar{t}\gamma,sl}}{A \cdot C \cdot \mathcal{L}} \tag{6.13}$$

where $\sigma^{tot}_{t\bar{t}\gamma,\text{sl}}$ is the total cross section for the semileptonic channel per lepton flavour, $\sigma_{t\bar{t}\gamma}$ is the total $t\bar{t}\gamma$ cross section, $BR_{t\bar{t}\gamma,\text{sl}}$ is the branching ratio of the semileptonic channel channel per lepton flavour, $N_{t\bar{t}\gamma,sl}$ is the expected number of $t\bar{t}\gamma$ events in the semileptonic channel per lepton flavour. The additional terms A, the acceptance factor, and C, the correction factor, contain the correction for the event reconstruction and selection efficiencies as well as event migration from non-fiducial phase space to the fiducial phase space. Details of these two factors is discussed in section 6.7. In equation 6.13, an extrapolation from the detector phase space to the total phase space takes place which can be subject to large theoretical uncertainties since a specific region of the total phase space is extrap-

olated to a kinematic region where no measurement is performed. In order to avoid this extrapolation, equation 6.13 can be reformulated as follows:

$$\sigma^{fid}_{t\bar{t}\gamma,\mathrm{sl}} = A \times (\sigma^{tot}_{t\bar{t}\gamma} \times BR_{t\bar{t}\gamma,\mathrm{sl}}) = \frac{N_{obs} - N_{bkg}}{C \cdot \mathcal{L}}. \tag{6.14}$$

where the expected number of $t\bar{t}\gamma$ events is replaced by the difference of the expected number of the backgrounds, N_{bkg}, and the total number of observed data events passing the event selection. In this equation, the first equality in the formula represent the definition of the fiducial cross section whereas the second equality shows how the measurement is performed avoiding the aforementioned phase space extrapolation.

6.6 Definition of the fiducial phase space

There are two levels of the fiducial phase space definition: Particle, or object, selection level and event selection level.

Particle definition for fiducial region

- **Leptons:**
  Electrons and muons with $p_T > 10$ GeV and $|\eta| < 2.7$ are dressed with photons that are not originating from hadrons and are within a cone of $\Delta R = 0.1$ around the lepton. Leptons are required to have $p_T > 25$ GeV, $|\eta| < 2.5$ and to not have a hadron origin.

- **Jets:**
  Jets are clustered with the anti-k_T algorithm with a radius of $R = 0.4$ and muons are not considered in the clustering. Jets are required to have $p_T > 25$ GeV and $|\eta| < 2.5$.

- **b-jets:**
  The flavour of the jet is determined by the flavour of the hadron that satisfies a minimum p_T of 5 GeV and maximum ΔR of 0.3 with respect to the jet axis. If there are simultaneously a b-hadron and a c-hadron matching to the jet, the b-hadron is preferred.

- **Photons:**
  Photons are required not to originate from hadron decay and to have $E_T > 15$ GeV and $|\eta| < 2.37$.

- **Overlap removal:**
  The overlap removal is done between: (i) electron-jet: the jet with $\Delta R(e, j) \leq 0.2$ is removed; then the electron with $\Delta R(e, j) \leq 0.4$ is removed; (ii) photon-jet: the jet with $\Delta R(j, \gamma) \leq 0.1$ is removed; (iii) jet-muon: the muon with $\Delta R(\mu, j) \leq 0.4$ is removed.

Event selection for fiducial region

- **Leptons:**
  Exactly one electron (muon) is required in the electron (muon) channel.

- **Jets:**
  At least four jets have to be selected among which at least one should be a b-jet.

- **Photons:**
  Exactly one photon is required. Additionally, the event is rejected if the photon has a $\Delta R(j,\gamma) < 0.5$ with a jet or a $\Delta R(l,\gamma) < 0.7$ with the lepton.

In order to have a common phase space for electron and muon channels, some of the reconstruction levels cuts that are specific to either the electron or muon channel, such as $\not{E}_T$, $m_T(W)$ and $m(e,\gamma)$, are not included in the fiducial phase space definition.

6.7 Definition of the signal acceptance and correction

The aforementioned signal acceptance factor is evaluated by applying the fiducial phase space cuts to the MadGraph sample and by using the following formula:

$$A = \frac{N_{\text{gen}}^{\text{fid}}}{N_{\text{gen}}^{\text{all}}} \tag{6.15}$$

where $N_{\text{gen}}^{\text{all}}$ is the total number of events generated in the electron or muon channel and $N_{\text{gen}}^{\text{fid}}$ is the number of events that are generated within the fiducial region. The evaluated acceptance factors for the electron and muon channel are 13.9% and 13.2% respectively.

The role of the signal correction factor, C, is rather complicated. It takes two corrections into account. The first is that the events generated in the fiducial phase space but not reconstructed and selected due to the event reconstruction and selection efficiencies. The second is that the events generated outside the fiducial phase space but migrate into the fiducial phase space after reconstruction. Moreover, events from other channels, such as the τ channel, can also migrate to the fiducial phase space after reconstruction. These two cases have to be taken into account at the step of the extraction of the number of true signal events from the observed candidate events. The signal correction factor is defined as follows:

$$C = \frac{N_{\text{reco}}}{N_{\text{gen}}^{\text{fid}}} \tag{6.16}$$

where N_{reco} is the number of events passing the reconstruction level cuts and $N_{\text{gen}}^{\text{fid}}$ is the number of events generated in the fiducial region. This definition is actually product of two components:

$$C = \frac{N_{\text{reco}}^{\text{fid}}}{N_{\text{gen}}^{\text{fid}}} \cdot \frac{1}{\frac{N_{\text{reco}}^{\text{fid}}}{N_{\text{reco}}}} \tag{6.17}$$

The first component describes the reconstruction and selection efficiency for the generated signal events while the denominator in the second component is the ratio of the fiducial phase space signal events to the reconstructed and selected events. The calculated correction factor is 0.281 and 0.480 for the electron and muon channels respectively.

6.8 Definition of the differential cross section

As mentioned in chapter 1, possible deviations in the production or dynamics of a top-quark pair in association with a photon could imply new physics phenomena which could be explained e.g. through anomalous dipole moments.

One of the possible ways to enquire into these possible deviations is to investigate the kinematics of the "physical objects of interest" which is in this case the photon object.

This investigation can be carried out by performing the cross section measurement differentially as a function of the photon kinematics, such as transverse momentum and

pseudorapidity. Motivated by this argument, the differential measurement of $\sigma_{t\bar{t}\gamma}$ is performed as a function of transverse momentum and pseudorapidity in five bins for each physical observable. The choice of the bins in which the differential measurements are performed is motivated in section 6.9. The total and fiducial cross sections in each p_T or η bin can be defined in a similar way as the inclusive definition is defined:

$$\sigma^{\text{tot}}_{\text{sl},i} = \sigma^{\text{tot}}_i \times B_{\text{sl}} = \frac{N_i - N_{b,i}}{A_i \cdot C_i \cdot L}, \tag{6.18}$$

$$\sigma^{\text{fid}}_{\text{sl},i} = A_i \times (\sigma^{\text{tot}}_i \times B_{\text{sl}}) = \frac{N_i - N_{b,i}}{C_i \cdot L}, \tag{6.19}$$

where i is the p_T or η binning index. The acceptance and correction factors in each bin are also calculated in a similar way:

$$A_i = \frac{N^{\text{fid}}_{\text{gen},i}}{N^{\text{all}}_{\text{gen},i}}, \tag{6.20}$$

$$C_i = \frac{N_{\text{reco},i}}{N^{\text{fid}}_{\text{gen},i}}. \tag{6.21}$$

The values are summarised in Table 6.1 for the p_T and in Table 6.2 for the η differential measurement.

Table 6.1.: Acceptances and correction factors in each photon p_T bins for the electron and muon channels and their combination [87]. Statistical uncertainties are negligible, while systematic uncertainties are discussed in section 8.2.

p_T Bin (GeV)		$15 \le p_T < 25$	$25 \le p_T < 40$	$40 \le p_T < 60$	$60 \le p_T < 100$	$100 \le p_T < 300$
A (%)	e + jets	18.2	19.4	20.6	24.5	34.1
	μ + jets	17.4	18.6	19.7	22.8	32.3
	e/μ + jets	17.7	18.9	20.1	23.5	33.1
C (%)	e + jets	22.4	27.6	31.0	33.9	38.1
	μ + jets	38.1	48.2	54.8	57.3	62.0
	e/μ + jets	30.2	37.8	42.7	45.4	49.9

Table 6.2.: Acceptances and correction factors in each photon η bins for the electron and muon channels and their combination [87].. Statistical uncertainties are negligible, while systematic uncertainties are discussed in section 8.2.

η Bin		$0 \le \lvert\eta\rvert < 0.25$	$0.25 \le \lvert\eta\rvert < 0.55$	$0.55 \le \lvert\eta\rvert < 0.90$	$0.90 \le \lvert\eta\rvert < 1.37$	$1.37 \le \lvert\eta\rvert < 2.37$
A (%)	e + jets	20.8	20.9	20.5	20.2	19.7
	μ + jets	19.9	19.9	19.5	19.3	18.9
	e/μ + jets	20.2	20.4	19.9	19.7	19.3
C (%)	e + jets	31.5	31.3	29.4	27.5	21.4
	μ + jets	51.8	53.1	50.4	48.0	37.7
	e/μ + jets	41.6	42.0	39.7	37.6	29.4

In principle, the acceptance for the inclusive measurement and and the differential bins are expected to be similar. However, it can be seen that the acceptance for the

inclusive measurement is smaller. The reason to this originates from the gap between generation level and reconstruction level cuts, 10 GeV and 15 GeV respectively, for the photon p_T. There is no such a gap for the differential bins.

6.9 Optimisation of differential binning

A significant differential cross-section measurement requires a rigorous binning of the physical observable, as a function of which the cross-section measurement will be performed. If the measurement does not suffer from lack of data statistics, finer binning is advantageous for new possible observation. However larger number of bins causes more migration between the bins. As a consequence, if the data to be analysed is not rich in terms of statistics, then the analyser should optimise the binning considering the statistics of each bin and the migration between the bins.

For the optimisation of the bins, the resolution of the photon p_T and η are studied. The difference between the p_T or η of the generated and the reconstructed photon in the event can be interpreted as resolution and obviously the smaller the difference the better the resolution. The migration between the bins becomes smaller with the smaller resolution and correspondingly the binning could also go finer as long as the statistics of the bins allows. The resolution for the photon p_T and η are checked in the signal region. On top of the signal selection a truth matching is performed between the generated and reconstructed photon by requiring a maximum distance limit of $\Delta R < 0.1$. The p_t and η resolutions as a function of generated photon p_T and η for both channels are shown in figure 6.1. The resolution is observed to be better in the low p_T region than in the high p_T region,

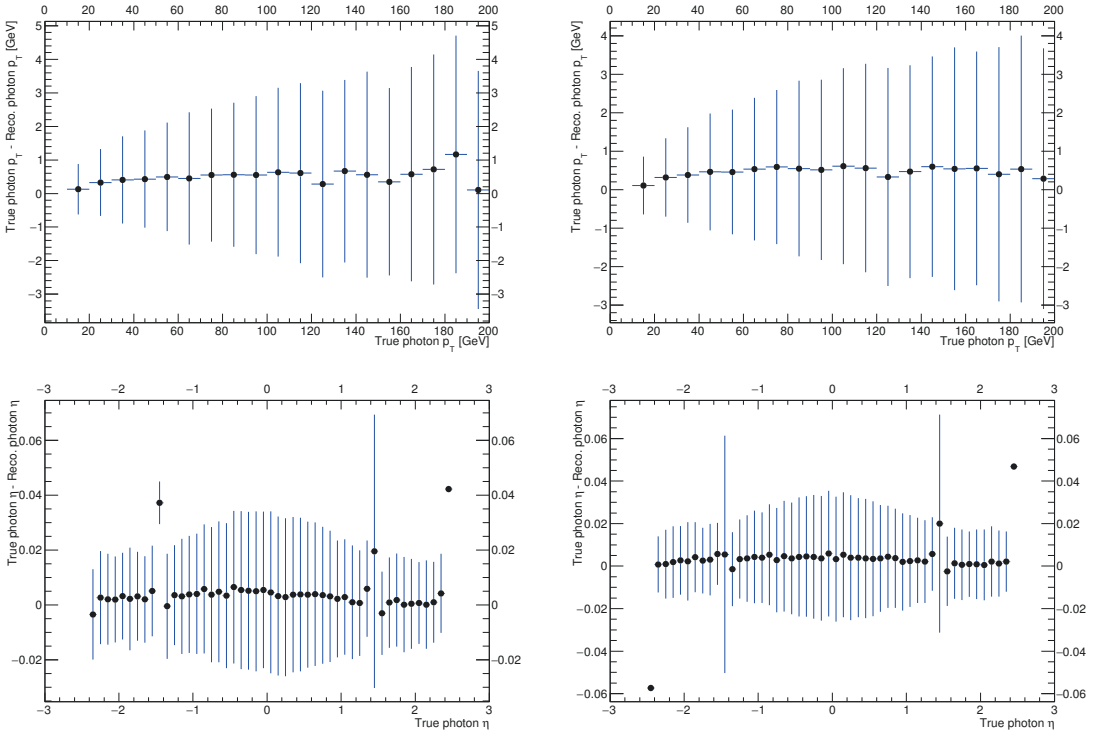

Figure 6.1.: Resolutions of photon p_T and η for the electron (left column) and muon (right column) channels in the signal region.

while the η resolution is relatively better in the forward regions of the detector than in the

central region. Considering the resolutions of the physical observables, different binning combinations are studied. The statistics seem to have the most homogeneous distributions with p_T binning of {15,25), {25,40), {40,60), {60,100), {100,300} GeV and η binning of {0.0,0.25) {0.25,0.55), {0.55,0.90), {0.90,1.37} {1.52,2.37}. For these bins, the expected number of events are calculated by normalising the MC prediction to the data luminosity. The expected number of events are shown in two dimensional histograms in figure 6.2 as a function of generated and reconstructed photon p_T and η separately. Furthermore, to

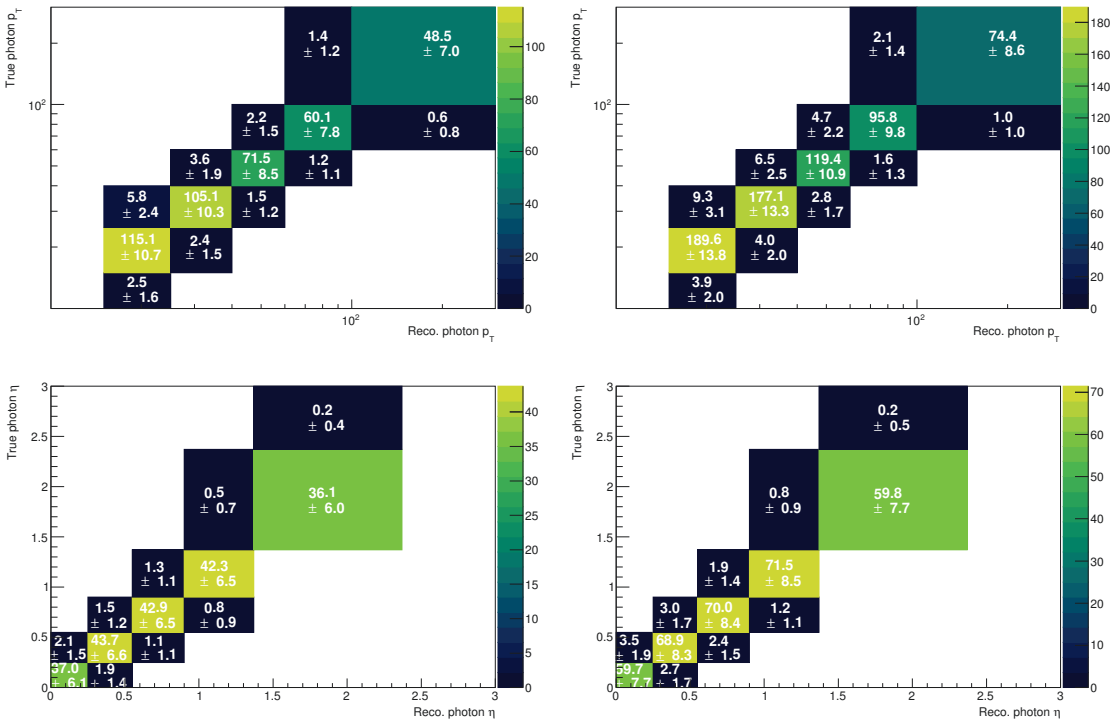

Figure 6.2.: Expected number of events for the differential photon p_T and η bins for the electron (left column) and muon (right column) channels in the signal region.

study the migration between bins, the statistical population of each bin is converted into percentages with respect to the generated photon p_T or η (y-axes). Figure 6.3 shows the fraction of events in percentages. This justifies the chosen method of bin-by-bin unfolding for the calculation of the differential cross-section. It can be seen that the population in the diagonal elements for both photons observables p_T and η in both channels are always above 93% which is promising for a significant differential measurement.

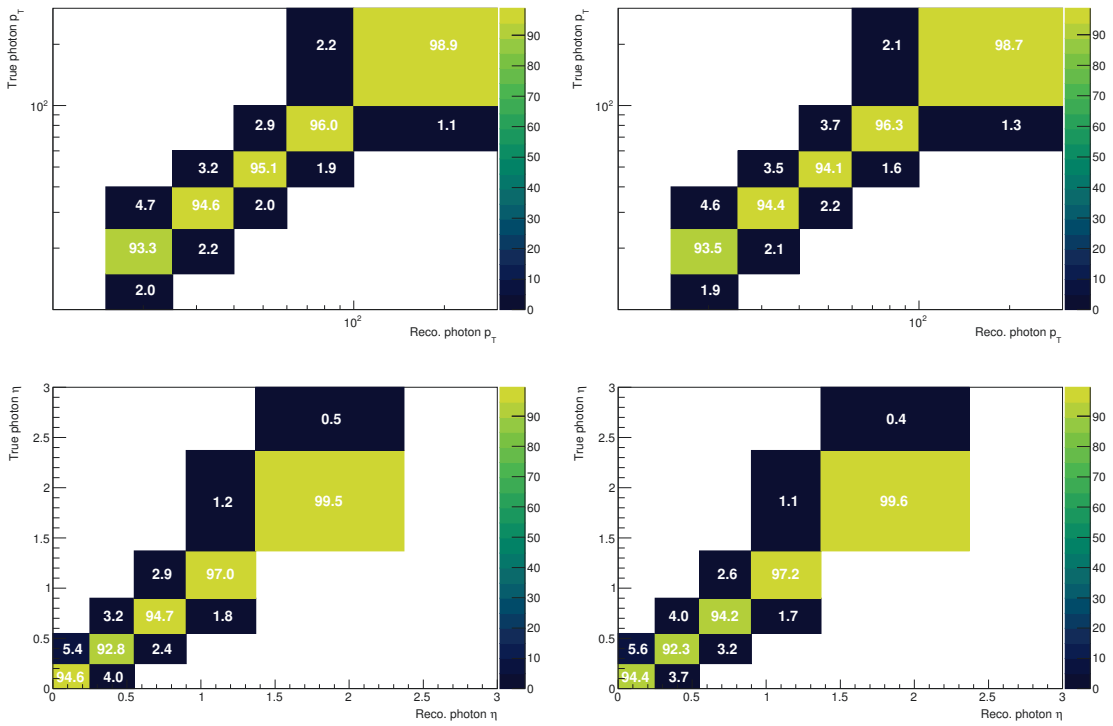

Figure 6.3.: Fraction of events in percentages for the differential photon p_T and η bins for the electron (left column) and muon (right column) channels in the signal region.

Chapter 7

Extraction of templates and estimation of backgrounds

7.1 Prompt photon template

In the fit framework, signal-like photons are represented by a template determined from $t\bar{t}\gamma$ Monte Carlo simulation, although the intention is to perform the measurement as much independent of MC simulations as possible. However, it is not possible to determine a statistically sufficient and highly pure sample of signal-like photons from $t\bar{t}\gamma$ or even any other processes using data. A possible solution to make use of data for this purpose would be to use $Z \to ee$ processes, as has been preferred in the previous measurements[1]. Electrons and photons have a very similar signature in the EMCal and this feature can be exploited. The obstacle with this solution, however, is the difference between the event topologies of $Z \to ee$ and $t\bar{t}\gamma$ processes. The photons in the $t\bar{t}\gamma$ event topology are expected to be less isolated due to the higher jet multiplicity and this would require a reweighing which brings additional systematics along. As a result, in order to avoid all these, the template for signal-like photons is determined using $t\bar{t}\gamma$ MC in the presented analysis.

For the determination of the template, the isolation distribution of photons from $t\bar{t}\gamma$ MC is investigated. After selecting signal events by applying the nominal $t\bar{t}\gamma$ event selection, the reconstructed photon in each event is geometrically (i.e. ΔR distance) matched to the truth photon. The aim of this *truth matching* is to select only prompt photons in the event by excluding photons originating from QED showering. The preference of the ΔR value, for this purpose is motivated by investigating the ΔR distribution between the reconstructed and the truth photon coming from the matrix element. As can be seen in figure 7.1, and as expected, in 95% of selected events, the ΔR distance between the reconstructed and the truth photon is smaller than 0.1. Motivated by this, the ΔR value of 0.1 is preferred to perform the truth matching.

Fig. 7.2 shows the isolation variable p_T^{cone20} of signal photons in the electron and muon channels after the truth matching. The statistical uncertainty of the template is rather small, as expected, due to the large statistics of the signal MC. The statistical uncertainties are shown in table 7.1 both for fiducial region and for each differential p_T and η bin. The large uncertainties in the last two bins have very rudimentary effect on the cross-section measurement since they are low populated for signal events.

[1] Another reason to prefer using $Z \to ee$ processes was the limited statistics of $t\bar{t}\gamma$ MC simulation at the time.

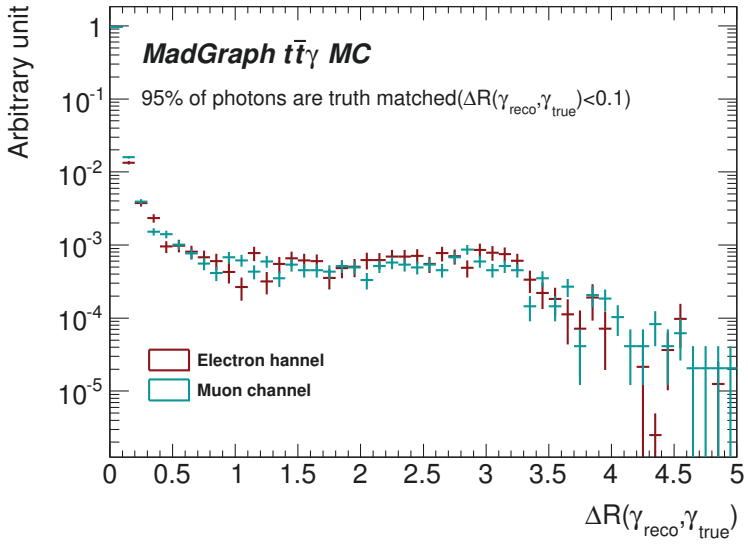

Figure 7.1.: Distribution of ΔR between the reconstructed and the matrix element photon after the nominal event selection.

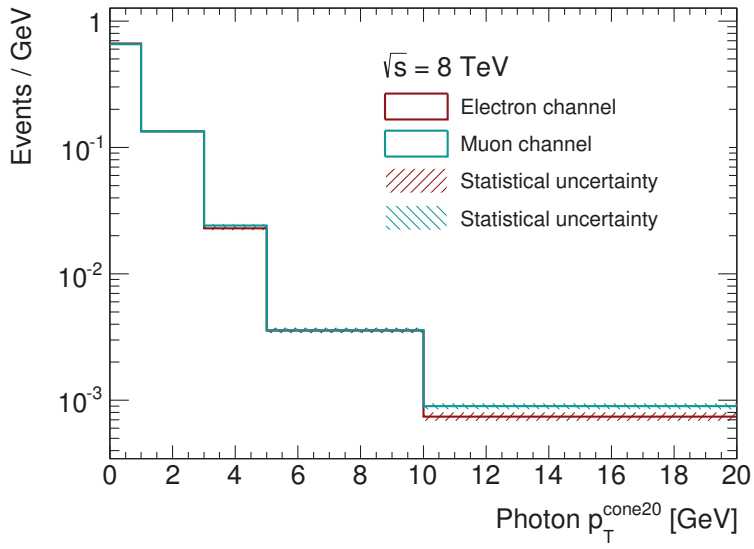

Figure 7.2.: Prompt photon templates for the electron and muon channels extracted from the $t\bar{t}\gamma$ MC sample.

Table 7.1.: Statistical uncertainty of the prompt photon template in the electron and muon channels for the fiducial measurement and p_T and η differential measurements.

p_T^{iso} Bin (GeV)		$0 \leq p_T^{iso} < 1$	$1 \leq p_T^{iso} < 3$	$3 \leq p_T^{iso} < 5$	$5 \leq p_T^{iso} < 10$	$10 \leq p_T^{iso}$
e + jets (%)	fiducial	0.4	1.0	2.8	4.5	6.9
	$15 \leq p_T < 25$ GeV	0.8	1.9	5.7	10.1	23.7
	$25 \leq p_T < 40$ GeV	0.9	2.0	5.5	9.2	14.6
	$40 \leq p_T < 60$ GeV	1.1	2.4	6.4	10.3	13.8
	$60 \leq p_T < 100$ GeV	1.3	2.6	6.7	9.5	13.6
	$100 \leq p_T < 300$ GeV	1.3	3.1	8.4	12.5	15.7
	$0 \leq \lvert\eta\rvert < 0.25$	1.0	2.3	6.4	9.6	16.2
	$0.25 \leq \lvert\eta\rvert < 0.55$	1.0	2.1	5.9	9.3	14.0
	$0.55 \leq \lvert\eta\rvert < 0.90$	1.0	2.2	6.1	9.3	14.9
	$0.90 \leq \lvert\eta\rvert < 1.37$	1.0	2.2	6.1	10.5	14.2
	$1.37 \leq \lvert\eta\rvert < 2.37$	1.0	2.7	7.6	13.0	18.8
μ + jets (%)	fiducial	0.4	0.8	2.2	3.7	5.2
	$15 \leq p_T < 25$ GeV	0.6	1.5	4.4	8.1	14.3
	$25 \leq p_T < 40$ GeV	0.7	1.6	4.1	7.3	11.8
	$40 \leq p_T < 60$ GeV	0.9	1.9	5.1	8.1	10.1
	$60 \leq p_T < 100$ GeV	1.0	2.2	5.6	8.2	10.7
	$100 \leq p_T < 300$ GeV	1.1	2.5	6.9	10.0	12.3
	$0 \leq \lvert\eta\rvert < 0.25$	0.9	1.9	4.9	8.4	11.7
	$0.25 \leq \lvert\eta\rvert < 0.55$	0.8	1.7	4.5	7.5	10.6
	$0.55 \leq \lvert\eta\rvert < 0.90$	0.8	1.8	4.6	7.9	10.1
	$0.90 \leq \lvert\eta\rvert < 1.37$	0.8	1.8	5.0	7.8	11.5
	$1.37 \leq \lvert\eta\rvert < 2.37$	0.8	2.1	6.4	9.9	16.0

7.2 Template for photons faked by hadrons

The template for photons faked by hadrons, from here on referred to as *hadronic-fake template*, represents the background events in which a hadron is misidentified as a photon or where a hadron decays into multiple photons. These objects will be referred to as *hadronic-fakes* and the background events with these misidentified objects as *hadronic-fake background*. The hadronic-fake background consists mostly of $t\bar{t}$ events with a photon from the hadronisation process and not from the hard scattering. This background dominates all other background contributions in the analysis.

The template is extracted from a control region selected from the `JetTauEtmiss` stream in data. An optimised selection is applied in order to enrich the control region with hadronic-fakes.

7.2.1 Control region definition

At the ATLAS experiment, photons are identified according to the shower-shape variables (F_{side}, w_{s3}, ΔE, E_{ratio}) which hold information from the strip (first) layer of the ECAL. The shower shape variables are the essential component of the tight photon identification. Therefore, a control region to be enriched with hadronic-fakes can be selected by loosening the cuts on the shower shape variables. The control region is selected by applying the following cuts:

- Existence of a good vertex in the event.
- At least one photon that fails at least one of the shower shape cuts defined in the tight photon identification.
- At least four jests in the event in order to have a similar event topology to the signal event. (Figure 7.3 supports the choice on the number of jets.)
- Rejection of hadronic-fake candidates with a close by electron, i.e. $\Delta R(\gamma_{had-fake}, e) < 0.1$. This hadronic-fake control region must be free of backgrounds with photons faked by electron since that background contribution is treated separately.

In order to take any kinematic dependence of the photon in the control region into account, the track isolation distribution of the hadronic-fakes in the control region is plotted as a function of p_T and η intervals. These distributions are shown in figure 7.4. Obvious p_T and η dependences can be observed in these distributions. In the first distribution where the p_T dependence is checked, it can be observed that the isolation distributions for p_T intervals differ from each other. The higher the hadronic-fake p_T is, the lower the isolation. This is accountable since a hadronic-fake with a high transverse momentum is expected to be radiated collinear to the jet in which the hadronic-fake is produced. Being radiated collinear to a jet means being surrounded by jet activities which, in turn, means less isolation. The case is different for η intervals. The isolation distributions for η are, so to speak, clustered in two regions, below $\eta = 1.81$ and beyond $\eta = 1.81$, where the former region is less and the latter is more isolated. The η dependence, unlike the p_T dependence, has a hardware related explanation. It is to observe these hadronic-fakes in high η regions are more isolated which means that the jet activity surrounding that hadronic-fakes in this region is lower. This can be explained by the fact that the track reconstruction efficiency at ATLAS is η dependent. As can be seen in figure 7.5, the track reconstruction efficiency is under 80% for the region $|\eta| > 1.80$. In order to take these dependences into account,

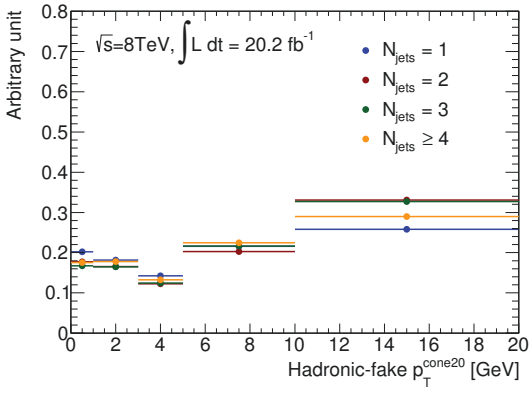

Figure 7.3.: The p_T^{cone20} distributions of the hadronic-fakes in the data control region a function of jet multiplicity. The distributions are normalised to unity and the last bin contains the overflow. The statistical uncertainties are too small to be visible in the plot. The isolation distribution has a high dependence on the number of jets. $N_{\text{jets}} > 3$ is the nominal selection to be used in the fit.

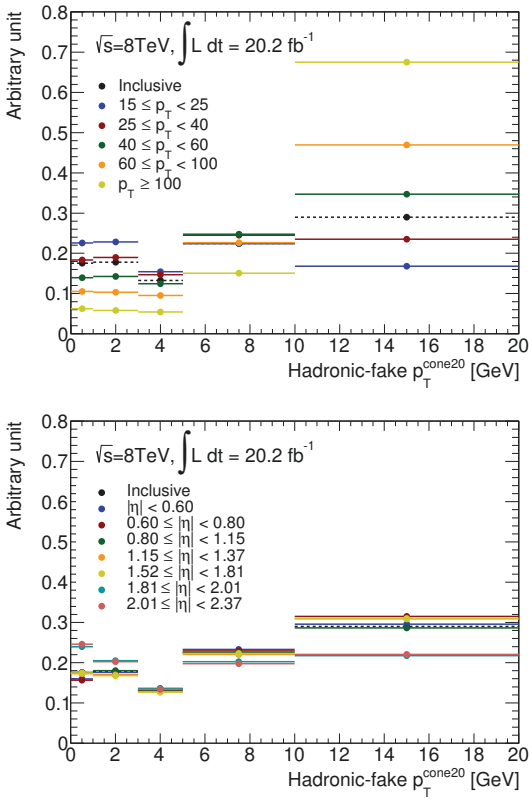

Figure 7.4.: The p_T^{cone20} distributions of the hadronic-fakes in the data control region as a function of photon p_T (upper) and η (lower) differential bins, as well as the inclusive distribution (dashed line). The distributions are normalised to unity and the last bins contains the overflow. The statistical uncertainties are too small to be visible in the plot. A high p_T and η dependence is to be observed.

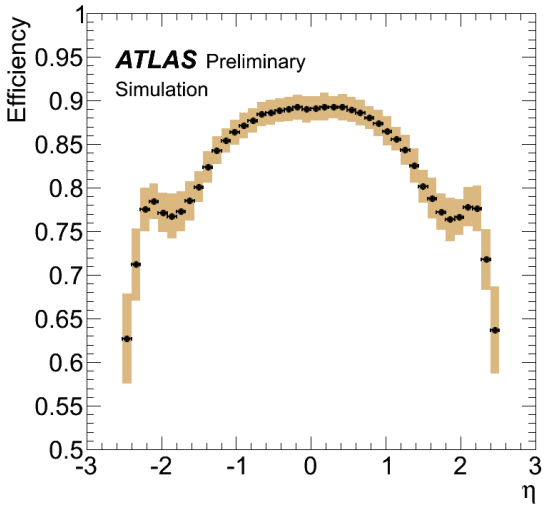

Figure 7.5.: Track reconstruction efficiency as a function of η obtained using the GEO-20 detector model, for tracks with p_T >500 MeV. The systematic uncertainties were determined by comparison to a model with +10% additional material in the whole ID [88].

the inclusive hadronic-fake template has to be weighted using the p_T and η distributions of the hadronic-fakes in the signal event topology. For extracting these p_T and η distributions in the signal event topology, another control region ($t\bar{t}\gamma_{h-fake}$ CR) is selected from data. The selection of the $t\bar{t}\gamma_{h-fake}$ CR is performed by modifying the nominal signal selection by replacing the tight photon requirement with the requirement of hadronic-fake. All other cuts in the selection remain the same. The p_T and η distributions of the hadronic-fakes from the control region $t\bar{t}\gamma_{h-fake}$ are shown figure 7.6. Although this modified control region seems to be a convenient option to extract the template directly, it cannot be used because of the very limited statistics after the selection of this CR. Before performing

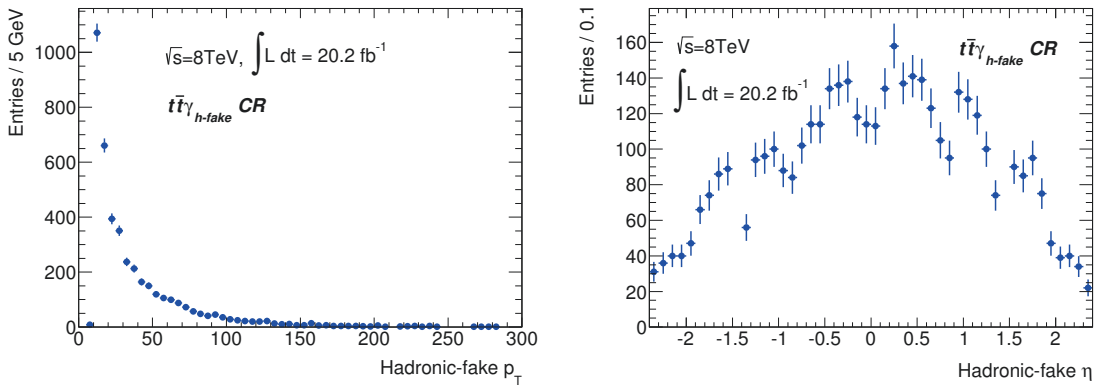

Figure 7.6.: p_T (left) and η (right) distributions of the hadronic-fakes from the $t\bar{t}\gamma_{h-fake}$ CR defined by modifying the signal selection.

the weighting, any possible correlation between kinematics of the hadronic-fakes in the $t\bar{t}\gamma_{hadfake}$ CR should be checked. This correlation check is shown in figure 7.7 where p_T

and η variables of the hadronic fakes are shown in a two dimensional scatter plot. No correlation between the p_T and η is observed. Since there is no correlation observed, the p_T and η dependences can be weighted separately. The weighting of the hadron-fake

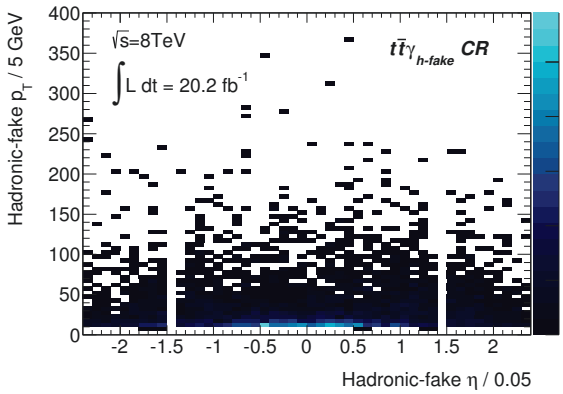

Figure 7.7.: Scatter plot for transverse momentum and pseudo-rapidity of hadronic-fake objects in the $t\bar{t}\gamma_{h-fake}$ control region. No correlation is observed. The weighting of the hadronic fakes template can be performed separately.

template can be formulated as follows:

$$T^{\text{h-fake}}_{\text{weighted}} = \frac{1}{2}\left(\sum_{i=1}^{5} w_{p_T,i} \;\; T_i^{\text{h-fake}}(p_T) + \sum_{j=1}^{2} w_{\eta,j} \;\; T_j^{\text{h-fake}}(\eta)\right) \tag{7.1}$$

where $T_i^{\text{hadfake}}(p_T)$ is the hadronic-fake template of the p_T bin i and $w_{p_T,i}$ is its corresponding weight. Similarly, $T_j^{\text{hadfake}}(\eta)$ is the hadronic-fake template of the η bin j with its associated weight $w_{\eta,j}$.

Because of the reasons discussed earlier in this section, the p_T weighting of the template is performed for all p_T intervals, i.e. $15 \leq p_T < 25$, $25 \leq p_T < 40$, $40 \leq p_T < 60$, $60 \leq p_T < 100$ and $p_T \geq 100$ GeV, whereas the η weighting is performed for only two intervals, i.e. $|\eta| \leq 1.81$ and $1.81 < |\eta| \leq 2.37$. The hadronic-fake template of $p_T(\eta)$ bin $i(j)$ is weighted by the fraction of the $t\bar{t}\gamma_{hadron-fake}$ data events in the bin $i(j)$:

$$w_{p_T,i} = \frac{N_i}{\sum\limits_i N_i} \quad \text{and} \quad w_{\eta,j} = \frac{N_j}{\sum\limits_j N_j}. \tag{7.2}$$

The $w_{p_T,i}$ and $w_{\eta,j}$ are summarised in table 7.2 and table 7.3, and the final weighted hadron-fake template is shown in figure 7.8. The uncertainty of the weighted template comes from the uncertainties of the weights, which are due to the statistical fluctuation of $t\bar{t}\gamma_{hadron-fake}$ CR.

Table 7.2.: $p_T$weights used for the reweighing of the hadron-fake template of the fiducial measurement.

p_T bins [GeV]	$15 \leq p_T < 25$	$25 \leq p_T < 40$	$40 \leq p_T < 60$	$60 \leq p_T < 100$	$p_T \geq 100$
w_{p_T}	0.42 ± 0.01	0.28 ± 0.01	0.14 ± 0.01	0.10 ± 0.01	0.06 ± 0.01

Table 7.3.: η weights used for the reweighing of the hadron-fake template of the fiducial measurement.

η bins	$\lvert\eta\rvert \leq 1.80$	$1.80 < \lvert\eta\rvert \leq 2.37$
w_η	0.88 ± 0.01	0.12 ± 0.01

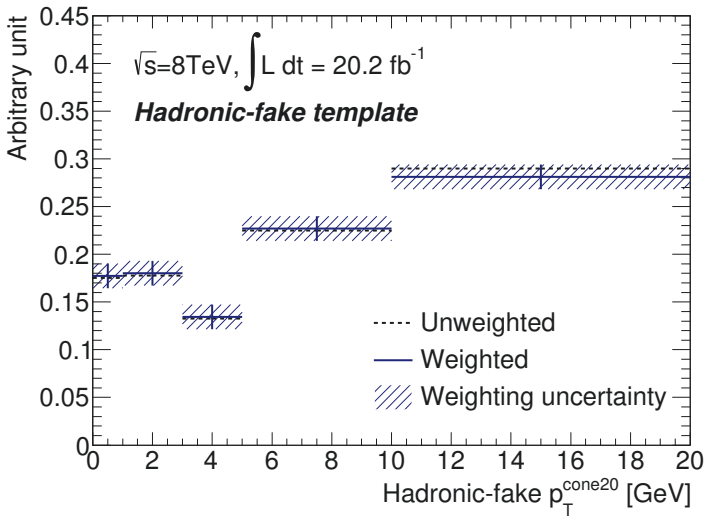

Figure 7.8.: The data-driven hadron-fake template, before and after being weighting according to p_T and η. The distributions are normalised to unity and the last bin contains the overflow. The uncertainty of the weighted template is due to the $w_{p_T,i}$ and $w_{\eta,j}$ uncertainties.

7.2.1.1 Prompt photon contamination in the hadron-fake template

Although the selection based on failing of one of the tight photon ID requirements on the shower shape variables enriches the hadronic photon fake control region, prompt photons can still leak into this control region and bias the measurement. This section presents the investigation and treatment of this contamination.

One option to treat this contamination is to correct the template extracted from data using MC. However this option is ruled out since MC simulations, which are produced and conventionally used by ATLAS analyses, do not present a good description of data in terms of jet kinematics. In figure 7.9, the multiplicity and kinematics of the jets in the hadronic fake control region are presented for data and di-jet MC sample produced centrally for ATLAS analyses. It can be seen that the jet multiplicity and transverse

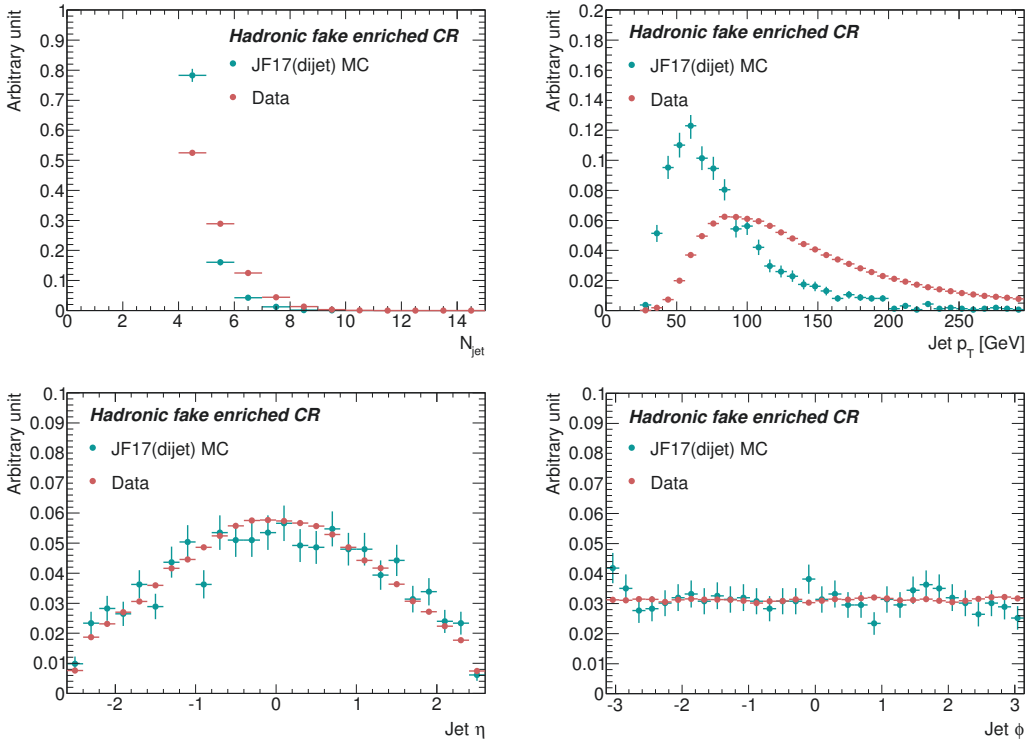

Figure 7.9.: Comparison of data and JF17 di-jet MC sample in terms of jet kinematics. It can be seen that the MC does not describe the data well. The sample is therefore not suitable to be used for evaluating the systematic uncertainty for prompt photon contamination.

momentum distributions differ dramatically between the MC and data. Another option is to assign a systematic uncertainty dedicated to this contamination. In order to determine this systematic uncertainty, the effect of failing multiple requirements of the shower shape variables is studied. As it can be recalled, the nominal hadronic fake sample was extracted by selecting hadronic fake candidates which fails at least one of the shower shape requirements in the tight photon ID. The nominal sample could be extracted by selecting hadronic fakes that fail all four shower shape requirements since it is expected that the more the shower shape requirements fail, the smaller the probability that the selected hadronic fake candidate to be a prompt photon. But this reduces the statistics dramatically which becomes an obstacle especially in the differential measurement. This expectation is checked

by using data. Figure 7.10 presents four different isolation distributions. The distributions are extracted by requiring exactly one, two, three and four shower shape requirements to fail. It can be seen that with the increasing number of failing requirements the distributions become less and less isolated which satisfies the expectation. This expectation

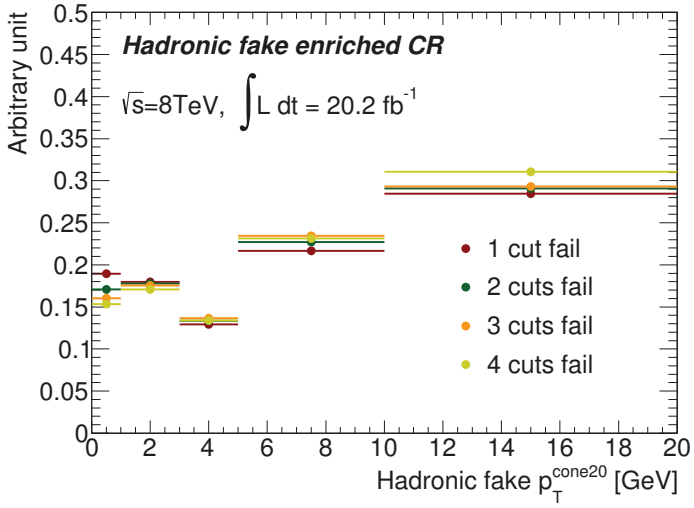

Figure 7.10.: Hadronic fake isolation distributions extracted from MC for four cases where exactly one, two, three and four shower shape variables are required to fail. It can be seen that higher the number of failed cuts, the less isolated the hadronic photon fakes are.

is also cross checked with a MC study. In figure 7.11, isolation distributions extracted from MC are presented again for four cases where exactly one, two, three and four shower shape variables are required to fail. The advantage of the MC simulation is the event record information. By exploiting this information, isolation distributions of hadronic fake candidates are extracted where the candidate itself or its mother particle is a true hadronic particle. The comparison of these truth matched and not matched distributions can be seen in the same figure. The result clearly shows that the more the failing cuts, the higher the probability of being a true hadronic fake. Motivated by this fact, the shape difference between the nominal template and the template extracted by selecting hadronic fakes failing all four shower shape cuts of the tight photon ID is assigned as a systematic uncertainty for the prompt photon contamination. The shape difference for the inclusive template is presented in figure 7.12. The systematic uncertainty is determined before the p_T and η weighting of the template due to the statistical issue in the $t\bar{t}\gamma_{hadron-fake}$ control region.

7.2.1.2 Templates for the differential measurements

The templates for the differential p_T and η bins are extracted with the same procedure that is used in the inclusive measurement case. Furthermore, weightings of the differential templates also follow the same procedure used for the inclusive template. For the differential measures, the templates themselves do not suffer from statistics however, the control region used for weighting has low statistics in the differential bins which effects the weighting uncertainties. The effect of the low statistics on the weighting uncertainty can be especially seen in the large p_T and forward η regions. The templates are presented

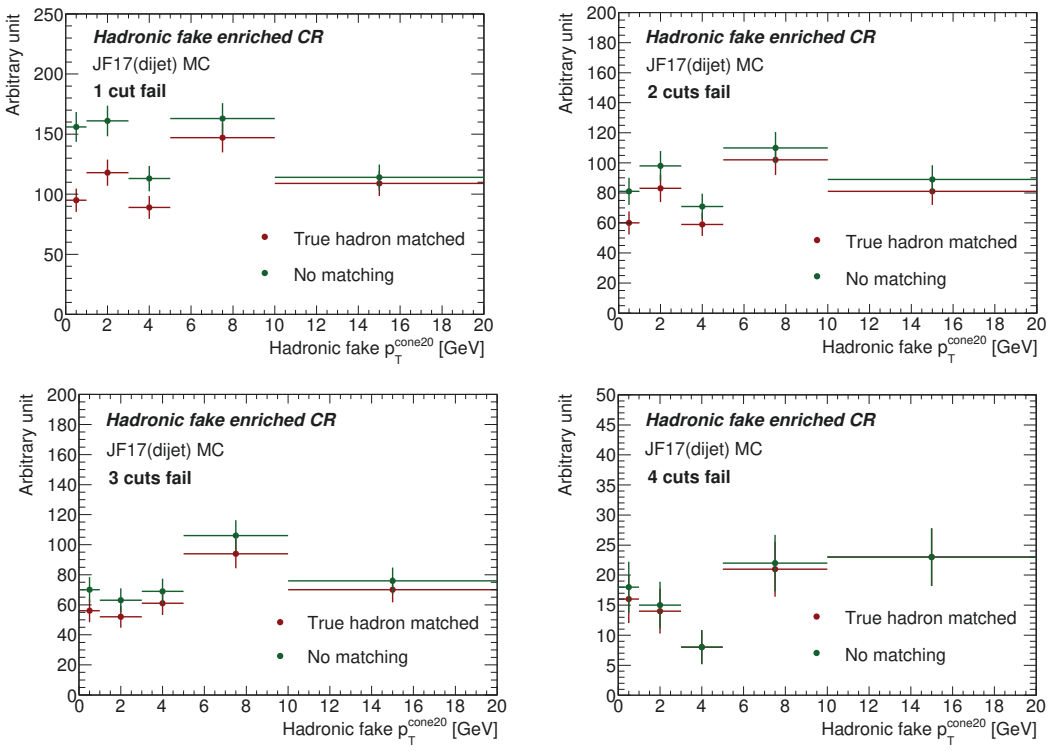

Figure 7.11.: Hadronic fake isolation distributions extracted from MC for four cases where exactly one, two, three and four shower shape variables are required to fail. Distributions are presented where the hadronic photon fakes are matched to a hadronic origin and where no matching is performed. It can be seen that higher the number of failed cuts, the more likely the hadronic photon fakes have a hadronic origin.

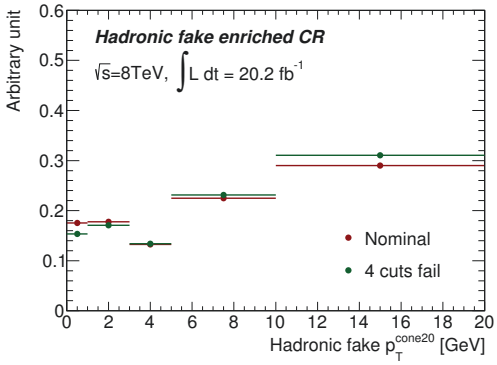

Figure 7.12.: Comparison of the nominal template and the template with all shower shape variables are required to failed. The difference is assigned as a systematic error.

in figure 7.13 and figure 7.14.

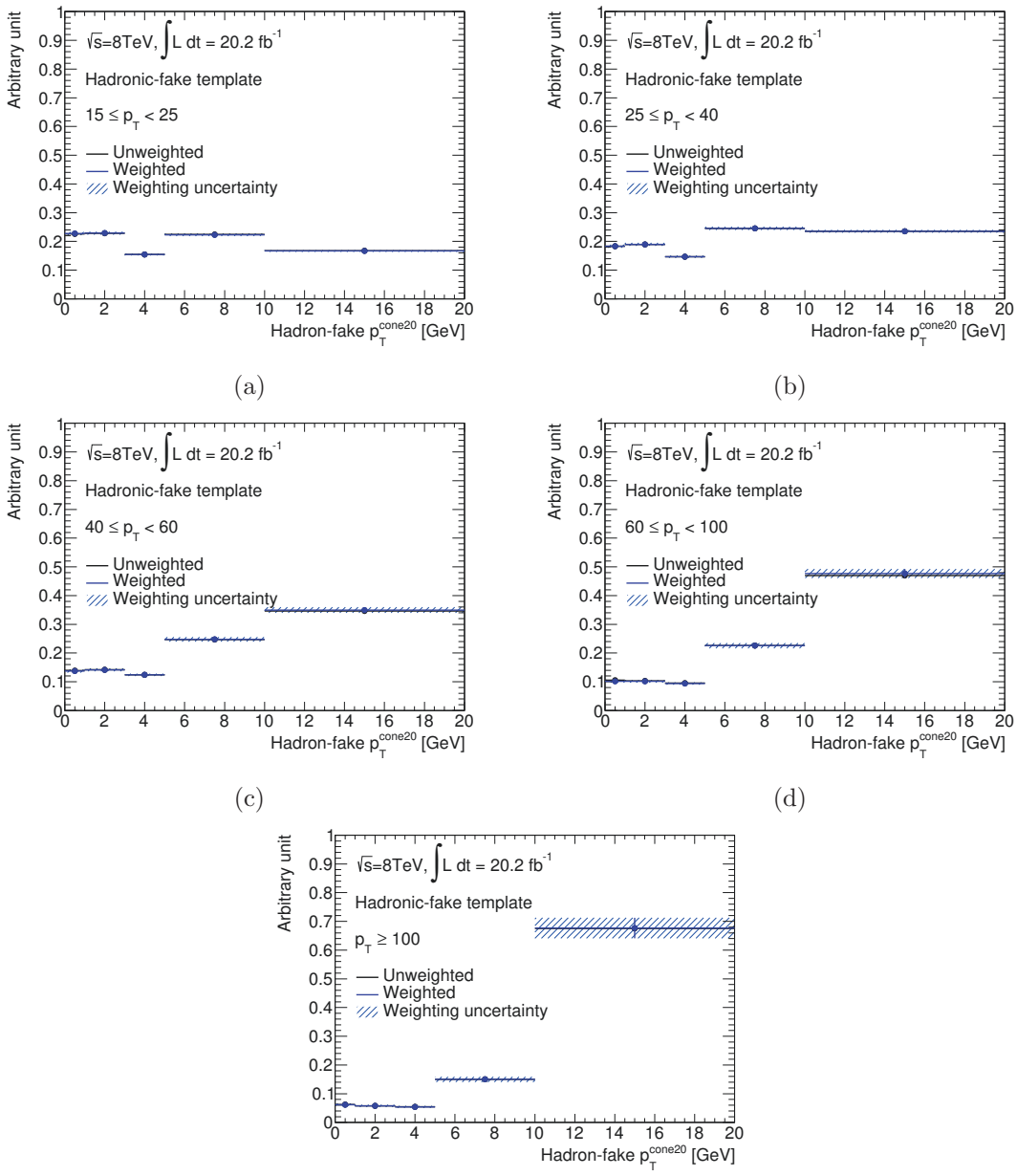

Figure 7.13.: Templates for photons faked by hadrons for the differential measurement in p_T bins: $15 \leq p_T < 25$ GeV, (b) $25 \leq p_T < 40$ GeV, (c) $40 \leq p_T < 60$ GeV, (d) $60 \leq p_T < 100$ GeV and (e) $100 \leq p_T < 300$ GeV. Templates are presented before and after being weighted using two η bins: $|\eta|$¡1.81 and $|\eta| \geq$1.81. The distributions are normalised to unity and the last bins contains the overflows. The uncertainties of the weighted templates are due to the weighting uncertainties.

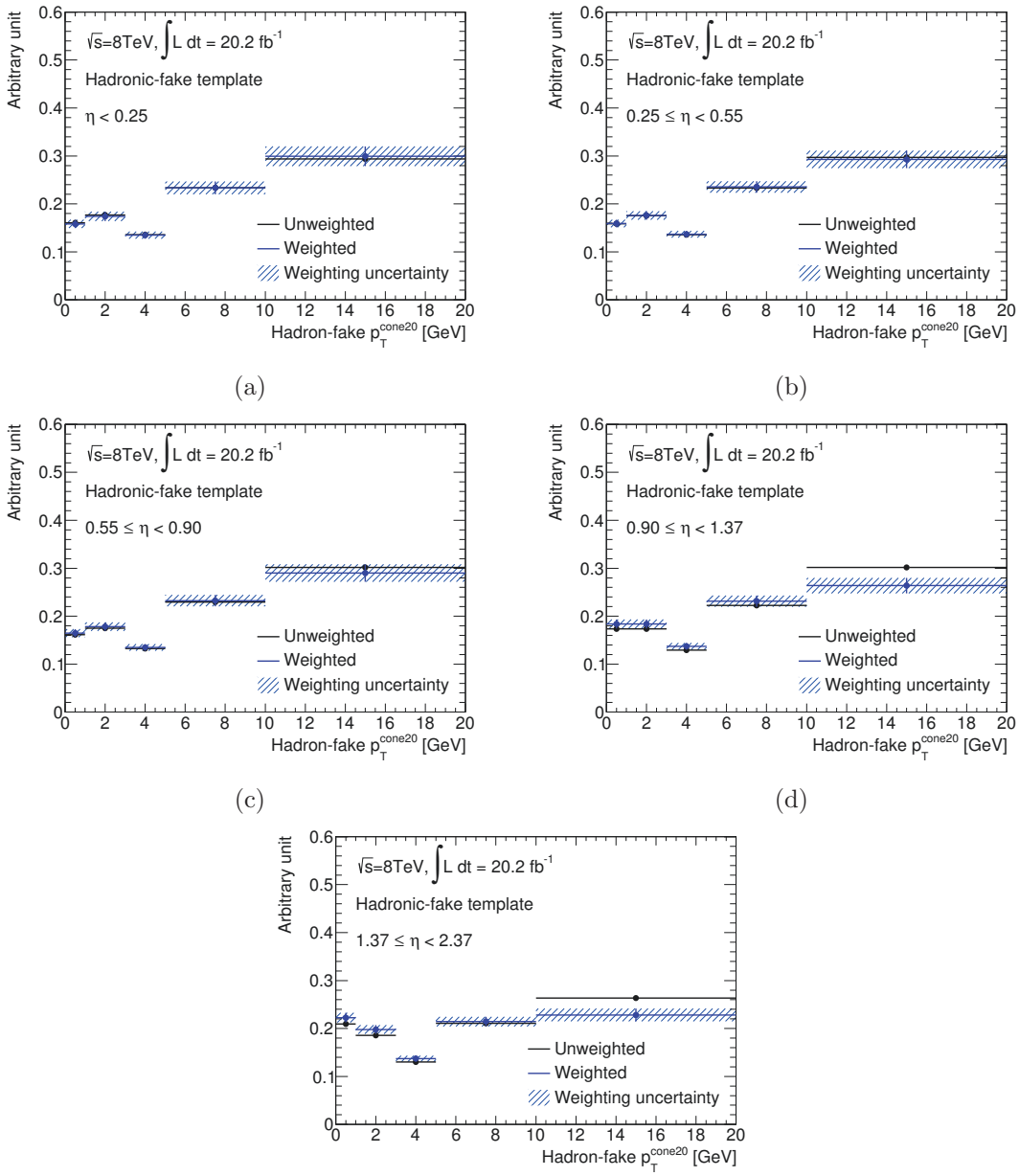

Figure 7.14.: Templates for photons faked by hadrons for the differential measurement in η bins: (a) $|\eta| \leq 0.25$, (b) $0.25 < |\eta| \leq 0.55$, (c) $0.55 < |\eta| \leq 0.90$, (d) $0.90 < |\eta| \leq 1.37$ and (e) $1.37 < |\eta| \leq 2.37$. Templates are presented before and after being weighted using five p_T bins: $15 \leq p_T < 25$, $25 \leq p_T < 40$, $40 \leq p_T < 60$, $60 \leq p_T < 100$ and $p_T \geq 100$. The distributions are normalised to unity and the last bins contains the overflows. The uncertainties of the weighted templates are due to the weighting uncertainties.

cross-section The resemblance between electrons and photons compels the reconstruction of these objects to share the same algorithm to a good deal of extent, as discussed in chapter 4. This leads to misidentification of electrons as photons. In certain final states, such as dileptonic $t\bar{t}$ decays (ee and $e\mu$ channels only) and Z+jets events where the Z-boson decays into an e^+e^- pair, the misidentification of electrons leads to a background process to the signal of the presented analysis. In addition, physical processes such as bremsstrahlung and photon conversion are also obstacles to differentiation between electrons and photons. Events with electrons misidentified as photons is the largest background contribution coming after hadron-fake background (cf. section 7.2). An electron can easily be misidentified as a photon under the following conditions:

- Despite electrons differ from photons by their associated tracks, an electron with a poorly reconstructed track can be misidentified as an unconverted photon.
- Moreover, an electron with any close by jet activity, which can be reconstructed as tracks pointing to the EMC clusters of electrons, can be misidentified as a converted photon.

7.2.2 Estimate of the number events with $e \to \gamma$ fakes

The contribution of this background is estimated by investigating $Z \to e^+e^-$ decays in data. These events with e^+e^- pairs having an invariant mass around the Z-boson mass window are overwhelmingly dominated by true electrons. However, electrons can radiate high-E_T photons. Since these high-E_T photons are radiated collinear with respect to their mother electrons, the detector might detect only the high-E_T photons and in turn misidentify these electrons as photons. These events are referred to as $Z \to e\gamma$ events. This misidentification can be exploited to estimate the fraction of electrons faking photons ($e \to \gamma$ *fake rate*, or $fr_{e\to\gamma}$) and ultimately the contribution of background events with electrons misidentified as photons. The fake rate is estimated using $Z \to ee$ and $Z \to e\gamma$ events and in a second step, this fake rate is applied onto a *modified signal region*, denoted as (SR$'$), to estimate the final contribution. The signal region is modified by replacing the requirement of a photon with an electron which is required to fulfil the kinematic requirements of the signal photon. This electron is referred to as *photon-like electron* in the following.

In order to estimate the $fr_{e\to\gamma}$, two distinct event selections are applied to select $Z \to ee$ and $Z \to e\gamma$ control regions. The event selections and object definitions used in these selections are described in section 7.2.3. In both selections, the leading electron in the event, the *tag electron*, is used for the single lepton trigger matching while the subleading e/γ object, the *probe object*, is used to calculate the invariant mass together with the tag electron.

The calculation of the $fr_{e\to\gamma}$ is performed in 5×5 $E_T \times \eta$ bins and formulated as follows: If the total number of true dielectron $Z \to ee$ events is $N^{CR}_{e_ie_j}$ with one electron being in (p_T, η) bin i where the other in bin j, the number of events in the $Z \to ee$ and $Z \to e\gamma$ control regions, $N^{CR}_{e_i^T e_j^L}$ and $N^{CR}_{e_i^T \gamma_j^L}$ respectively, can be factorised as:

$$N^{CR}_{e_i^T e_j^L} = N^{CR}_{e_ie_j} \cdot \epsilon_i^{reco} \cdot \epsilon_i^{id} \cdot \epsilon_i^{iso} \cdot \epsilon_j^{reco} \cdot \epsilon_j^{id} \tag{7.3}$$

$$N^{CR}_{e_i^T \gamma_j^L} = N^{CR}_{e_ie_j} \cdot \epsilon_i^{reco} \cdot \epsilon_i^{id} \cdot \epsilon_i^{iso} \cdot \mathcal{P}(e \to \gamma)_j \cdot \epsilon(\gamma)_j^{id}. \tag{7.4}$$

Here, different efficiencies are denoted by ϵ(*reconstruction, identification, isolation*) for

electrons and photons which are provided by centrally by ATLAS. $\mathcal{P}(e \to \gamma)$ denotes the probability of an electron being reconstructed as a photon. The electron super indices, T and L, indicate *tight* and *loose*, respectively. The tight electron is the standard electron from the $t\bar{t}\gamma$ signal region, where the loose electron is an electron without isolation. In order to avoid any bias, no isolation criterion is required for the probe objects. The fake rate then can be expressed as follows by dividing the two formulae above:

$$fr_{e\to\gamma,j} = \frac{N^{CR}_{e^T\gamma^L_j}}{N^{CR}_{e^Te^L_j}} = \frac{\mathcal{P}(e \to \gamma)_j \cdot \epsilon(\gamma)^{id}_j}{\epsilon^{reco}_j \cdot \epsilon^{id}_j} \tag{7.5}$$

after summing up over the bin i.

The number of events with $e \to \gamma$ fakes in the signal region can be described exploiting the same interpretation as follows:

$$N^{SR'}_{e^T_ie^L_j} = N^{SR'}_{e_ie_j} \cdot \epsilon^{reco}_i \cdot \epsilon^{id}_i \cdot \epsilon^{iso}_i \cdot \epsilon^{reco}_j \cdot \epsilon^{id}_j \tag{7.6}$$

$$N^{SR'}_{e^T_i\gamma^L_j} = N^{SR'}_{e_ie_j} \cdot \epsilon^{reco}_i \cdot \epsilon^{id}_i \cdot \epsilon^{iso}_i \cdot \mathcal{P}(e \to \gamma)_j \cdot \epsilon^{\gamma,id}_j \tag{7.7}$$

where $N^{SR'}_{e_ie_j}$ is the total number of dilepton events, $N^{SR'}_{e^T_ie^L_j}$ is the observed number of dilepton events and $N^{SR'}_{e^T_i\gamma^L_j}$ is the observed number of the events with $e \to \gamma$ fakes. Dividing equation 7.7 by equation 7.6 and summing up over the index i yields:

$$N^{SR'}_{e^T_i\gamma^L_j} = N^{SR'}_{e^T_ie^L_j} \cdot fr_{e\to\gamma,j}. \tag{7.8}$$

The photon can be faked not only by the *photon-like* electron but by any of the two electrons in the modified signal region. Similarly to equation 7.7, the fake rate considering the other electron faking photon can be described as follows:

$$N^{SR'}_{\gamma^L_ie^T_j} = N^{SR'}_{e_ie_j} \cdot \mathcal{P}(e \to \gamma)_i \cdot \epsilon^{\gamma,id}_i \cdot \epsilon^{id}_j \cdot \epsilon^{reco}_j \cdot \epsilon^{iso}_j. \tag{7.9}$$

By dividing equation 7.9 by equation 7.6, one calculates the number of background events with an isolated electron misidentified as a photon:

$$N^{SR'}_{\gamma^L_ie^T_j} = N^{SR'}_{e^T_ie^L_j} \cdot fr_{e\to\gamma,i} \cdot \frac{\epsilon^{iso}_j}{\epsilon^{iso}_i}. \tag{7.10}$$

The final contribution is then the sum of two cases; $N^{SR'}_{\gamma^L_ie^T_j}$ and $N^{SR'}_{e^T_i\gamma^L_j}$. The last term in equation 7.10 is estimated by performing a fit as for the estimation of the fake rate ($fr_{e\to\gamma}$). For this, the ratio of $N^{CR}_{e^T_ie^T_j}$ to $N^{CR}_{e^T_ie^L_j}$ events are calculated by fitting the Z-boson masses.

7.2.3 Object definition and event selection for the data driven fake rate estimation

Electron candidates satisfying the `Tight++` criteria, including the conversion veto `isEM` bit, are used. They are required to have a $p_T > 15$ GeV and $|\eta_{cl}| < 2.47$, excluding the crack-region $1.37 < |\eta_{cl}| < 1.52$. Electron candidates are to fulfil the `egamma` OQ quality flags. The electron p_T cut is motivated by the p_T threshold of the nominal signal photons. Photon candidates (for the $Z \to e\gamma$ CR) are selected using the same definition as in section 4.4.

As usual, objects that overlap are removed. In the $Z \to ee$ and $Z \to e\gamma$ control regions, muon candidates within $\Delta R = 0.4$ with respect to calibrated jets (LCW+JES) are rejected. In addition, the closest jet to a good electron candidate is rejected if $\Delta R(e, j) < 0.2$. Finally, any jet within a cone $\Delta R = 0.1$ with respect to the reconstructed photon is also discarded.

The *tag* electron in the event is required to be identified as tight++ with a $p_T > 25$ GeV and to pass the single electron trigger. Calorimetric (`Etcone20@90`) and track (`ptcone30@90`) isolation cuts are applied (same case as for the definition of the signal electron in the $t\bar{t}\gamma$ selection). For the $Z \to ee$ sample, exactly two back-to-back ($\Delta\varphi_{e^+e^-} > 150°$) electrons with opposite charge are required in the event. To avoid trigger bias and for consistency with how the $Z \to ee$ sample is treated (cf. section 7.2.2), for the $Z \to e\gamma$ sample the *tag* electron p_T is required to be larger than that of the leading photon (this requirement is omitted for one of the cross checks and the results are found to be in good agreement.). The electron and the photon are also required to be back-to-back ($\Delta\varphi_{\ell\gamma} > 150°$). In both cases, a muon veto is applied. The invariant mass corresponding to each selection ($m(ee)$ for $Z \to ee$ and $m(e\gamma)$ for $Z \to e\gamma$) is required to be in a window of ± 50 GeV around the Z-boson mass. Invariant Z-mass distributions of the selected data events are shown in figure 7.15. Figure 7.16 shows the p_T distributions for the *tag* and the *probe* objects for the $Z \to ee$ ($Z \to e\gamma$) selection performed on the full 2012 dataset.

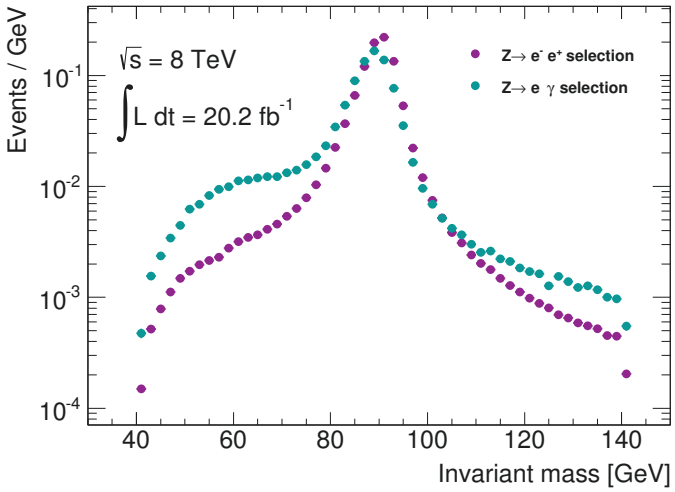

Figure 7.15.: Invariant mass distributions of the selected $Z \to ee$ and $Z \to e\gamma$ data events.

7.2.3.1 Calculation of the fake rates

The fake rates are calculated by fitting the ee and $e\gamma$ invariant mass distributions. The fit is performed in the different bins of photon p_T and η and is repeated in three invariant mass windows of [60-120] GeV, [70-110] GeV and [80-100] GeV using a crystal ball function to describe the signal and a Gaussian function for background. Figure 7.17 shows an example of a fit performed for the photon E_T [25-35] GeV bin within a mass window of [70-110] GeV. Figure 7.18 shows $fr_{e\to\gamma}$ distributions for all (both converted and unconverted) photons in data. The dependence of the fake rate from E_T, η, pile-up(μ) and number of primary vertices distributions are shown.

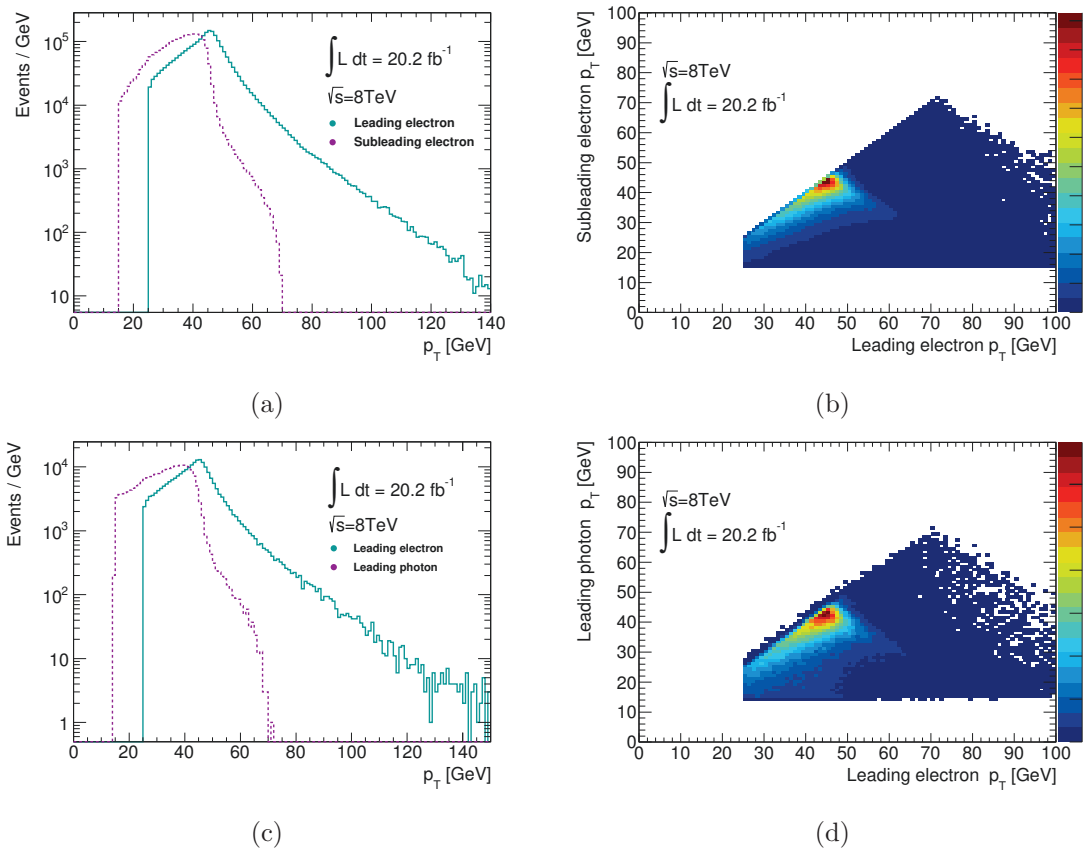

Figure 7.16.: p_T distributions of the *tag* and *probe* electron (a), and photon (c). *Probe* versus *tag* p_T for $Z \to ee$ (b), $Z \to e\gamma$ (d) event selection. The vertical (horizontal) line in the correlation plots indicates the minimum p_T-cut for the *tag* (*probe*) object. For the $Z \to e\gamma$ selection, the electron was required to have a p_T larger than that of the photon.

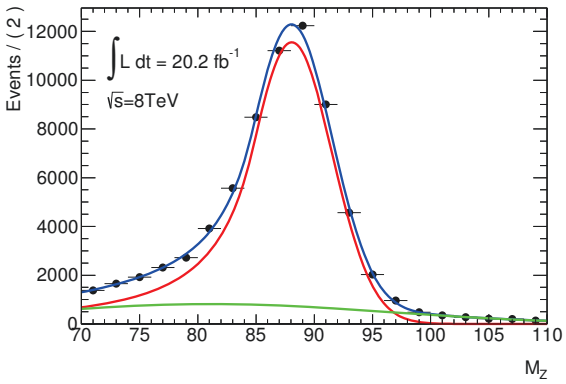

Figure 7.17.: Example fit for the calculation of $fr_{e\to\gamma}$ in the photon E_T [25-35] GeV bin in data using crystal ball + Gaussian functions. The red line describes the crystal ball function for signal and the green line describes the Gaussian background, where the blue line is the signal and the background in total.

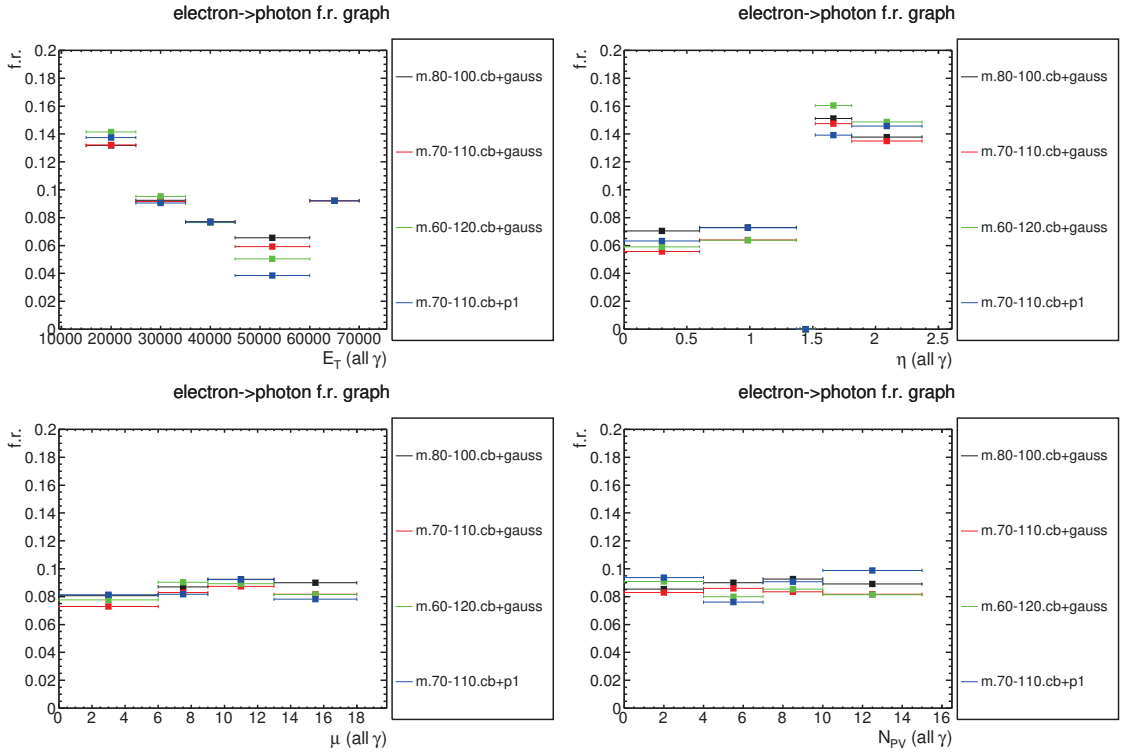

Figure 7.18.: Distributions of electron faking photon rate versus (a) photon E_T, (b) photon η, (c) μ and (d) NPV, shown for all (converted and unconverted) photons in data. Results are shown for CB+Gauss and CB + p1 (first order polynomial) fits performed in different mass windows. [60-120] GeV, [70-110] GeV and [80-100] GeV.

The resulting fake rates are shown in figure 7.19 in different E_T and η bins. In order to estimate the final background contribution of the events with an electron faking a photon in the signal region, the calculated fake rates are applied to a control region selected in data. The control region is defined by the nominal signal selection with an electron instead of a photon, where the electron is required to fulfil the photon requirements. Noting that in the electron channel we will end up with two selected electrons, both of them will contribute to the final background estimate. The $E_T \times \eta$ matrix of the *photon-like electron* in the control region described above is reweighted according to the fake rates shown in figure 7.19. The resulting background contributions of $e \to \gamma$ fake estimated in this way are $317 \pm 7 \pm 41$ and $385 \pm 6 \pm 42$ events in the electron and muon channels respectively, with the first error being statistical and second being the quadratic sum of the variations of fit function and fit ranges. Similarly, the $e \to \gamma$ fake backgrounds in each photon p_T and η bins are studied and the results are summarised in table 7.4 and 7.5.

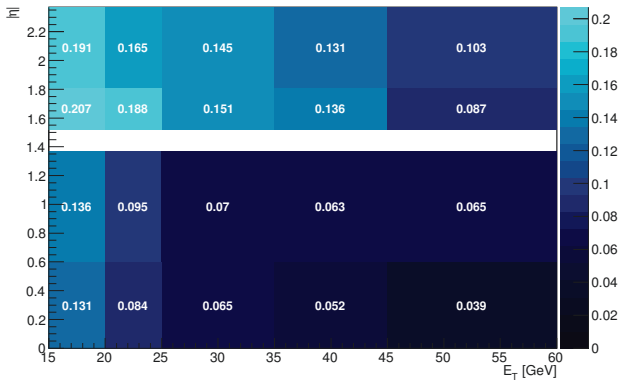

Figure 7.19.: The resulting fake rates are represented in different E_T and η bins.

Table 7.4.: The estimated $e \to \gamma$ fake background events in each photon p_T bins with their statistical (first) and systematic (second) uncertainties

p_T bin [GeV]	$15 \leq p_T < 25$	$25 \leq p_T < 40$	$40 \leq p_T < 60$	$60 \leq p_T < 100$	$100 \leq p_T < 300$
e + jets	$92.1 \pm 3.6 \pm 15.6$	$79.0 \pm 3.5 \pm 3.1$	$60.8 \pm 3.0 \pm 16.8$	$55.4 \pm 2.7 \pm 22.3$	$29.5 \pm 1.8 \pm 11.2$
μ + jets	$136.4 \pm 4.4 \pm 23.0$	$91.4 \pm 2.9 \pm 4.1$	$65.8 \pm 2.2 \pm 17.8$	$62.0 \pm 2.0 \pm 24.9$	$29.2 \pm 1.4 \pm 11.3$

Table 7.5.: The estimated $e \to \gamma$ fake background events in each photon η bins. The first uncertainty is of statistics and the second is of systematics.

η bin	$0 \leq \lvert\eta\rvert < 0.25$	$0.25 \leq \lvert\eta\rvert < 0.55$	$0.55 \leq \lvert\eta\rvert < 0.90$	$0.90 \leq \lvert\eta\rvert < 1.37$	$1.37 \leq \lvert\eta\rvert < 2.37$
e + jets	$39.0 \pm 2.2 \pm 9.2$	$50.4 \pm 2.5 \pm 11.9$	$63.4 \pm 3.2 \pm 18.4$	$71.8 \pm 3.4 \pm 21.0$	$92.6 \pm 4.9 \pm 6.8$
μ + jets	$50.2 \pm 1.9 \pm 12.8$	$61.3 \pm 2.1 \pm 15.2$	$81.9 \pm 2.7 \pm 19.8$	$85.8 \pm 2.7 \pm 22.9$	$105.8 \pm 3.9 \pm 6.3$

7.2.4 Extraction of the template

Due to the reasons mentioned in section 6.2, the isolation of $e \to \gamma$ fake candidates is expected to be different from the isolation of prompt photons. This fact is presented

graphically in figure 7.20 where the isolation of $e \to \gamma$ is compared to the isolation of prompt photons in the signal region, which is in fact the nominal signal template to be used in the maximum likelihood fit. The isolation of $e \to \gamma$ fakes is extracted from $Z \to ee$ MC simulation by applying the $Z \to e\gamma$ selection described previously in section 7.2.3. Then, the isolation of of photons in the so-called $Z \to e\gamma$ decays is compared to the signal template. It can be clearly observed that the $e \to \gamma$ fakes are remarkably less isolated than prompt photons. For this reason, a separate template dedicated to $e \to \gamma$ fakes has to be considered in the maximum likelihood fit.

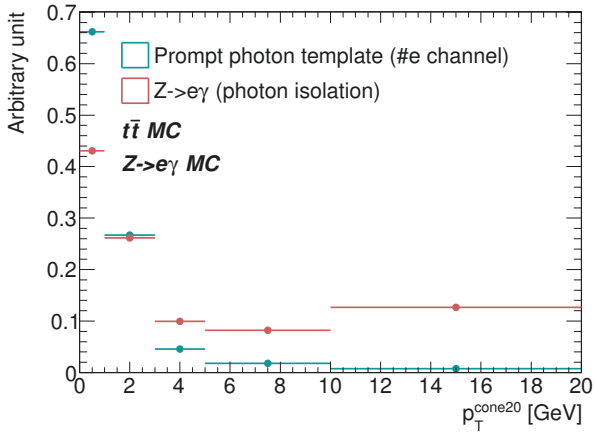

Figure 7.20.: Comparison of photon isolation distributions for prompt photons and photons faked by electrons. The distribution of prompt photons is extracted from $t\bar{t}$ MC by applying nominal signal event selection, since the dileptonic $t\bar{t}$ events are the dominating source of this background. The distribution of photons faked by electrons is extracted from $Z \to ee$ MC by applying $Z \to e\gamma$ selection.

Therefore, a template can be built from isolation of photons from the $Z \to e\gamma$ decays selected using data. However, the isolation distribution of photons from the $Z \to e\gamma$ decays cannot be directly employed in the fit because of the possible biases due to different event topologies between the $t\bar{t}\gamma$ signal region and the $Z \to e\gamma$ control region. Existence of any possible bias can be found out by investigating the effects of different cuts applied in the signal and the control region. This investigation is performed by following an add-and-remove-cuts method using MC simulations, where the cuts object to the signal and the control region, which are listed in table 7.6, are applied one by one and their effects are investigated. The investigation is performed by using $Z \to ee$ MC simulation produced

Table 7.6.: The list of cuts applied to investigate their effects on the template for photons faked by electrons.

Signal region	Control region
Overlap removals (γ,e/j)	p_T ordering (e/γ)
E_T^{Miss}	$\Delta\phi$ (ee or $e\gamma$)
m_W^T + jets	m_Z window
Jet multiplicity	-
b-tagging	-

centrally by ATLAS. The effects of all cuts individually and with some combinations are presented in figure 7.21. Most of the cuts, such as jet multiplicity, b-tagging, overlap removal cuts and most of the control region cuts do not show any strong effect on the isolation behaviour. Nevertheless, one control region cut, p_T ordering, and two signal region cuts, E_T^{Miss} and m_W^T, seem to have remarkable effects.

The p_T ordering cut requires the leading photon to have smaller transverse momentum than the leading electron in the $Z \to ee$ decay events. This cut has a relatively limited effect in comparison to E_T^{Miss} and m_W^T cuts. The effect of this cut is therefore decided to be assigned as a systematic uncertainty which is evaluated by using $Z \to ee$ MC where the shape difference between the isolation distributions with and without application of this cut is evaluated.

The m_W^T cut has an obvious effect on the isolation behaviour. The isolation becomes less and less isolated with the increasing m_W^T cut value. In order to judge this effect correctly, a reference isolation distribution is needed. This reference is extracted from $t\bar{t}$ MC by applying he nominal signal event selection since it is known that the dileptonic $t\bar{t}$ events(ee or $e\mu$ channel), in which one of the electrons is misidentified as a photon, is major source of this background contribution. In the distribution, it can be seen that as the m_W^T cut value gets closer to the nominal value applied in the signal selection, the distribution get more deflected from the $t\bar{t}$ distribution. For this reason, it is decided to not apply any m_W^T cut when extracting the template for $e \to \gamma$ fakes.

The case is different for the E_T^{Miss} cut. As the E_T^{Miss} cut value increases and gets closer to the value applied in the nominal signal selection, the distribution gets also closer to the reference distribution. It can be seen that the distributions with the E_T^{Miss} cuts of 30 GeV and 35 GeV are the two most reference like distributions. As a result, it would be the normal decision to apply the E_T^{Miss} cut of 30 GeV, which is the value of the nominal signal selection in the electron channel, as the nominal cut, and to assign the shape difference between the distributions with 30 GeV and 35 GeV E_T^{Miss} cuts as a systematic uncertainty.

In addition to these two systematic uncertainties, due to p_T ordering and E_T^{Miss}, any possible background contamination in the template is checked by varying the size of the Z-boson mass window cut applied like it is performed for the assignment of the systematic uncertainty on the $fr_{e\to\gamma}$ estimation (cf. section 7.2.2). The Z-boson mass window is varied to be 20 GeV narrower, i.e. 80-100 GeV, or broader, i.e. 60-120 GeV, than the nominal window size applied, i.e. 70-110 GeV. Both distributions seem to be almost identical to the nominal distribution. The shape difference between the distributions is assigned as a systematic uncertainty. The nominal template to be used in the fit and the variation templates used for the evaluation of the systematics are presented in figure 7.22.

The templates for the differential measurements are extracted by following the same procedure. In figure 7.16c, it can be seen that transverse momentum distribution of photons from the $Z \to e\gamma$ control region does not extend beyond 60 GeV. For this reason, differential template for the last two p_T bins, i.e. [60,100] GeV and [100,300] GeV, cannot be extracted. Therefore, for these two bins, the template for the bin of [40-60] GeV is used. However, this *bypass* sort of solution should be assigned with an uncertainty and this extrapolation uncertainty is calculated as the difference between the template from the template from the bin of [40,60] GeV and the average template of the all three bins. The templates for the differential η bins are extracted as usual. The differential templates for p_T and η bins are presented in figure7.23.

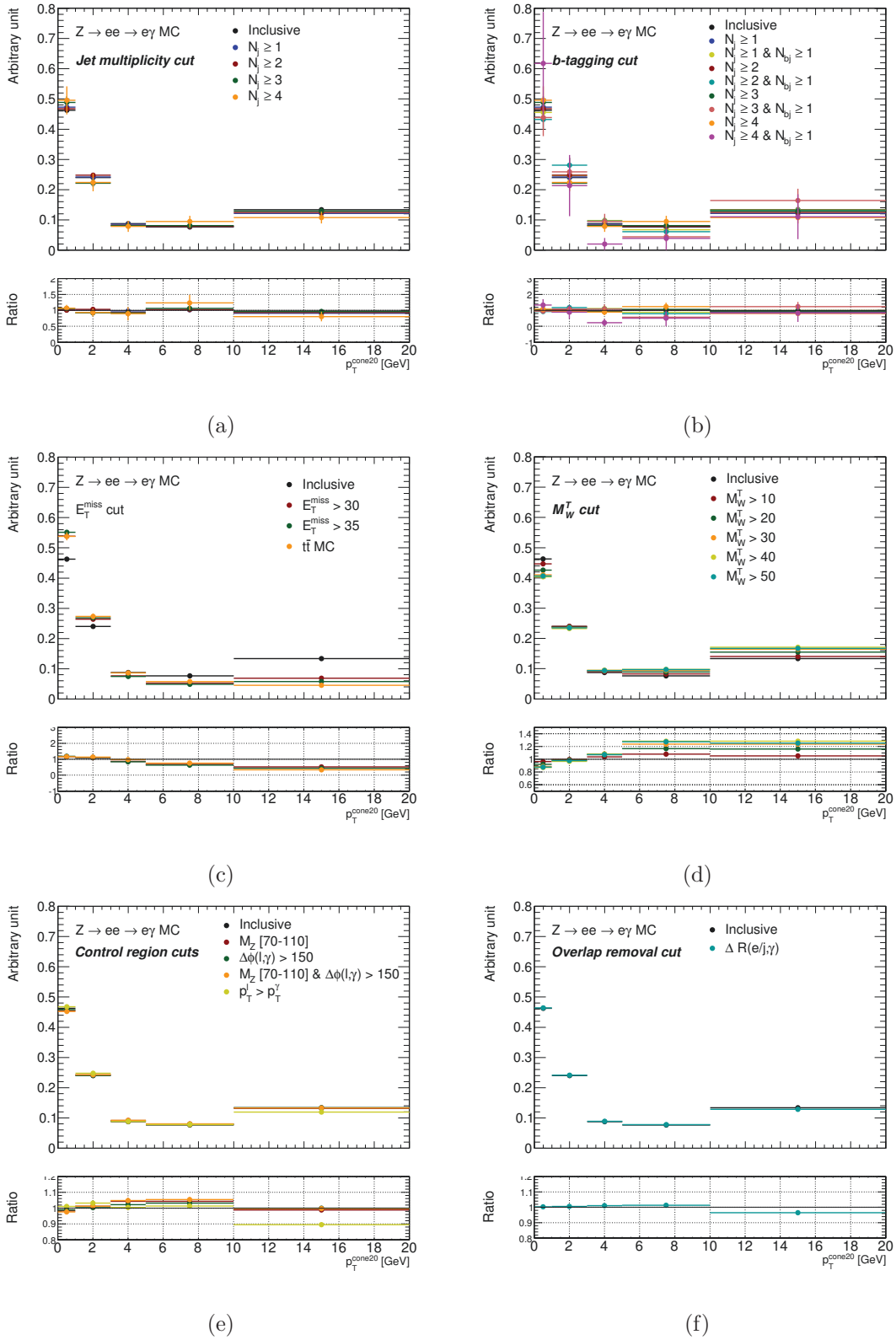

Figure 7.21.: Photon isolation distributions where the effects of several SR and CR cuts are investigated: (a) is the check for jet multiplicity, (b) for b-tagging, (c) for E_T^{miss}, (d) for M_W^T, (e) for control region cuts and (f) for the overlap removal between the photon and other objects.

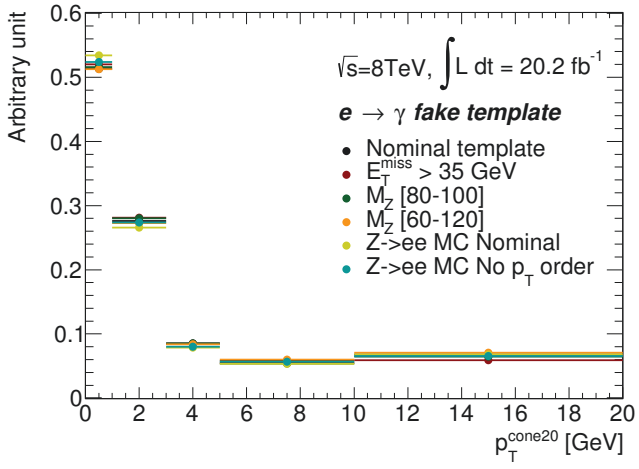

Figure 7.22.: The final template for photons faked by misidentified electrons together with the distributions to calculate the systematics for the template.

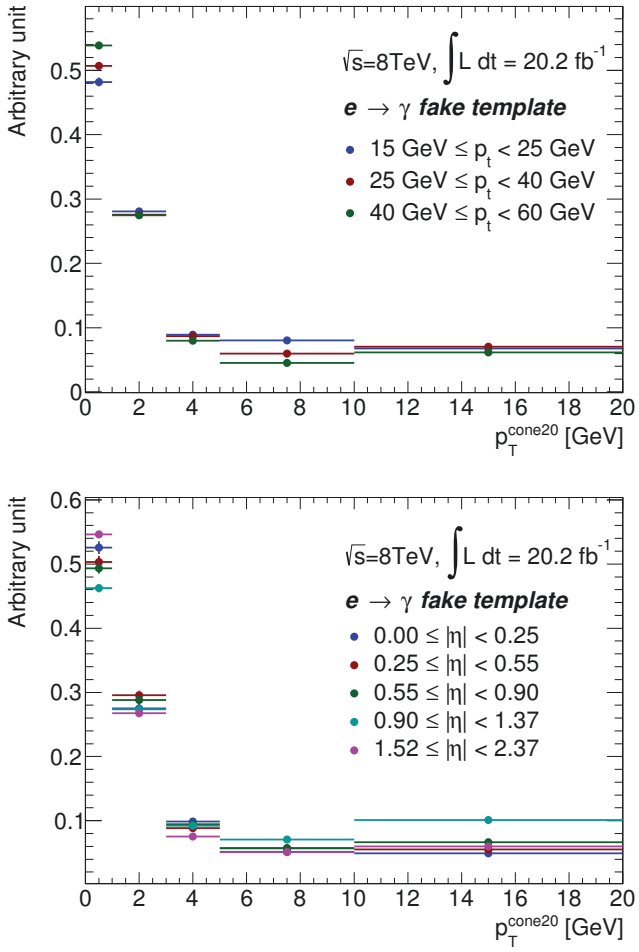

Figure 7.23.: Templates for photons faked by misidentified electrons in differential p_T and η bins.

7.3 Estimation of backgrounds with prompt photons

These backgrounds are the processes that are associated with a prompt photon in the final state such as W + jets, multi-jet, Z + jets, single top-quark and diboson productions. An example Feynman diagram for each production process is shown in figure 7.24. The contributions of W + jets and multi-jet production are estimated by use of data driven methods while the contributions of the other processes are estimated by use of MC samples.

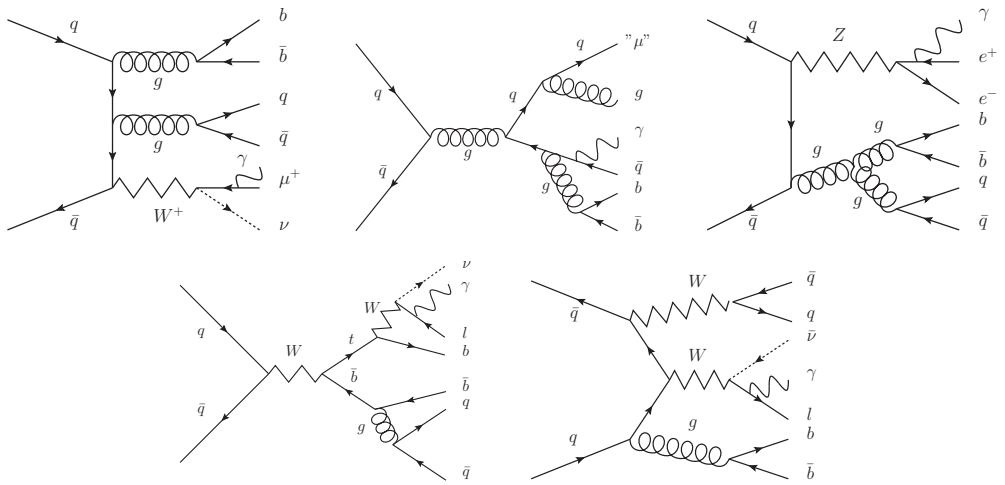

Figure 7.24.: Example representative Feynman diagrams for the background processes with a prompt photon.

7.3.1 W+jets events with a prompt photon

The largest contribution between backgrounds with a prompt photon comes from W + jets + γ events. This contribution is estimated by following the same method that is followed to estimate the number of signal events in the main maximum likelihood fit. In order to this, a control region is selected from data. The selection of the control region is optimised to select events dominated by $W + \text{jets} + \gamma$ events. The number of $W + \text{jets} + \gamma$ events is the estimated by performing a maximum likelihood template fit where the number of the $W + \text{jets} + \gamma$ events and the number backgrounds in this control region is estimated. As in the main fit, the number of signal, which is $W + \text{jets} + \gamma$ events in this case, and the number of hadronic fakes are free parameters in the fit where the other backgrounds are constant.

7.3.1.1 W + jets + γ control region

The selection of the control region is performed by applying the following requirements:

1. Requirement of at least one and at most three jets in the event.
2. Requirement of exactly one b-tagged jet.
3. Requirement of an invariant mass from lepton+photon system in the event being smaller then 40 GeV.

The selection ensures the suppression of $t\bar{t}\gamma$ events along with the domination of W + jets + γ events since the $t\bar{t}\gamma$ event topology requires at least four jets and at least one b-tagged jet. However, other background processes such as hadronic fakes, $e \to \gamma$ fakes and Z+jets+γ also contribute to the control region. Furthermore, minor contributions from single top-quark+γ, diboson+γ and multi-jet+γ are also expected in the control regions. The estimations of contributions from all non-W+jets+γ processes are performed the same manner as for the signal region. As mentioned in the introduction of this section, the hadronic fakes is a free parameter in the fit and therefore the final contribution of this process is extracted from the fit to the control region. Contributions of all other background processes are estimated from MC simulations.

The minor background contributions, Z+jets+γ, single top-quark+γ and diboson+γ are assigned with a 50% modelling uncertainty. This choice is made in order to be consistent with the choice made in the main fit to extract the cross section (cf. section 8.2.2). No other uncertainty is assigned to these processes, since the dominating uncertainty for these processes is expected to be the modelling uncertainty. The uncertainty on the contribution from the background with $e \to \gamma$ fakes is evaluated by varying functions and the range used for performing the fit to the m_Z distributions of $Z \to ee$ and $Z \to e\gamma$ control regions. The uncertainties on the template shapes of the hadronic fakes and $e \to \gamma$ fakes are simply assigned with the same uncertainty values evaluated for the signal region which are discussed in the previous sections, 7.2, and 7.2.1.2. A conservative value of 20% is considered for $t\bar{t}\gamma$ contamination in the control region, wile for the multi-jet+γ background, only statistical uncertainty is considered.

Table 7.7 summarises the contributions of each background process and the W+jets+γ events extracted by the fit. The post-fit distributions of the p_T^{cone20}20 isolation of photons are presented in figure7.25.

Table 7.7.: The observed number of $W + jets + \gamma$ events and expected background contributions in the W+jets+γ control region after the fit. The data - non-W+jets+γ value is the calculated by the fit by subtracting all the non-W+jets+γcontributions from the observed data. The errors include both statistical and systematic uncertainties.

Channel	data - non-W+jets+γ	Hadron Fake	$Z\gamma$ + Jets	$e \to \gamma$ Fake	$tt\gamma$	Diboson + γ	Single Top + γ	QCD + γ	data
e + jets	175.0 ± 39.1	95.0 ± 18.0	57.8 ± 23.4	124.6 ± 16.4	57.8 ± 11.1	0.5 ± 0.3	19.9 ± 8.7	16.3 ± 2.4	558.0 ± 23.6
μ + jets	278.2 ± 52.4	124.1 ± 21.7	90.8 ± 37.5	126.6 ± 17.6	82.0 ± 14.9	0.9 ± 0.4	8.0 ± 2.9	49.3 ± 4.8	774.0 ± 27.8

The data driven estimation of W + jets + γ contribution in the control region is compared to two different MC simulations samples. The samples are Sherpa $W + \gamma$ and Alpgen $W + \gamma$ samples. Details of the samples used are listed in table 7.8. The test of

Table 7.8.: The $W\gamma$ MC samples used to in the study.

MC	Process
Sherpa	$W + \gamma$ with up to three jets
Alpgen	$W + \gamma$ with up to five jets

of the data driven estimation is performed by calculating a so-called scale factor for each MC sample which is simply the ratio of the number of events estimated by data driven method to the number of expected events using MC samples. The calculated scale factors

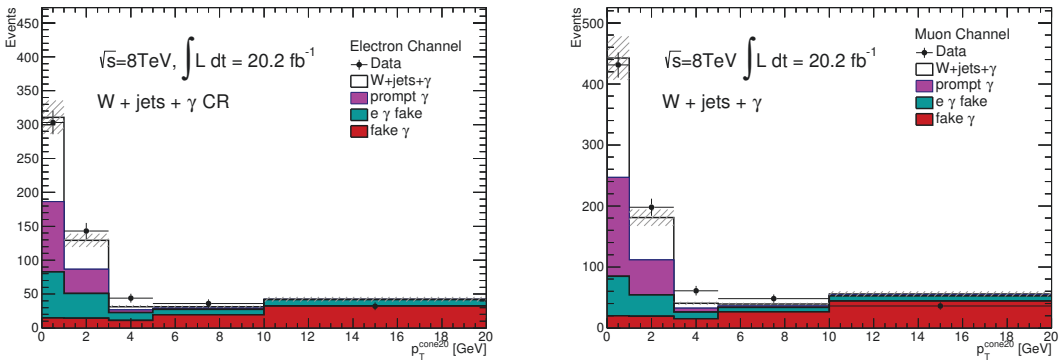

Figure 7.25.: Post-fit distributions of the photon track isolation for the electron and muon channels.

are listed in table 7.9. Since the scale factors are ratios of two independent values, the uncertainty on them are simply the quadratic sum of the uncertainties of the data-driven and MC-based estimations.

Table 7.9.: The $W\gamma$ scale factors calculated for the two sets of MC samples in the two control regions. The uncertainties of the scale factors are the quadratic sum of those of the data-driven estimated and MC predicted W+jets+γ event yields, with the latter being of MC statistics.

Channel	data - non-W+jets+γ	Sherpa	SF	Alpgen	SF
e + jets	174.6 ± 42.0	252.97 ± 10.84	0.69 ± 0.17	111.45 ± 4.10	1.58 ± 0.36
μ + jets	278.2 ± 58.0	365.66 ± 13.18	0.76 ± 0.15	149.46 ± 4.88	1.87 ± 0.36

The W+jets+γ contribution which is estimated in the control region defined above should be extrapolated to the signal region. This is performed via an extrapolation factor (EF) which is the ratio of the number estimated events in the signal region using MC simulation to the number of estimated events in the control region using MC.

$$EF = \frac{N^{SR}_{W+jets+\gamma,MC}}{N^{CR}_{W+jets+\gamma,MC}} \tag{7.11}$$

The EF is calculated for both MC samples given above and the results are listed in table 7.10. Among these MC samples, the Sherpa sample is chosen to be the nominal sample, since the Sherpa sample predicts more stable results than the Alpgen sample with respect to the control region. The final estimate of the $W + jets + \gamma$ contribution in the signal region is given in table 7.11. The uncertainties are the quadratic sum of the uncertainties of the data driven estimate and the extrapolation factor.

The contributions for the differential measurements are extrapolated from the inclusive fiducial phase space to the differential p_T and η bins using Sherpa MC. No systematic uncertainty is assigned to this extrapolation, since predictions of photon kinematics(p_T and η) distributions by Sherpa and Alpgen MC samples are observed to be very similar. The estimated contributions for the differential measurements are given in table 7.12.

Table 7.10.: The extrapolation factors for the two MC samples and their relative difference. The errors are the statistical uncertainties.

Channel		Control Region	Signal Region	Extrapolation	Difference (%)
e + jets	Sherpa	252.97 ± 10.84	96.76 ± 6.79	0.38 ± 0.03	–
	Alpgen	111.45 ± 4.10	30.80 ± 2.43	0.28 ± 0.02	27.74
μ + jets	Sherpa	365.66 ± 13.18	127.35 ± 8.01	0.35 ± 0.03	–
	Alpgen	149.46 ± 4.88	58.35 ± 3.55	0.39 ± 0.03	12.09

Table 7.11.: The estimated W+jets+γ event yields in the signal region, extrapolated from the control region, with the extrapolation factor being calculated from the two MC samples. The errors are the quadratic sum of those for the data-driven estimated $W + jets + \gamma$ in the control region and the statistics uncertainties of the corresponding extrapolation factors.

Channel	Sherpa	Alpgen
e + jets	67.1 ± 16.12	48.22 ± 11.51
μ + jets	96.7 ± 21.23	108.60 ± 21.59

Table 7.12.: The final estimated contributions W+jets+γ background in the signal region for the differential p_T and η bins. The first error is from the data-driven estimation method, while the second is from the difference between Sherpa and Alpgen generators.

Channel	$15 \leq p_T < 25$	$25 \leq p_T < 40$	$40 \leq p_T < 60$	$60 \leq p_T < 100$	$100 \leq p_T < 300$
e + jets	19.9 ± 4.7 ± 5.5	15.6 ± 3.7 ± 4.3	9.8 ± 2.3 ± 2.7	10.4 ± 2.4 ± 2.9	10.4 ± 2.5 ± 2.9
μ + jets	28.6 ± 5.7 ± 3.5	21.6 ± 4.3 ± 2.6	19.1 ± 3.8 ± 2.3	13.8 ± 2.7 ± 1.7	13.2 ± 2.6 ± 1.6
Channel	$0 \leq \lvert\eta\rvert < 0.25$	$0.25 \leq \lvert\eta\rvert < 0.55$	$0.55 \leq \lvert\eta\rvert < 0.90$	$0.90 \leq \lvert\eta\rvert < 1.37$	$1.37 \leq \lvert\eta\rvert < 2.37$
e + jets	9.2 ± 2.2 ± 2.5	11.8 ± 2.8 ± 3.3	13.0 ± 3.1 ± 3.6	14.2 ± 3.3 ± 3.9	18.8 ± 4.4 ± 5.2
μ + jets	9.8 ± 2.0 ± 1.2	17.6 ± 3.5 ± 2.1	18.7 ± 3.7 ± 2.3	21.7 ± 4.3 ± 2.6	29.4 ± 5.8 ± 3.5

7.3.2 Multi-jet (QCD) events with a prompt photon

The final state of $t\bar{t}\gamma$ signal in the single-lepton decay mode can be imitated by a final state of multiple jets with an associated photon or a photon originating from jet fragmentation and with one of the jets being misidentified as a tight lepton. An example for such a case is illustrated with Feynman diagram in figure 7.24.

This background contribution is estimated with a data driven method. First, a control sample enriched with $t\bar{t}$ events with fake leptons is extracted using the well-known and by ATLAS analyses widely used Matrix Method [89]. Based on the efficiency measurement of leptons with loosened identification criteria, the matrix method is developed to estimate backgrounds with non-prompt and fake leptons. Furthermore, photon related cuts of the nominal signal selection is applied to the control sample. Finally, a template fit is performed using the discriminating variable, p_T^{cone20}, where the prompt photon and hadron-fake templates are fitted to the final control sample in order to estimate the contribution of multi-jet events associated with a prompt photon.

Brief description of the matrix method

Since this background is characterized by the jets misidentified as leptons, the selection of the control sample is nothing but the nominal signal selection with loosened lepton definition. Explicitly, the control sample is extracted by using the nominal signal selection where no isolation requirement for both electron and muon is applied and where the rectangular cuts on the shower shapes of electrons are extended. In the following, this selection is referred to as *loose* selection while the selection with nominal lepton criteria, which is identical to the nominal signal selection, is referred to as *tight* selection. In terms of leptons, the leptons that are faked by misidentified jets are referred to as *fake* leptons while leptons selected by the nominal definition are referred to as *real* leptons.

The keystone of the matrix method that in a data sample selected by the tight, or the loose, selection and containing only one lepton, the number of events is assumed to be the linear sum of the events with the real and the fake leptons which are formulated as follows:

$$\begin{aligned} N^t &= N_r^t + N_f, \\ N^l &= N_r^l + N_f^l. \end{aligned} \tag{7.12}$$

The events selected by the tight selection can also be expressed as follows:

$$N^t = f_r N_r^l + f_f N_f^l, \tag{7.13}$$

where f_r and f_f are the fractions of leptons, the reals and the fakes respectively, that pass both the loose and the tight selections. With these fractions, which are measured using a data control sample enriched with the real and the fake leptons[89], the number of tight events with fake leptons can be formulated as follows:

$$N_f = \frac{f_f}{f_r - f_f}\ (f_r\ N^l - N^t). \tag{7.14}$$

This number corresponds the number of $t\bar{t}$ events with fake leptons that pass the tight selection. Furthermore, the measured fractions, f_r and f_f, depend on lepton kinematics and event characteristics, such as the number of jets or b-jets. In order for an accurate calculation of the fractions, an event weight is taken into account which is a parametrisation of the fractions as a function of the various object kinematics. The parametrisation

is described in details elsewhere [89]. The event weight is formulated as follows:

$$w_i = \frac{f_f}{f_r - f_f}\ (f_r - \delta_i), \tag{7.15}$$

where δ_i is equal to 1 if the loose lepton in the event i passes the tight selection as well and 0 otherwise. The presented analysis uses the w_i values that are centrally provided by the ATLAS Top Working Group.

Estimation of the final contribution

Estimation of the multi-jet background contribution proceeds with the application of photon related cuts on the events selected using the loose selection. These events are then weighed in accordance with equation 7.15. The procedure yields 12.7±3.9 and 24.6±5.5 events in the electron and muon channels, respectively. The data distributions in figure 7.26 represents the isolation of the photons in the selected events for both channels. The final step of the estimation is the fitting of the prompt and the hadron-fake templates to the selected data events. The post-fit distributions for both channels are shown in figure 7.26. The background contribution of multi-jet events with a prompt photon is estimated to be 7.5 ± 3.6 and 8.3 ± 5.2 events in the electron and muon channels, respectively, with the errors coming from the statistical fluctuation.

The fitting procedure is iterated for each photon p_T and η bins for the differential measurement. The results are summarized in table 7.13 and table 7.14 for the fiducial and the differential measurements.

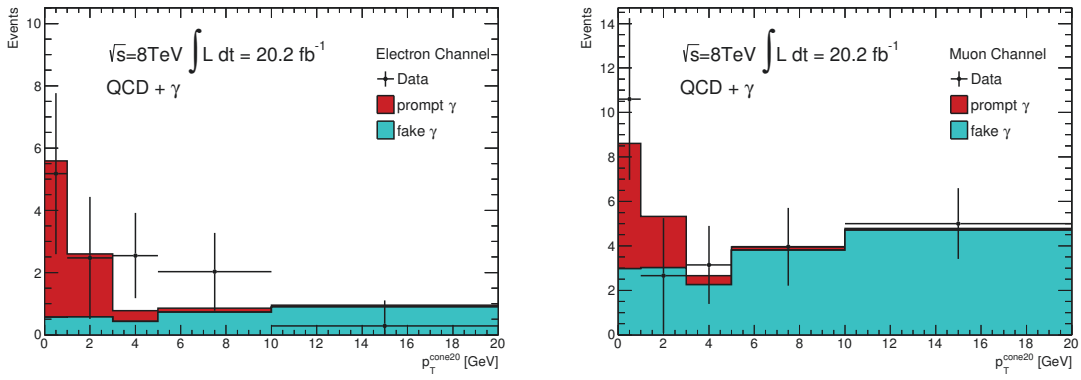

Figure 7.26.: Distribution of ΔR between the reconstructed and the matrix element photon after the nominal event selection.

Table 7.13.: The estimated QCD + γ background events in each photon $p_T$bins. The uncertainty is statistical only.

p_T nin [GeV]	15≤ p_T <25	25≤ p_T <40	40≤ p_T <60	60≤ p_T <100	100≤ p_T <300
e + jets	2.2 ± 1.7	1.9 ± 1.7	0.8 ± 1.4	1.7 ± 1.5	0.4 ± 0.7
μ + jets	5.2 ± 3.6	0.0 ± 2.1	3.0 ± 2.0	0.0 ± 1.1	0.0 ± 0.1

Table 7.14.: The estimated QCD + γ background events in each photon η bins. The uncertainty is statistical only.

η bin	$0 \leq \lvert\eta\rvert < 0.25$	$0.25 \leq \lvert\eta\rvert < 0.55$	$0.55 \leq \lvert\eta\rvert < 0.90$	$0.90 \leq \lvert\eta\rvert < 1.37$	$1.37 \leq \lvert\eta\rvert < 2.37$
e + jets	2.6 ± 1.3	0.0 ± 0.3	2.0 ± 1.3	2.9 ± 1.5	2.7 ± 1.8
μ + jets	1.6 ± 1.8	2.1 ± 2.5	0.0 ± 0.8	0.5 ± 3.2	1.4 ± 2.5

7.3.3 Other backgrounds with a prompt photon

The contributions of the rest of the background processes with a prompt photon radiation, which are Z +jets, single top-quark and diboson productions, are estimated by use of MC samples. For each process, a dedicated MC simulation provided centrally by the ATLAS collaboration is used. The nominal event selection is applied on the MC simulations to estimate the background contributions to the signal. Background events with fake photons can contaminate these selected background events with prompt photons. Since fake photon background contributions are estimated separately, this contamination should be discarded. This is carried out by use of true information record in the MC simulations by checking the *origin* and *type* of photons. The contributions from backgrounds with a prompt photon radiation is summarised in table 7.15. The associated errors are the statistical uncertainties. The contributions for the differential measurement are summarised in table 7.16 and table 7.17.

Table 7.15.: The expected yields of prompt photon background events from MC. The numbers are normalised to the total integrated luminosity of 20.2 fb^{-1} and statistical uncertainties are given.

Process	e + jets	μ + jets
$Z\gamma$ + jets	35.4 ± 2.3	37.5 ± 2.3
Single top + γ	13.3 ± 3.1	18.9 ± 3.7
Diboson + γ	2.2 ± 0.6	1.8 ± 0.5

Table 7.16.: The expected yields of prompt photon background events in each photon p_T bins from MC. The numbers are normalised to the total integrated luminosity of 20.2 fb^{-1} and statistical uncertainties are given.

p_T Bin (GeV)		$15 \leq p_T < 25$	$25 \leq p_T < 40$	$40 \leq p_T < 60$	$60 \leq p_T < 100$	$100 \leq p_T < 300$
e + jets	$Z\gamma$ + jets	9.5 ± 0.9	9.3 ± 0.9	7.6 ± 0.8	5.8 ± 0.7	2.7 ± 0.5
	Single Top + γ	2.2 ± 1.0	2.2 ± 1.0	4.9 ± 1.5	3.8 ± 1.3	0.9 ± 0.6
	Diboson + γ	0.6 ± 0.1	0.4 ± 0.1	0.2 ± 0.1	0.7 ± 0.4	0.2 ± 0.1
μ + jets	$Z\gamma$ + jets	13.2 ± 1.0	12.9 ± 1.1	5.3 ± 0.6	4.1 ± 0.5	1.7 ± 0.4
	Single Top + γ	5.4 ± 1.6	4.4 ± 1.4	5.0 ± 1.5	4.1 ± 1.4	0.0 ± 0.1
	Diboson + γ	0.3 ± 0.1	0.9 ± 0.3	0.2 ± 0.1	0.3 ± 0.1	0.1 ± 0.1

Table 7.17.: The expected yields of prompt photon background events in each photon η bins from MC. The numbers are normalised to the total integrated luminosity of 20.2 fb^{-1} and statistical uncertainty are given.

η Bin		$0 \leq \lvert\eta\rvert < 0.25$	$0.25 \leq \lvert\eta\rvert < 0.55$	$0.55 \leq \lvert\eta\rvert < 0.90$	$0.90 \leq \lvert\eta\rvert < 1.37$	$1.37 \leq \lvert\eta\rvert < 2.37$
e + jets	$Z\gamma$ + jets	5.1 ± 0.7	4.7 ± 0.6	7.4 ± 0.8	8.7 ± 0.9	9.3 ± 0.9
	Single Top + γ	1.4 ± 0.8	1.5 ± 0.8	1.2 ± 0.7	5.6 ± 1.6	4.3 ± 1.4
	Diboson + γ	0.8 ± 0.4	0.3 ± 0.1	0.3 ± 0.1	0.5 ± 0.1	0.3 ± 0.1
μ + jets	$Z\gamma$ + jets	4.3 ± 0.6	6.5 ± 0.7	8.2 ± 0.8	8.5 ± 0.8	9.8 ± 0.9
	Single Top + γ	2.6 ± 1.1	2.2 ± 1.0	2.1 ± 1.0	3.6 ± 1.3	8.5 ± 1.9
	Diboson + γ	0.2 ± 0.1	0.7 ± 0.3	0.1 ± 0.1	0.3 ± 0.1	0.5 ± 0.1

Chapter 8

Systematic uncertainties

Systematic uncertainties affecting the cross section measurement can be categorised in three groups:
Experimental uncertainties: Uncertainties induced by the experimental setup related calibrations. This category includes numerous sources of uncertainties but mainly such as the uncertainties of the reconstruction and identification as well as the calibrations of the kinematics measurements such as energy and momentum measurement. The uncertainties induced by the pile-up events and uncertainty of the measured integrated luminosity is also included in this category.
Modelling uncertainties: Uncertainties induced by MC modelling of the signal and three of the background processes: Z+jets+γ, single top+γ and diboson+γ.
Template-related uncertainties: Uncertainties induced by the methods used to extract the templates for the fit.

8.1 Experimental uncertainties

Experimental uncertainties affect the parts of the analysis where detector modelling is involved. Namely, the signal correction factor, prompt photon template and the backgrounds that are estimated from MC simulations.

The effect of the each uncertainty is calculated individually by varying each systematic source up and down by 1σ. The calculated responses on the signal correction factors for the inclusive and the differential cross-sections are listed in tables 8.1 and 8.2. The responses are in fact not symmetric in positive and negative directions. However, they are, simply for convenience, symmetrised by taking the larger variation as the systematics uncertainty for both directions. There are a few cases where the experimental uncertainty is evaluated not by calculating 1σ variation but rather by varying a cut value, e.g. for JVF, or by varying calibration scale factors, e.g. b-tagging uncertainty. In such cases, the variation values are provided centrally by the related working group with in the ATLAS collaboration.

The responses of the experimental uncertainties on the prompt photon template are listed in table 8.3 for each bin of the template.

Finally, the responses of the experimental uncertainties on the backgrounds estimated from MC are not presented, since the contributions of these backgrounds are remarkably small in the signal region and their uncertainties are dominated by the *assumed* modelling uncertainties which will be described in section 8.2.

Leptons
The trigger, reconstruction, identification and isolation efficiencies of the lepton in the event are corrected for the simulated events according to the data expectation by using the so-called scale factors. The scale factors are basically the ratio of the efficiencies obtained in data over the efficiencies obtained using MC simulations. The efficiencies used for the calculation of the scale factors are obtained by the use of the tag-and-probe method on $Z \to ee$, $J/\Psi \to ee$ and $Z \to \mu\mu$ decays.

In addition, the scale and resolution of the lepton energy and momentum are calibrated by the help of MC-based methods. Any possible detector mis-modelling in the calibration is corrected by applying the so-called correction factors obtained from studies of dileptonic Z-boson decays. As usual, the correction factors are varied up and down by 1σ to investigate the uncertainty on the lepton energy and momentum.

The resolution of lepton energy and momentum is found to be slightly worse in data than in MC. A smearing is applied to the lepton energy and momentum in MC samples to take this difference into account. The smearing factor is varied to investigate the uncertainty on the resolution of lepton energy and momentum.

Photons
The systematic uncertainties on the photon identification efficiency is studied by making use of radiative and non-radiative Z-boson decays, $Z \to ee$ and $Z \to ee\gamma$, and by exploiting the resemblance between the electromagnetic showers of electrons and photons in the ECAL.

A ratio of the efficiencies calculated for data to that in MC is taken as the scale factor and applied to MC samples for correction of detector mis-modelling. The scale factors are varied to investigate their effects on the measurement. The uncertainty on the resolution and scale of photon energy is studied by following the same procedure as for leptons.

Jets
The calibration of jets, conventionally referred to as jet energy scale (JES), depends on several components such as behaviour of high-p_T jets, energy scale of b-jets, modelling and statistical uncertainties on the extrapolation of the jet calibration from the central region of detector to the full acceptance, as well as uncertainties due to the pile-up events and in-situ jet corrections. The JES uncertainty is evaluated by varying each source independently by its corresponding uncertainty. Fractional components of the jet energy scale uncertainties are presented in figure 8.1 as a function of transverse momentum and pseudo-rapidity.

The resolution of jets (JER) is measured by making use of p_T-balance measurement technique using the processes of which physics is well-known, such as γ+jets or Z+jets events. Data and MC are found to be in good agreement. Similar to the situation for JES, JER uncertainty also consists of several independent sources. The procedure to calculate the JER systematic uncertainty is identical to that for the JES uncertainty.

The systematic uncertainty associated to the jet vertex fraction is studied by varying the cut value on the JVF up and down.

***b*-tagging**
The uncertainty of the b-tagging process is evaluated by varying the calibration scale factors. The scale factors are provided for $b-$, $c-$ and light flavour jets.

Missing transverse energy
As given in section 4.5, the reconstruction of the missing transverse energy depends on other reconstructed physical objects in the event. Therefore some portion of the uncertainty on the missing transverse energy is originated from the propagation of the uncer-

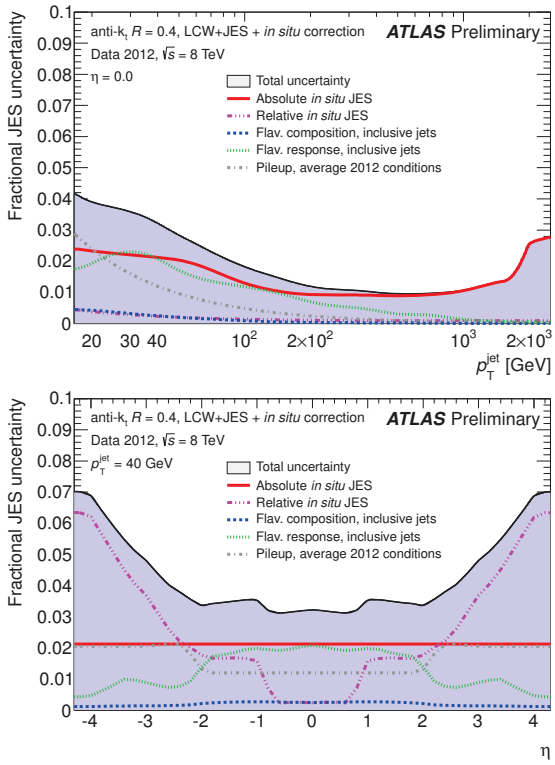

Figure 8.1.: Fractional jet energy scale systematic uncertainty components as a function of p_T (left) and η (right) for anti-k_T jets at $|\eta| = 0.0$ (left) and $p_T = 40$ GeV (right) with radius parameter of $R = 0.4$ calibrated using the LCW+JES calibration scheme. The total uncertainty (all components summed in quadrature) is shown as a filled blue region topped by a solid black line.

tainties of the other objects onto the uncertainty of E_T^{miss}. In addition, the uncertainties on the two other terms, $E_{x,y}^{RefSoftJet}$, $E_{x,y}^{CellOut}$ are also taken into account. The uncertainty of the scale of the soft terms are determined from the comparison of MC to data. The soft-term resolution uncertainty is determined in terms of the x and y components of E_T^{miss}. The uncertainty originated by energy scale and energy resolution components in the soft term are varied up and down by 1σ to investigate their effects on the measurement.

Pile-up

The uncertainty due to the pile-up events is determined by varying the nominal value of the rescaling parameter μ, 1.09, by ± 0.04. The uncertainty is found to be negligible.

Luminosity

The uncertainty of the integrated data luminosity is provided centrally by ATLAS and is 1.9%.

Table 8.1.: Experimental systematic uncertainties of the signal correction factors for inclusive and the p_T differential measurement in the electron and muon channels. The uncertainties are given in per cent, and only the leading 10 sources are presented. The quadratic sum represents the sum of all uncertainties [87].

p_T bins (GeV)		Inclusive	{15, 25)	{25, 40)	{40, 60)	{60, 100)	{100, 300}
e + jets (%)	JES EffectiveNP Modelling1	2.8	3.0	3.0	2.9	2.6	2.1
	e Identification ϵ	2.4	2.4	2.4	2.4	2.4	2.4
	JES RhoTopology	2.1	2.4	2.4	2.2	1.7	1.7
	JES FlavourResponse	-1.6	-1.8	-1.9	-1.7	-1.3	-1.1
	JES EffectiveNP Statistical1	1.1	1.3	1.1	1.1	0.9	1.2
	γ Identification ϵ	1.1	1.8	1.3	0.7	0.3	0.4
	e Trigger	1.1	1.0	1.0	1.0	1.2	1.3
	JES EtaIntercalibration TotalStat	0.7	0.9	0.7	0.8	0.6	0.8
	γ Energy Scale	-0.7	0.2	-0.6	-1.2	-0.9	-1.7
	JES NPVOffsetTerm	-0.7	-0.9	-0.7	-0.7	-0.6	-0.8
	Quadratic Sum	5.2	5.8	5.7	5.4	4.9	5.0
μ + jets (%)	JES EffectiveNP Modelling1	2.7	2.8	2.7	2.9	2.9	2.2
	JES RhoTopology	2.0	2.2	1.9	2.2	2.2	1.6
	μ Trigger	1.8	1.8	1.8	1.8	1.8	1.8
	JES FlavourResponse	-1.4	-1.6	-1.3	-1.7	-1.6	-1.3
	γ Identification ϵ	1.1	1.8	1.3	0.7	0.3	0.4
	JES EffectiveNP Statistical1	1.1	1.2	1.1	1.0	1.2	0.8
	JES NPVOffsetTerm	-0.7	-0.9	-0.7	-0.9	-0.9	-1.0
	JES EtaIntercalibration TotalStat	0.7	0.9	0.7	0.7	0.8	0.6
	γ Energy Scale	-0.7	0.4	-0.5	-0.9	-1.8	-1.8
	JER NP2	0.6	0.9	0.4	0.3	1.2	-0.1
	Quadratic Sum	4.8	5.4	4.8	5.1	5.7	4.4

8.2 Modelling uncertainties

An important systematic uncertainty source on the measurement is the modelling of the processes using MC simulations. Among them, the modelling of the signal process is of great importance. The modelling, or generation, of these processes depends on several parameters such as parton distribution functions of the colliding protons, initial and final state radiations (ISR, FSR) and, being specific to the signal process, choice of the renormalisation and factorisation scales (μ_R and μ_F) mentioned in formula 2.1. These sources and more are discussed in the following.

Table 8.2.: Experimental systematic uncertainties of the signal correction factors for inclusive and the η differential measurement in the electron and muon channels. The uncertainties are given in per cent, and only the leading 10 sources are presented. The quadratic sum represents the sum of all uncertainties. [87].

η bins		Inclusive	{0.0, 0.25)	{0.25, 0.55)	{0.55, 0.90)	{0.90, 1.37	{1.37, 2.37)
e + jets (%)	JES EffectiveNP Modelling1	2.8	3.0	3.0	2.6	2.4	2.8
	e Identification ϵ	2.4	2.4	2.4	2.4	2.4	2.4
	JES RhoTopology	2.1	2.1	2.4	2.1	1.9	2.1
	JES FlavourResponse	-1.6	-1.5	-1.9	-1.6	-1.6	-1.6
	JES EffectiveNP Statistical1	1.1	1.2	1.3	1.3	1.0	1.1
	γ Identification ϵ	1.1	0.9	0.9	1.1	1.2	1.5
	e Trigger	1.1	1.1	1.0	1.1	1.1	1.1
	JES EtaIntercalibration TotalStat	0.7	0.8	0.8	0.9	0.8	0.7
	γ Energy Scale	-0.7	-0.5	-0.7	-0.8	-0.6	-1.4
	JES NPVOffsetTerm	-0.7	-0.7	-0.7	-0.6	-0.7	-0.9
	Quadratic Sum	5.2	5.4	5.6	5.3	5.0	5.7
μ + jets (%)	JES EffectiveNP Modelling1	2.7	2.9	2.7	2.8	2.4	2.8
	JES RhoTopology	2.0	2.1	2.1	2.2	1.7	2.1
	μ Trigger	1.8	1.8	1.8	1.8	1.8	1.8
	JES FlavourResponse	-1.4	-1.5	-1.5	-1.4	-1.1	-1.6
	γ Identification ϵ	1.1	0.9	0.9	1.1	1.2	1.5
	JES EffectiveNP Statistical1	1.1	1.1	0.9	1.2	1.0	1.2
	JES NPVOffsetTerm	-0.7	-0.7	-0.8	-1.0	-0.6	-0.9
	JES EtaIntercalibration TotalStat	0.7	0.8	0.6	0.8	0.6	0.9
	γ Energy Scale	-0.7	-0.4	-0.5	-0.6	-0.6	-1.3
	JER NP2	0.6	0.2	0.9	1.0	0.5	0.3
	Quadratic Sum	4.8	5.0	4.8	5.3	4.4	5.3

8.2.1 Signal modelling

Renormalisation and factorisation scales:
As mentioned in the previous chapter, the choice of μ_R and μ_F scales for the nominal sample is $2m_{top}$. In order to adjust a systematic uncertainty on this choice, samples with μ_R and μ_F varied up and down by factor two (m_{top} and $4m_{top}$) are compared to the nominal sample at four-vector level. It is found out that behaviours of the variation samples are symmetric. Motivated with this fact, generation of only one sample, the one with m_{top} scale, is performed. The systematic uncertainty is then evaluated by comparing the variation and the nominal sample at detector level. The response of the variation on the signal correction factor is found to be 0.6% and 0.3% for the electron and muon channels respectively, while the responses on the acceptances are found to be 3.9% and 2.7% for the electron and muon channels respectively. The study is repeated for the differential p_T and η bins and results are listed in tables 8.4 and 8.5.

The choice of the μ_R and μ_F scales affects also the prompt photon template. It can be seen in figure 8.2 that this effect is negligible. The situation remains the same in the differential bins.

Modelling of the parton shower and hadronisation: The parton showering and hadronisation of the events are modelled by matching the ME generator to a parton shower generator. For this purpose the nominal signal sample, MADGRAPH, is matched to PYTHIA. The uncertainty of this choice is evaluated by comparing the nominal matching, MADGRAPH+PYTHIA, to a matching where the parton shower generator is replaced by HERWIG. The response of this variation on the correction factors are found to be 0.7% and -1.3% for the electron and muon channels. The results for the differential p_T and η bins are listed in tables 8.4 and 8.5. Furthermore, the response of the parton shower and hadronisation variation on the prompt photon template is investigated and presented in

Table 8.3.: Experimental systematic uncertainties of the prompt photon template in the electron and muon channels for the fiducial measurement. The uncertainties are given in per cent, and only the leading 10 sources are presented. The quadratic sum represents the sum of all uncertainties.

p_T^{iso} bins (GeV)		{0, 1)	{1, 3)	{3, 5)	{5, 10)	{10, ∞)
e + jets (%)	JES EffectiveNP Modelling1	-0.0	-0.1	0.4	1.3	2.9
	e Identification ϵ	-0.0	0.0	0.0	-0.0	-0.0
	JES RhoTopology	-0.0	-0.1	-0.3	1.7	0.8
	JES FlavourResponse	0.1	-0.2	0.3	-1.7	0.7
	JES EffectiveNP Statistical1	0.0	-0.1	-0.2	0.4	-0.5
	γ Identification ϵ	0.0	-0.0	-0.1	-0.1	-0.3
	e Trigger	-0.0	0.1	0.1	-0.1	-0.1
	JES EtaIntercalibration TotalStat	0.0	-0.1	0.2	-0.4	0.6
	γ Energy Scale	-0.1	0.0	0.3	-0.2	1.0
	JES NPVOffsetTerm	-0.3	0.6	1.5	0.8	-2.5
	Quadratic Sum	0.5	1.1	3.5	4.0	9.0
μ + jets (%)	JES EffectiveNP Modelling1	0.1	-0.1	0.2	-0.5	1.7
	JES RhoTopology	0.1	-0.2	0.1	-0.3	1.0
	μ Trigger	-0.0	0.0	0.0	0.0	-0.0
	JES FlavourResponse	-0.1	0.2	-0.0	0.3	-1.4
	γ Identification ϵ	0.0	-0.0	-0.1	-0.2	-0.3
	JES EffectiveNP Statistical1	0.0	-0.1	0.0	-0.6	0.6
	JES NPVOffsetTerm	-0.3	0.6	1.0	0.3	-0.3
	JES EtaIntercalibration TotalStat	0.0	-0.0	0.0	-0.7	1.1
	γ Energy Scale	-0.1	0.1	0.4	0.2	0.5
	JER NP2	0.1	-0.2	0.5	0.1	-1.7
	Quadratic Sum	0.4	0.8	1.9	2.6	5.6

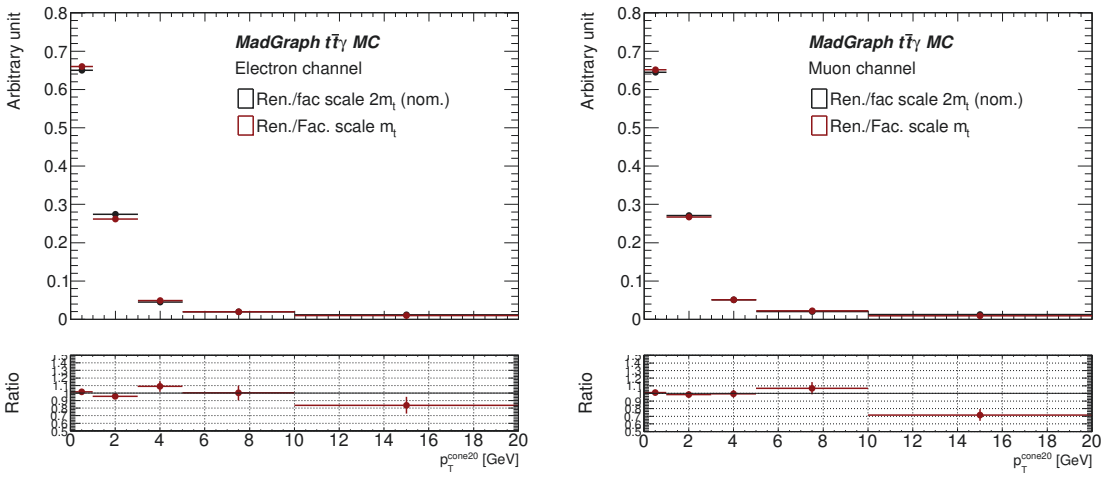

Figure 8.2.: QCD scale variations of the signal photon isolation distribution in the electron and muon channels. The deviation in the last bin is safe to be ignored since very few prompt photons fall into it.

Table 8.4.: Modelling uncertainties for the acceptance and correction factors in each photon p_T bin. Errors are originated from the limited statistics of the samples.

p_T bins [GeV]			1 {15, 25)	{25, 40)	{40, 60)	{60, 100)	{100, 300}
QCD Scale Unc. (%)	A	e + jets	-2.4 ± 0.9	-5.3 ± 1.0	-2.8 ± 1.4	-5.3 ± 1.5	-5.4 ± 1.7
		μ + jets	-1.8 ± 0.9	-3.5 ± 1.1	-3.0 ± 1.4	-0.7 ± 1.6	-3.7 ± 1.8
	C	e + jets	0.0 ± 2.0	-1.7 ± 2.0	-2.1 ± 2.3	1.0 ± 2.7	1.5 ± 2.8
		μ + jets	-0.3 ± 1.4	1.5 ± 1.3	-1.9 ± 1.4	-2.0 ± 1.5	1.2 ± 1.6
PS Unc. (%)	A	e + jets	-2.9 ± 0.9	-7.2 ± 1.0	-7.1 ± 1.3	-3.8 ± 1.6	-4.9 ± 1.8
		μ + jets	-5.1 ± 0.9	-5.6 ± 1.1	-6.1 ± 1.4	-2.6 ± 1.7	-4.9 ± 1.9
	C	e + jets	1.5 ± 2.1	2.1 ± 2.1	0.2 ± 2.5	3.3 ± 2.9	-3.3 ± 2.9
		μ + jets	-0.6 ± 1.5	-1.7 ± 1.4	-2.9 ± 1.6	-1.1 ± 1.8	1.0 ± 2.0
ISR/FSR Unc. (%)	A	e + jets	2.9 ± 1.0	3.2 ± 1.1	1.4 ± 1.4	2.8 ± 1.6	3.3 ± 1.8
		μ + jets	1.4 ± 1.0	2.8 ± 1.1	4.7 ± 1.5	4.4 ± 1.7	1.4 ± 1.8
	C	e + jets	-2.0 ± 2.0	-3.7 ± 1.9	-4.3 ± 2.3	-9.6 ± 2.8	-2.0 ± 2.6
		μ + jets	-0.3 ± 1.4	-2.6 ± 1.2	-1.7 ± 1.4	-3.8 ± 1.5	-2.1 ± 1.6
PDF Unc. (%)	A	e + jets	0.9	0.9	1.0	0.9	1.0
		μ + jets	1.0	0.9	0.8	1.0	0.9
	C	e + jets	0.3	0.3	0.3	0.3	0.1
		μ + jets	0.1	0.2	0.2	0.4	0.2

Table 8.5.: Modelling uncertainties for the acceptance and correction factors in each photon η bin. Errors are originated from the limited statistics of the samples.

η bins			{0.0, 0.25)	{0.25, 0.55)	{0.55, 0.90)	{0.90, 1.37	{1.37, 2.37)
QCD Scale Unc. (%)	A	e + jets	-2.2 ± 1.3	-3.9 ± 1.2	-5.1 ± 1.2	-3.9 ± 1.2	-4.0 ± 1.2
		μ + jets	-0.5 ± 1.4	-2.0 ± 1.3	-2.7 ± 1.3	-1.6 ± 1.2	-5.3 ± 1.2
	C	e + jets	-3.7 ± 2.2	0.8 ± 2.2	2.4 ± 2.3	-5.1 ± 2.1	2.9 ± 2.8
		μ + jets	0.1 ± 1.5	1.8 ± 1.3	-1.1 ± 1.4	-3.3 ± 1.4	-0.2 ± 1.8
PS Unc.(%)	A	e + jets	-3.4 ± 1.3	-4.9 ± 1.2	-5.4 ± 1.2	-5.4 ± 1.2	-6.3 ± 1.2
		μ + jets	-3.2 ± 1.4	-6.0 ± 1.2	-4.8 ± 1.2	-6.0 ± 1.2	-5.6 ± 1.2
	C	e + jets	-3.0 ± 2.3	4.2 ± 2.3	2.7 ± 2.4	-5.6 ± 2.3	5.1 ± 2.9
		μ + jets	-1.6 ± 1.7	1.7 ± 1.5	-2.8 ± 1.6	-1.0 ± 1.6	-3.3 ± 1.9
ISR/FSR Unc. (%)	A	e + jets	5.3 ± 1.4	3.0 ± 1.2	1.2 ± 1.2	0.7 ± 1.2	3.5 ± 1.2
		μ + jets	2.7 ± 1.4	2.4 ± 1.3	2.6 ± 1.3	2.5 ± 1.3	1.6 ± 1.2
		e/μ + jets	4.0 ± 1.0	2.6 ± 0.9	1.5 ± 0.9	1.3 ± 0.9	2.5 ± 0.9
	C	e + jets	-6.5 ± 2.1	-5.1 ± 2.2	-4.4 ± 2.3	-1.9 ± 2.2	-4.7 ± 2.8
		μ + jets	-3.9 ± 1.5	1.0 ± 1.3	-2.1 ± 1.4	-4.3 ± 1.4	-3.0 ± 1.7
PDF Unc. (%)	A	e + jets	0.7	0.8	0.8	0.8	1.6
		μ + jets	0.7	0.7	0.8	0.8	1.8
	C	e + jets	0.3	0.1	0.2	0.3	0.2
		μ + jets	0.2	0.2	0.2	0.4	0.8

figure 8.3.

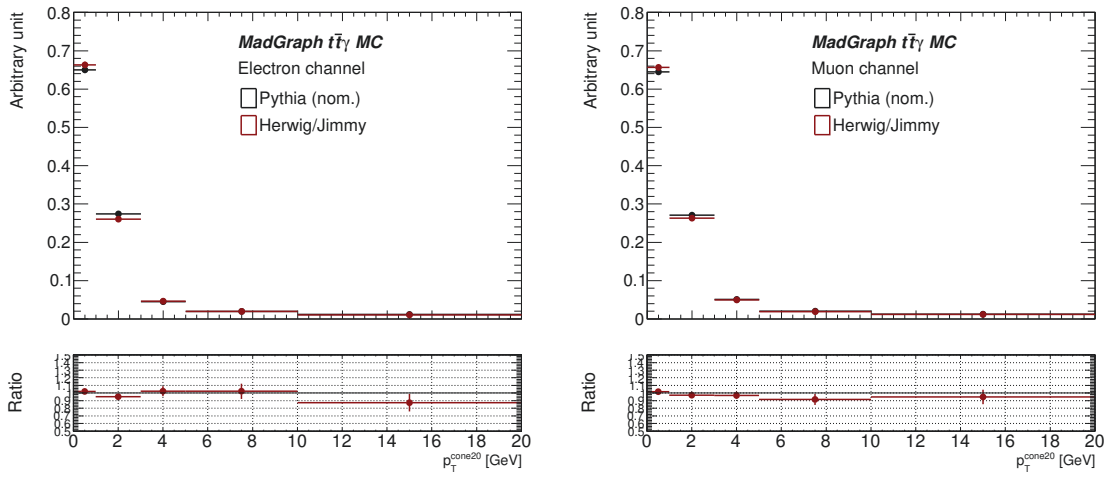

Figure 8.3.: Comparison of different parton shower modelings in terms of the signal photon isolation distribution in the electron and muon channels. The deviation in the last bin is safe to be ignored since very few prompt photon falls into it.

Initial and final state radiations: The modelling of initial- and final-state radiations uncertainty is evaluated by comparing the nominal signal sample, MADGRAPH+PYTHIA, to variation samples produced by varying the tune for QCD radiation activity in PYTHIA to higher and lower activity. The responses, which are symmetrised, on the correction factors are found to be 1.8% and 2.1% for the electron and muon channels, respectively, while the responses on the fiducial region acceptances are 2.4% and 1.2%. The evaluation is repeated for each differential p_T and η bin. The results are listed in tables 8.4 and 8.5. As usual, the response of ISR/FSR variation on the prompt photon template is investigated and presented in figure 8.4. Some remarkable but statistically not very significant uncertainties are seen in the region beyond 3 GeV.

Parton distribution function: Another modelling uncertainty is induced by the modelling of the parton distribution function (PDF) set. The nominal PDF choice is CT10 which has 52 eigenvector sets itself. The uncertainty of the PDF choice includes two stages. In the first stage, the variations of the 52 CT10 eigenvectors with respect to the nominal CT10 set are summed in quadrature. In the second stage, the nominal sample is compared with two other choices of PDF sets: the NNPDF, and the MSTW, by reweighting technique. Reweighting is useful for getting an idea of PDF uncertainties without having to generate several samples. Instead of generating multiple samples with a different PDF, event weights are used to reweight a sample produced with one PDF. This provides the possibility to have a prediction of a MC sample, if it was produced with another PDF set. The final vales of the uncertainty is the envelope of the summed CT10 eigenvector-variations and the variations of the NNPDF and the MSTW PDF sets from the nominal choice, CT10. The results are found to be 1.4% on the fiducial region acceptances for both channels while 0.2% and 0.3% on the correction factor for the electron and muon channels respectively. The corresponding uncertainties for the differential p_T and η bins are summarised in tables 8.5 and 8.5. As a consequence of the reweighting method, no statistical error exist on the systematic uncertainty as can be seen in the tables. The prompt photon template is not expected to be sensitive to the choice of PDF set.

Colour reconnection, underlying event and QED uncertainties: The effects of

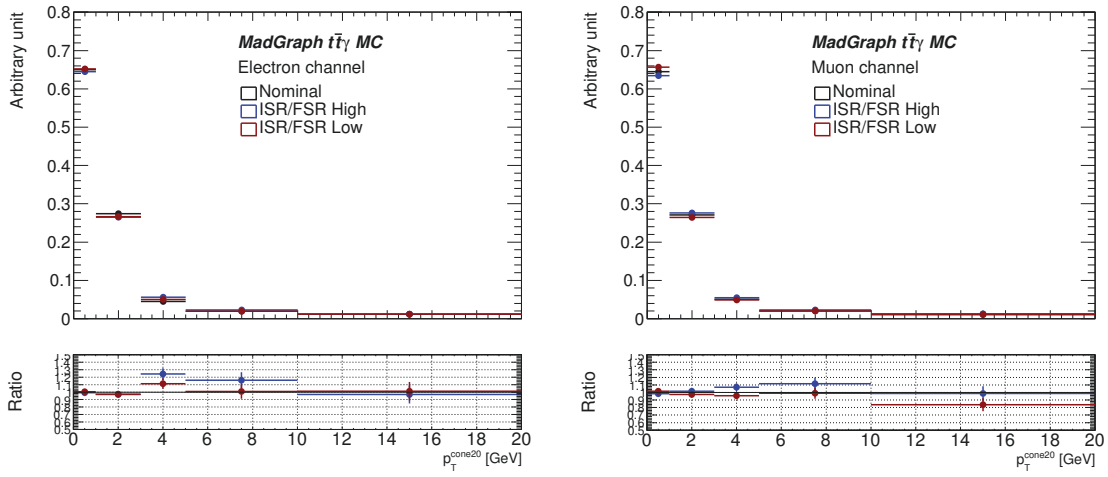

Figure 8.4.: Initial- and final-state radiation variations of the signal photon isolation distribution in the electron and muon channels. The deviation in the last bin is safe to be ignored since very few prompt photon falls into it.

these two MC modelling features on the isolation variables and the event selection yields are found out to be negligible as a result of studies performed with samples at the particle level. Therefore no dedicated samples have been generated for these features and no systematic uncertainty is considered.

8.2.2 Background modelling

All the sources originating from modelling above affect also the backgrounds that are estimated using MC: Z+jets+γ, single top+γ and diboson+γ. As evaluated in section 7.3, the contribution of these background processes are minor. This fact allows to handle the modelling systematic uncertainties for these processes conservatively by simply assigning 50% uncertainty, for the sake of simplicity.

8.3 Template-related uncertainties

Almost all of the uncertainties originating from the methods of extracting the templates are discussed in the dedicated sections: For the signal photon template in section 7.1, for the hadronic fake template in 7.2 and for the photons faked by electrons in section 7.2.1.2. Furthermore, since signal photon template is extracted using MC, the template is subject to modelling uncertainties which is discussed in section 8.2. However, there is still one missing point to be discussed in the context of template related uncertainties. As described in the chapter dedicated to the analysis strategy, the signal photon template is also used to describe the isolation behaviour of the prompt photons from the background processes with real photons. Although they are all actual prompt photons, any possible bias due to the different event topologies of the signal and backgrounds must be investigated. This is performed by comparing the isolation distributions of the prompt photons from the signal, W+jets+γ and Z+jets+γ processes. No remarkable disagreement was observed within the statistical error bands and therefore no systematic uncertainties is assigned for the possible bias mentioned in the beginning.

Chapter 9

Theoretical Prediction

Theoretical prediction for $t\bar{t}$ pair production with an additional photon n the final state with QCD corrections, i.e. at NLO($\mathcal{O}(\alpha_s^3)$), can be calculated at *different levels*. For instance, the NLO prediction by [90], was performed in the approximation of stable top-quarks. The cross-section for the same process was the extended in [**me**] by allowing the top-quarks to decay and including photon radiation in both the production and the decay processes of the $t\bar{t}$ pair. The result of the experimental measurement is compared to the prediction in the latter reference.

This prediction treats the top-quarks in the narrow width approximation by retaining spin correlations of final-state particles. The cross-section is predicted for the $l + jets$ decay channel of the $t\bar{t}$ pair. For the hadronic decays of the W-bosons, only the first two quark generations are considered with the quarks being massless. For the leptonic decays of W-bosons, only decays into e and μ flavours are considered.

Furthermore, the W-bosons are treated being on their mass-shells and no QCD radiative corrections to hadronic decays of W-bosons are considered. On the other hand, photons are allowed to radiate off any charged particles in the production and decay chain including the decay products of W-bosons. While the result presented in [91] is calculated for the collision of energy of 14 TeV, the authors provided a result dedicated to a collision energy of 8 TeV. For this calculation, the NLO PDF set CTEQ10 and the fine structure constant of 1/137 is used. The renormalisation and factorisation scales (QCD scales) are set to m_t and the strong coupling constant is evaluated using one- and two-loop running with five massless flavours.

9.1 Comparison of theoretical prediction to MC-based prediction

The $t\bar{t}\gamma$ cross-section is calculated at LO using MadGraph [71] considering the same generation phase space, as for the theoretical prediction. The lepton is required to have $p_T > 15$ GeV and presence of at least four jets is required, each of which being separated from photons by $\Delta R(\gamma, \text{jet}) > 0.2$. The jets are reconstructed with the anti-k_T algorithm (R=0.4) and required to have $p_T >$ 10 GeV and $\mid \eta \mid < 5$. The final state photon is required to have $p_T > 10$ GeV, $|\eta| < 5$, and $\Delta R(\gamma, l) > 0.5$.

The cross-section at LO calculated with MadGraph after applying the phase space

cuts for the theoretical calculation can be expressed with the following formula:

$$\sigma_{t\bar{t}\gamma}^{LO,cuts} = \frac{N_{t\bar{t}\gamma}^{gen,cuts}}{N_{t\bar{t}\gamma}^{gen,all}} \times \sigma_{t\bar{t}\gamma}^{LO} \tag{9.1}$$

where $N_{t\bar{t}\gamma}^{gen,cuts}$ is the total number of events at generator level after applying the phase space cuts used in the theoretical calculation, $N_{t\bar{t}\gamma}^{gen,all}$ is the total number of generated single-lepton events in the $t\bar{t}\gamma$ MC sample and finally $\sigma_{t\bar{t}\gamma}^{LO}$ is the LO $l + jets$ cross-section of the generated $t\bar{t}\gamma$ sample.

The theoretical predictions and the calculated total cross-sections using MadGraph with different selection of renormalisation and factorisation scales are listed table 9.1.

Table 9.1.: The LO cross-section comparison of predictions from theory calculations to those obtained from MadGraph calculations in the single lepton (e or μ) channel at scales of m_t and $2m_t$.

cross-section [fb]	scale m_t	scale $2m_t$
Theory	606.36	458.55
MadGraph	617.48	465.98

9.2 Next-to-leading order k-factor

The NLO k-factor is defined as the ratio of the cross-section at NLO (i.e. theory prediction) to the cross-section at LO calculated with MadGraph in the same phase space used for the calculation of theoretical prediction. As mentioned above, the QCD scales used in the calculation of NLO prediction are set to m_t, while in the calculation of LO madGraph cross-section the scales are set to $2m_t$. In figure 9.1, the k-factor is illustrated as a function of photon transverse momentum and pseudo-rapidity. In addition, two variations of the k-factors are shown where the QCD scales are varied up and down by factor 2 in the calculation of cross-section at NLO. An average k-factor is then calculated by weighting the binned k-factor shown as a function of photon transverse momentum which can be formulated as follows:

$$\bar{k} = \frac{\sum_i [k_i \times N_i^{gen}]}{\sum_i N_i^{gen}} \tag{9.2}$$

where k_i is the k-factor in the i-th p_T bin and N_i^{gen} is the number of photons in the i-th p_T bin.

The average k-factor is calculated to be $1.90 \pm 0.25 \pm 0.12$ where the first uncertainty is originated from the variation of QCD scales and the second is from the variation of PDF set used.

9.2.1 Next-to-leading order cross-section

The NLO predictions, which will be compared with the experimental results, are evaluated by applying the k_i-factors to the differential p_T and η bins bin by bin. The cross-sections at NLO are calculated to be 77.6 ± 12.8 fb and 73.8 ± 12.1 fb for the electron and muon

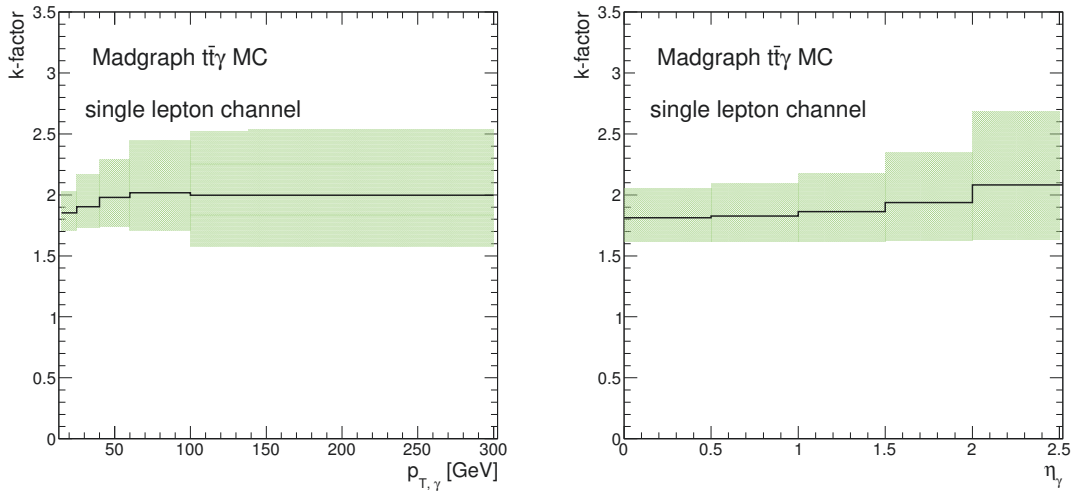

Figure 9.1.: The k-factor distributions as a function of the selected photon p_T (left) and η (right). The shaded area evaluated by varying the NLO scale variation by a factor of two around the central value (m_t) used for the NLO calculations. Photons are selected according to the same cuts applied in the theory calculations in the single lepton channel [92].

channels, respectively. The calculated predictions of differential cross-sections at NLO are listed in tables 9.2 and 9.3.

Table 9.2.: Predictions of the photon p_T differential cross-sections in the electron and muon channels.

cross-section (fb)	{15, 25)	{25, 40)	{40, 60)	{60, 100)	{100, 300}
e + jets	27.9 ± 2.7	20.1 ± 2.8	12.4 ± 1.8	9.7 ± 1.5	6.8 ± 1.4
μ + jets	26.7 ± 2.6	19.3 ± 2.6	11.7 ± 1.7	9.1 ± 1.4	6.4 ± 1.3

Table 9.3.: Predictions of the photon η differential cross-sections in the electron and muon channels.

cross-section (fb)	0{0.0, 0.25)	{0.25, 0.55)	{0.55, 0.90)	{0.90, 1.37	{1.37, 2.37)
e + jets	12.6 ± 1.7	14.7 ± 2.2	15.3 ± 2.6	16.7 ± 3.3	18.6 ± 5.0
μ + jets	12.1 ± 1.7	14.0 ± 2.1	14.5 ± 2.4	15.9 ± 3.2	17.8 ± 4.8

Chapter 10

Results

The measurements of both inclusive and differential cross-sections are performed in a fiducial phase space, of which the definition is given in section 6.6, by performing the maximum likelihood template fit method modelled in section 6.3.1.

The fit is performed by following a so-called *combined fit* manner. In this manner, the combination refers to the combination of the electron and muon channels in terms of the correlations of the systematic uncertainties. Namely, the fit is performed by taking the correlations of the uncertainties of the two channels into account, but without using data from the other channel. In the statistical modelling language, the nuisance parameters assigned to each systematic uncertainty is shared between the two channels where the data distributions are completely uncorrelated. This manner yields two separate cross-sections, $\sigma_{t\bar{t}\gamma}^{e,incl}$ and $\sigma_{t\bar{t}\gamma}^{\mu,incl}$.

10.1 Inclusive measurement

For the inclusive cross-section measurement, the template fit yields 404.6 ± 48.0 and 676.4 ± 60.0 of signal events in the electron and muon channels respectively. The post-fit yields for signal events and all backgrounds are listed in table 10.1.

Table 10.1.: Post-fit event yields for the signal and backgrounds for the inclusive measurement.

Process	$t\bar{t}\gamma$	Hadronic Fake	$e \to \gamma$ Fake	$W\gamma$ + Jets	$Z\gamma$ + Jets	Single Top + γ	QCD + γ	Diboson + γ	Total (Sig+Bkgs)	Data
e + jets	404.6 ± 48.0	415.9 ± 23.3	312.1 ± 20.4	65.2 ± 14.8	35.2 ± 11.4	13.0 ± 5.6	7.7 ± 16.2	2.2 ± 1.0	1255.9 ± 36.4	1256
μ + jets	676.4 ± 60.0	592.3 ± 31.0	382.3 ± 22.2	97.2 ± 15.1	38.1 ± 11.9	19.1 ± 7.4	8.3 ± 25.5	1.8 ± 0.8	1815.6 ± 43.8	1816

The total number of signal and background events yielded from the template fit is in excellent agreement with the number of data candidates in both channels. The post-fit distributions of the discriminator variable of the fit, p_T^{cone20} isolation of the photon, are presented in figure 10.1. The fit results of the cross-sections for the electron and muon channels are 71.4 ± 13.0 fb and 70.0 ± 9.8 fb which are in agreement within the uncertainties with the SM prediction. A comparison of the experimental and theoretical results are presented below in table 10.2. The model used to perform the template fit is tested by performing the same fit using computer generated Asimov data and it is found to be consistent with the real data. The post-fit photon isolation distribution using Asimov data is shown in figure 10.2. The confidence intervals for the two parameters of interest

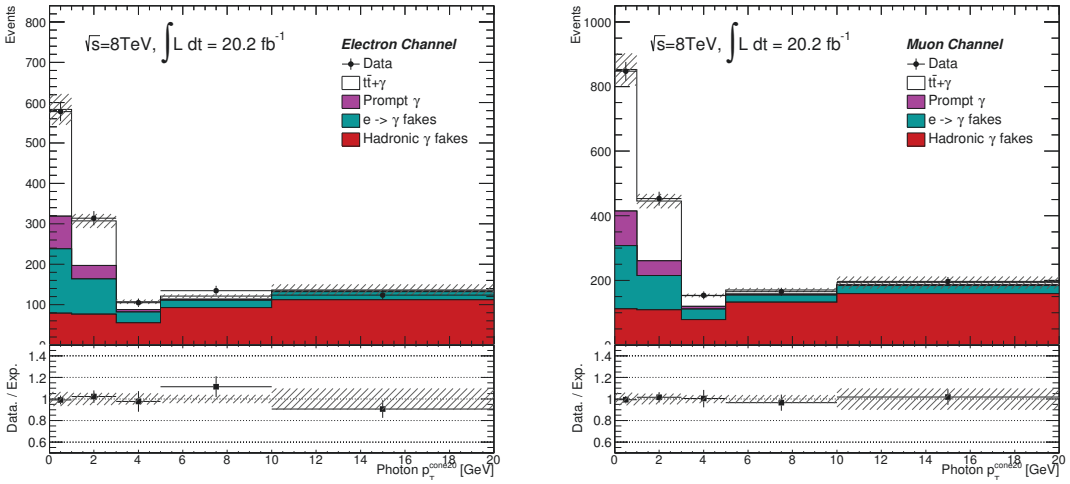

Figure 10.1.: Post-fit isolation distributions for electron and muon channels for the inclusive measurement.

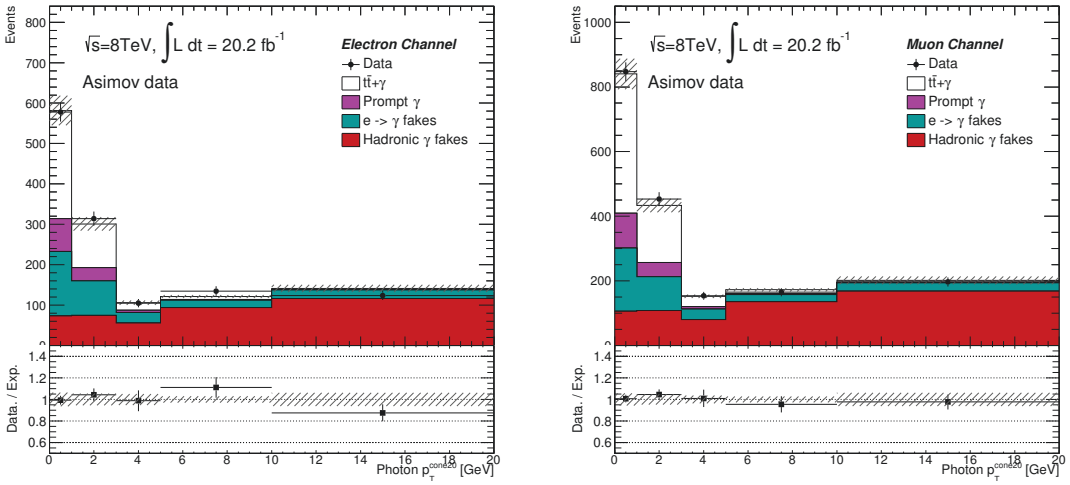

Figure 10.2.: Post-fit isolation distributions of the fit performed using Asimov data for electron and muon channels for the inclusive measurement.

Table 10.2.: Comparison of the measured inclusive cross-sections in the electron and muon channels. The statistical and systematical uncertainties are presented separately for the measured cross-section.

Channel	Theory [fb]	Measurement [fb]
e + jets	77.6 ± 12.8	71.4 ± 6.0(stat.) ± 11.5(sys.)
μ + jets	73.8 ± 12.1	70.0 ± 4.2(stat.) ± 8.85(sys.)

in the inclusive measurement, $\sigma_{t\bar{t}\gamma}^{e,incl}$ and $\sigma_{t\bar{t}\gamma}^{\mu,incl}$, are calculated via the profile likelihood ratio formulated in equation 6.10. The ratio is evaluated within the RooFit/RooStats framework. The upper and lower boundaries of the 68% confidence intervals on the cross-sections are determined. The profile likelihood ratio scans for the inclusive cross-section measurement in electron and muon channels are shown in figure 10.3. The effect of each

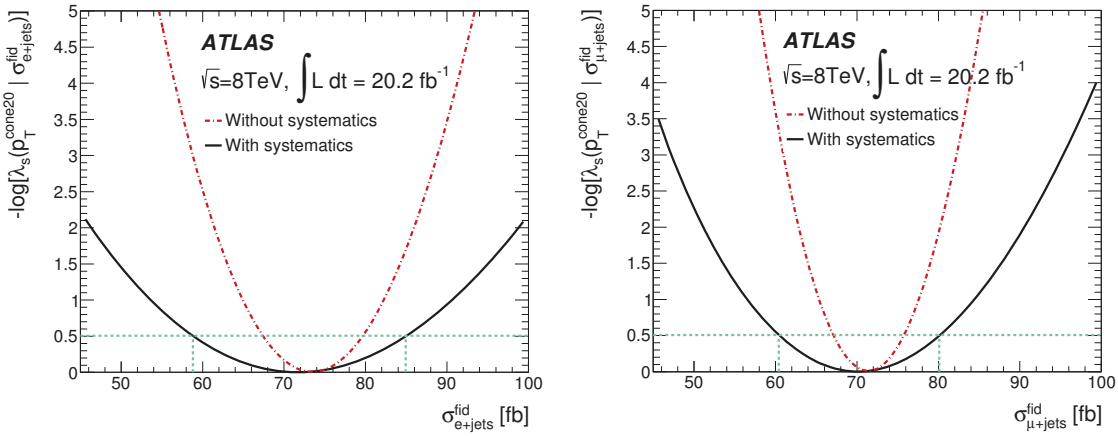

Figure 10.3.: Profile likelihood scans for the electron and muon channels.

systematic is studied by performing a naive approach, where the template fit is performed by incorporating only one systematic uncertainty at a time. The breakdown is performed for all systematics and a set of leading systematics are presented in tables 10.3 and 10.4.

10.2 Differential measurements

The post-fit event yields for each process and data are given in tables10.5 and 10.6 for the p_T and η bins respectively. The yields are in good agreement with data for both measurements. The post-fit p_T^{cone20} isolation distributions are given in figures 10.4, 10.5, 10.6 and 10.7. The comparisons of the differential cross-sections with the theoretical predictions are given tables 10.7 and 10.8 with the corresponding graphical presentation in figure 10.8.

Table 10.3.: Systematics breakdown for the electron channel by performing a naive add- and remove method. Only a set of leading systematics are presented. The effects of the systematics on the cross-section are presented in per cent.

Systematics	Uncertainty (%))	Systematics	Uncertainty (%))
SysFitFuncEGammaFake	6.5	SysJESEtaS	1.0
ShapeSysHadronFake	6.1	SysJESEtaM	0.8
SysTheoWGammaJets	5.8	SysPhES	0.7
SysTheoZGammaJets	4.2	SysJERNP2	0.7
SysJESMod1	3.5	ShapeSysContEGammaFake	0.7
SysJESRho	2.6	SysStatSTGammaEl	0.7
SysLepIDEl	2.6	SysJESMix2	0.6
SysISRFSR	2.5	SysJESMix1	0.5
SysLumi	2.1	SysStatEffEl	0.5
SysContEGammaFake	2.4	SysMETR	0.5
SysJESFlavR	2.3	SysStatZGammaJetsEl	0.5
SysPhID	1.7	SysJERNP5	0.5
SysTheoSTGamma	1.6	SysJESbJES	0.5
SysPS	1.6	SysMisTag12	0.4
ShapeSysMETEGammaFake	1.6	ShapeSysPtOrderEGammaFake	0.4
SysJESStat1	1.5	SysJERNP3	0.4
SysJESFlavC	1.3	SysTheoDiboson	0.3
SysStatEGammaFakeEl	1.2	SysJERNP4	0.3
SysLepTrigEl	1.2	ShapeSysStatHadronFakeBin1	0.3
SysStatWGammaJetsEl	1.1	SysJERNP0	0.2
SysJESNPVOff	1.0	SysMETS	0.2

Table 10.4.: Systematics breakdown for the muon channel by performing a naive add-and remove method. Only a set of leading systematics are presented.The effects of the systematics on the cross-section are presented in per cent.

Systematics	Uncertainty (%))	Systematics	Uncertainty (%))
ShapeSysHadronFake	5.2	SysTheoSTGamma	1.4
SysFitFuncEGammaFake	4.1	SysPhID	1.2
SysTheoWGammaJets	3.5	SysScale	1.1
SysJESMod1	3.1	SysStatWGammaJetsMu	0.9
SysTheoZGammaJets	2.8	SysJESNPVOff	0.8
SysJESRho	2.3	SysJESEtaS	0.8
SysLumi	2.1	ShapeSysContEGammaFake	0.5
SysLepTrigMu	1.9	SysJESbJES	0.5
SysContEGammaFake	1.8	SysJESMix1	0.5
SysJESFlavR	1.8	SysLepIDMu	0.5
SysPS	1.7	SysStatSTGammaMu	0.5
SysISRFSR	1.6	SysJERNP0	0.4
SysJESStat1	1.3	ShapeSysPtOrderEGammaFake	0.3
ShapeSysMETEGammaFake	1.2	SysMisTag12	0.3
SysJERNP2	0.8	SysStatZGammaJetsMu	0.3
SysJESFlavC	0.8	SysJERNP1	0.2
SysPhES	0.7	SysMETR	0.2
SysJESEtaM	0.7	SysJERNP5	0.1
SysJESMix2	0.6	SysMETS	0.1
SysJERNP3	0.6	SysJERNP4	0.1

Table 10.5.: Post-fit event yields for the signal and backgrounds in the p_T differential measurement.

Process		$t\bar{t}\gamma$	Hadron Fake	$e \to \gamma$ Fake	$W\gamma$ + Jets	$Z\gamma$ + Jets	Single Top + γ	QCD + γ	Diboson + γ	Data
e + jets	$15 \leq p_T < 25$ GeV	95.2 ± 22.1	181.5 ± 10.9	101.9 ± 17.6	18.0 ± 4.5	10.0 ± 3.6	1.5 ± 0.5	2.0 ± 2.0	0.5 ± 0.2	410
	$25 \leq p_T < 40$ GeV	123.1 ± 14.7	88.1 ± 7.8	79.3 ± 2.0	15.0 ± 3.7	9.0 ± 3.1	2.5 ± 1.3	2.0 ± 2.1	0.5 ± 0.2	319
	$40 \leq p_T < 60$ GeV	95.2 ± 14.1	54.0 ± 6.0	46.2 ± 8.1	9.1 ± 2.3	7.1 ± 2.7	5.6 ± 2.4	1.0 ± 1.0	0.5 ± 0.3	217
	$60 \leq p_T < 100$ GeV	72.9 ± 14.0	53.6 ± 7.6	36.7 ± 9.9	9.0 ± 2.3	6.0 ± 2.1	4.0 ± 1.9	1.5 ± 1.3	0.5 ± 0.3	178
	$100 \leq p_T < 300$ GeV	57.4 ± 9.6	36.2 ± 5.6	19.5 ± 4.8	9.1 ± 2.2	3.0 ± 1.1	1.0 ± 0.7	0.5 ± 0.2	0.5 ± 0.3	126
μ + jets	$15 \leq p_T < 25$ GeV	199.5 ± 26.9	155.4 ± 12.3	150.3 ± 13.6	27.0 ± 4.7	13.0 ± 4.4	5.5 ± 2.3	5.5 ± 3.4	0.5 ± 0.2	556
	$25 \leq p_T < 40$ GeV	201.0 ± 16.8	135.4 ± 9.0	91.1 ± 2.7	20.0 ± 3.5	12.0 ± 3.8	4.0 ± 1.7	0.0 ± 0.0	0.5 ± 0.2	464
	$40 \leq p_T < 60$ GeV	152.0 ± 16.3	139.9 ± 9.0	50.1 ± 8.3	18.0 ± 3.1	5.0 ± 1.7	4.0 ± 1.5	2.9 ± 3.3	0.5 ± 0.3	372
	$60 \leq p_T < 100$ GeV	116.5 ± 15.1	63.9 ± 6.6	40.4 ± 10.4	13.1 ± 2.4	4.0 ± 1.4	5.0 ± 2.0	0.0 ± 0.0	0.5 ± 0.2	242
	$100 \leq p_T < 300$ GeV	109.0 ± 11.0	36.3 ± 5.6	19.4 ± 4.9	12.0 ± 2.1	1.5 ± 1.1	0.0 ± 0.0	0.0 ± 0.0	0.5 ± 0.4	172

Table 10.6.: Post-fit event yields for the signal and backgrounds in the η differential measurement.

Process		$t\bar{t}\gamma$	Hadron Fake	$e \to \gamma$ Fake	$W\gamma$ + Jets	$Z\gamma$ + Jets	Single Top + γ	QCD + γ	Diboson + γ	Data
e + jets	$0 \leq \lvert\eta\rvert < 0.25$	102.8 ± 17.4	58.8 ± 8.6	40.3 ± 4.4	9.0 ± 2.3	5.0 ± 1.9	1.5 ± 0.9	2.5 ± 1.9	0.5 ± 0.3	216
	$0.25 \leq \lvert\eta\rvert < 0.55$	115.8 ± 17.5	55.6 ± 7.1	51.6 ± 5.6	11.0 ± 2.7	4.0 ± 1.9	2.5 ± 1.4	0.0 ± 0.0	0.5 ± 0.3	236
	$0.55 \leq \lvert\eta\rvert < 0.90$	65.4 ± 15.7	98.8 ± 9.3	57.0 ± 7.9	12.0 ± 3.0	7.0 ± 2.4	0.5 ± 0.4	1.5 ± 1.4	0.5 ± 0.3	242
	$0.90 \leq \lvert\eta\rvert < 1.37$	53.7 ± 17.2	104.1 ± 9.5	65.1 ± 8.8	13.0 ± 3.2	8.0 ± 2.7	5.0 ± 2.3	2.5 ± 2.3	0.5 ± 0.2	250
	$1.37 \leq \lvert\eta\rvert < 2.37$	65.6 ± 17.5	127.5 ± 9.8	91.7 ± 3.6	17.9 ± 4.6	8.9 ± 3.9	4.0 ± 1.9	2.5 ± 2.8	0.5 ± 0.3	312
μ + jets	$0 \leq \lvert\eta\rvert < 0.25$	146.4 ± 17.5	66.5 ± 7.2	51.7 ± 5.9	9.0 ± 1.8	4.0 ± 1.4	2.0 ± 0.9	1.5 ± 1.9	0.5 ± 0.3	281
	$0.25 \leq \lvert\eta\rvert < 0.55$	148.9 ± 18.5	77.8 ± 8.1	63.0 ± 7.1	17.0 ± 3.1	6.0 ± 2.1	2.0 ± 1.0	1.5 ± 2.2	0.5 ± 0.3	316
	$0.55 \leq \lvert\eta\rvert < 0.90$	134.9 ± 19.6	99.7 ± 9.5	74.9 ± 8.4	17.9 ± 3.2	8.0 ± 2.7	1.0 ± 0.5	0.0 ± 0.0	0.5 ± 0.3	336
	$0.90 \leq \lvert\eta\rvert < 1.37$	150.0 ± 22.2	151.3 ± 11.4	78.1 ± 9.5	22.0 ± 4.0	8.0 ± 2.7	3.0 ± 1.3	1.0 ± 2.3	0.5 ± 0.2	413
	$1.37 \leq \lvert\eta\rvert < 2.37$	105.5 ± nan	214.1 ± nan	105.6 ± 3.3	29.0 ± 5.2	9.0 ± 3.2	8.0 ± 3.2	1.0 ± 1.8	0.5 ± 0.2	470

Table 10.7.: Comparison of p_T differential cross-section measurement with the corresponding theoretical predictions. The first error on the observation values are statistical errors where the second ones is systematic. The unit is in fb.

p_T bins [GeV]		$15 \leq p_T < 25$	$25 \leq p_T < 40$	$40 \leq p_T < 60$	$60 \leq p_T < 100$	$100 \leq p_T < 300$
e + jets	Theory	27.9 ± 2.7	20.1 ± 2.8	12.4 ± 1.8	9.7 ± 1.5	6.8 ± 1.4
	Observation	20.7 ± 4.1 ± 3.9	21.4 ± 3.3 ± 2.3	13.4 ± 2.2 ± 2.6	8.9 ± 1.7 ± 2.9	6.7 ± 1.4± 1.3
μ + jets	Theory	26.7 ± 2.6	19.3 ± 2.6	11.7 ± 1.7	9.1 ± 1.4	6.4 ± 1.3
	Observation	24.2 ± 3.1 ± 2.9	19.4 ± 2.1 ± 1.7	11.8 ± 1.5 ± 1.6	8.5 ± 1.2 ± 1.9	7.7 ± 1.0 ± 0.8

Table 10.8.: Comparison of η differential cross-section measurement with the corresponding theoretical predictions. The first error on the observation values are statistical errors where the second ones is systematic. The unit is in fb.

$\lvert\eta\rvert$ bins		$0.0 \leq \lvert\eta\rvert < 0.25$	$0.25 \leq \lvert\eta\rvert < 0.55$	$0.55 \leq \lvert\eta\rvert < 0.90$	$0.90 \leq \lvert\eta\rvert < 1.37$	$1.37 \leq \lvert\eta\rvert < 2.37$
e + jets	Theory	12.6 ± 1.7	14.7 ± 2.2	15.3 ± 2.6	16.7 ± 3.3	18.6 ± 5.0
	Observation	16.1 ± 2.5 ± 2.5	18.4 ± 2.5 ± 2.6	11.0 ± 2.5 ± 2.6	9.7 ± 2.8 ± 3.2	15.3 ± 4.0(stat.) ± 3.5
μ + jets	Theory	12.1 ± 1.7	14.0 ± 2.1	14.5 ± 2.4	15.9 ± 3.2	17.8 ± 4.8
	Observation	14.0 ± 1.6 ± 1.5	13.9 ± 1.7 ± 1.5	13.3 ± 1.8 ± 2.0	15.5 ± 2.0 ± 2.2	13.9 ± 2.4 ± 2.1

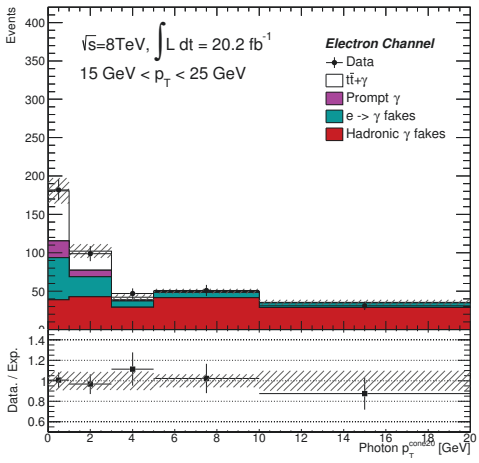

(a)

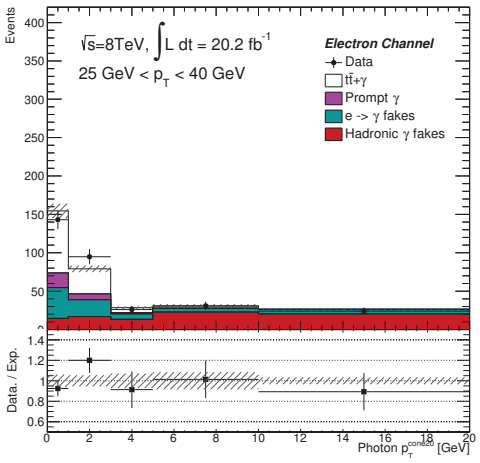

(b)

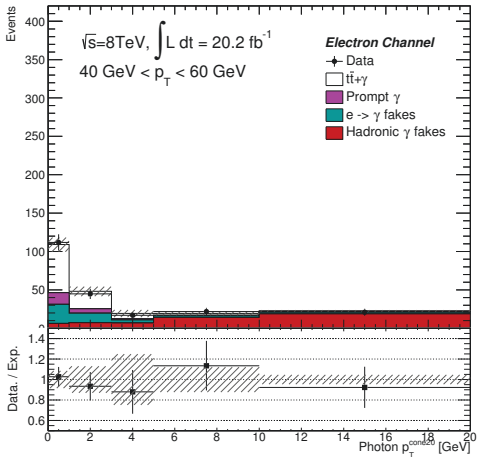

(c)

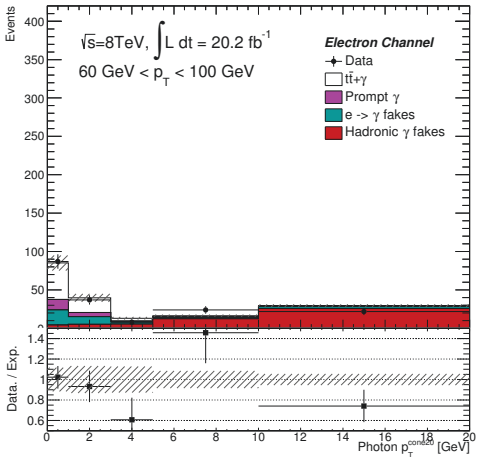

(d)

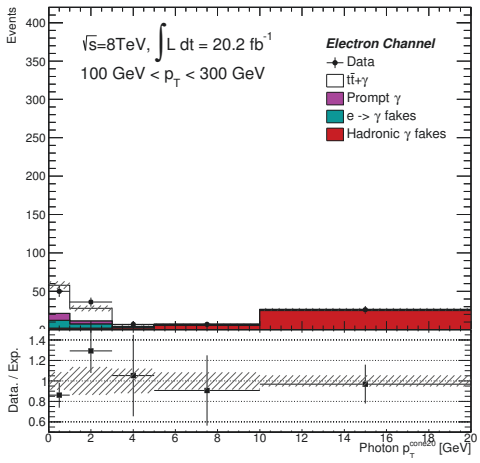

(e)

Figure 10.4.: Post-fit photon isolation distributions for the p_T differential cross-section measurement for the electron channel.

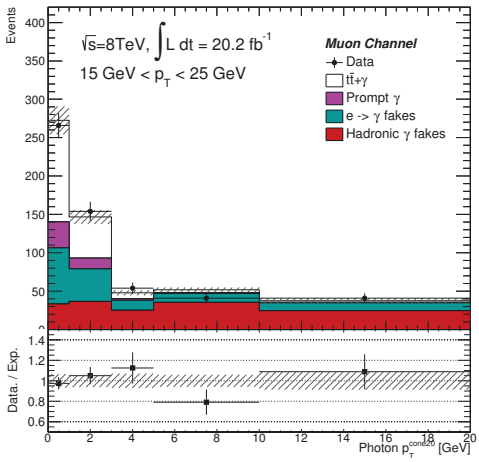

(a)

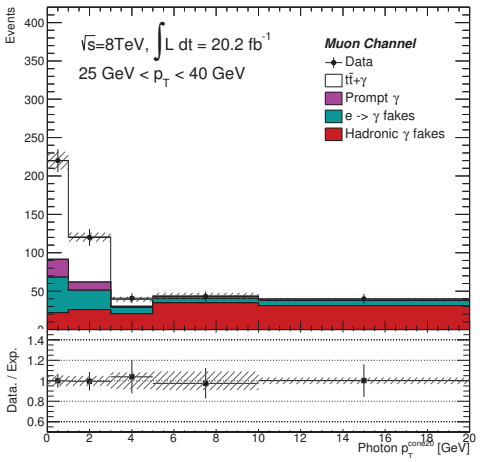

(b)

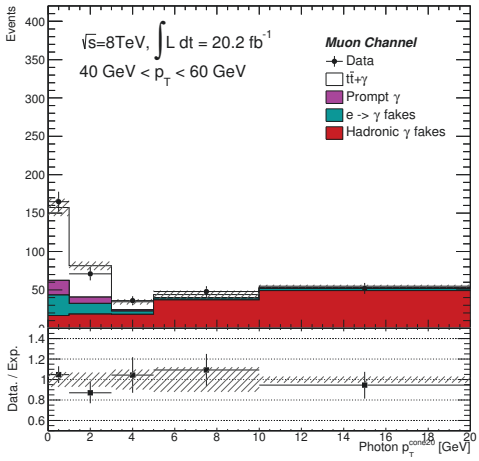

(c)

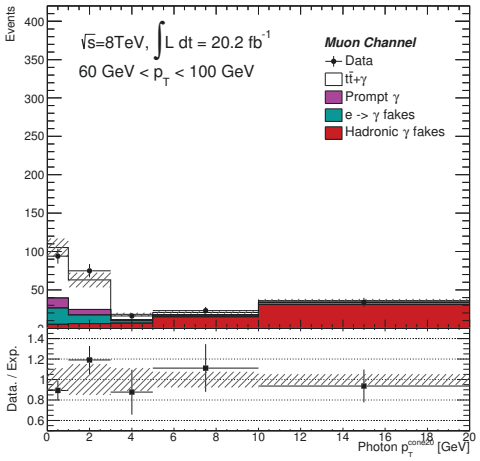

(d)

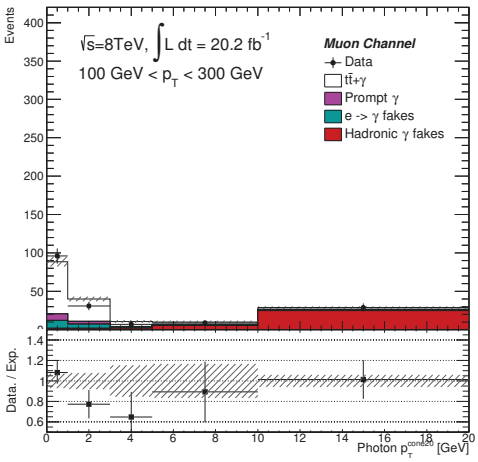

(e)

Figure 10.5.: Post-fit photon isolation distributions for the p_T differential cross-section measurement for the muon channel.

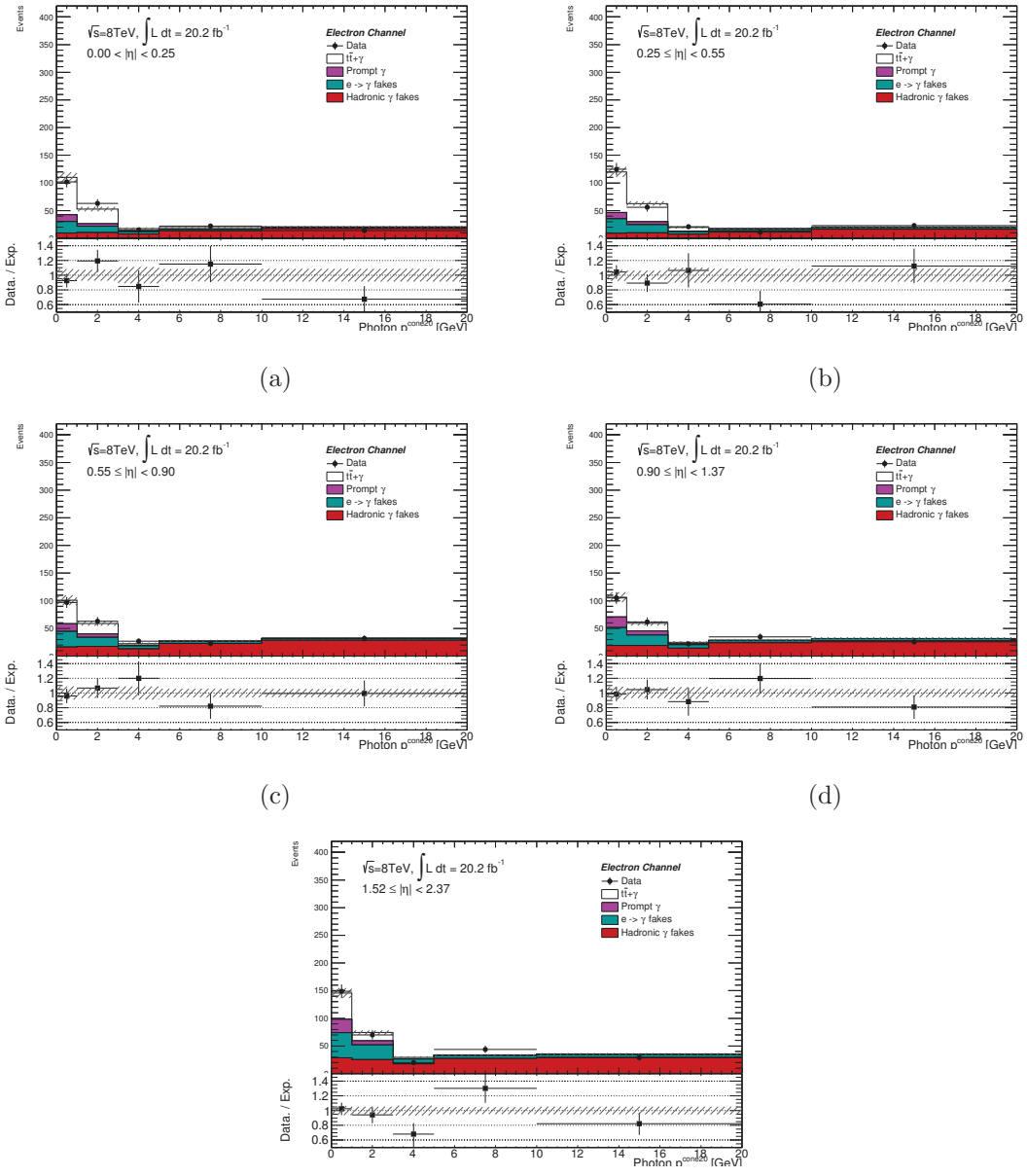

Figure 10.6.: Post-fit photon isolation distributions for the η differential cross-section measurement for the electron channel.

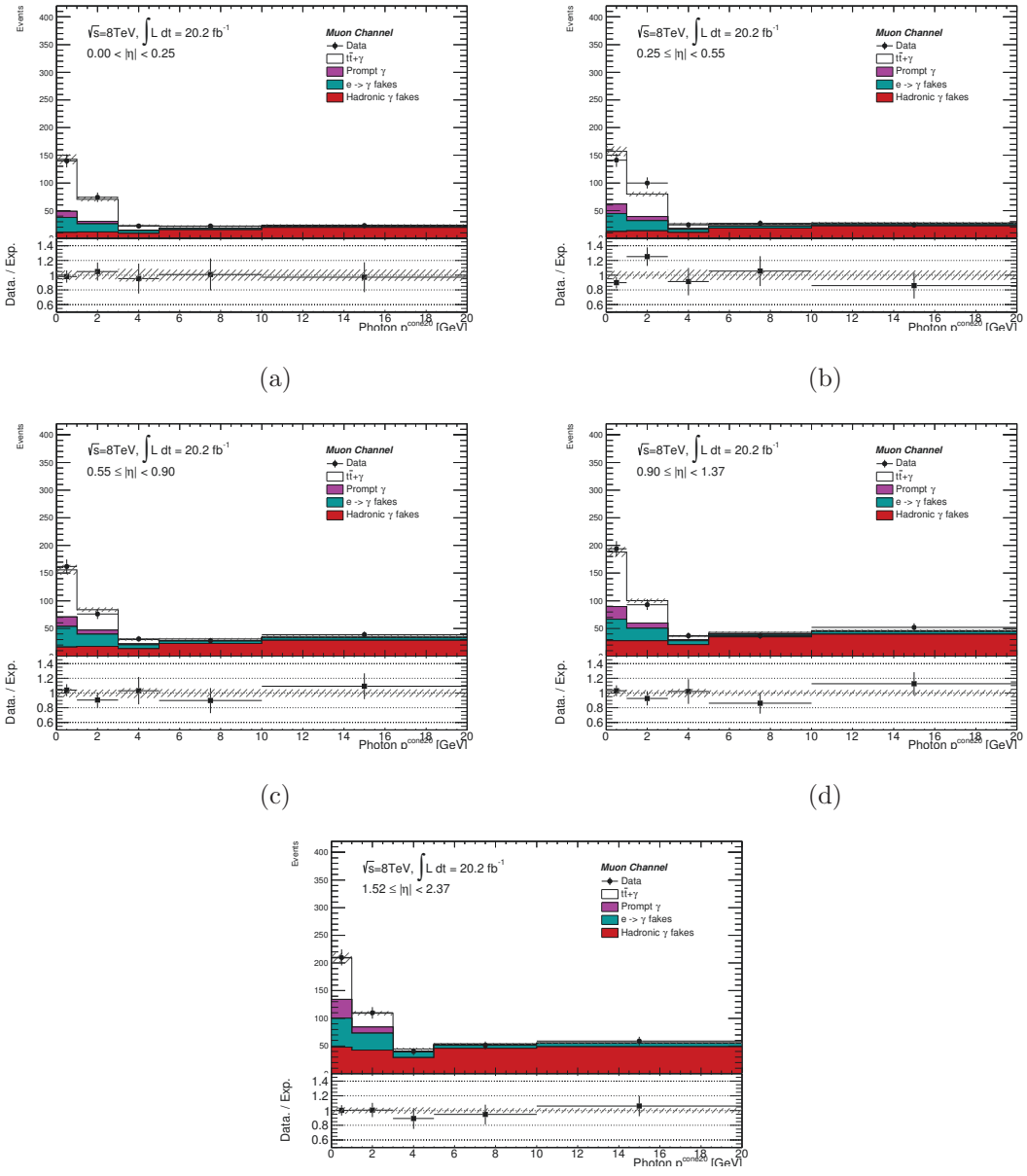

Figure 10.7.: Post-fit photon isolation distributions for the η differential cross-section measurement for the muon channel.

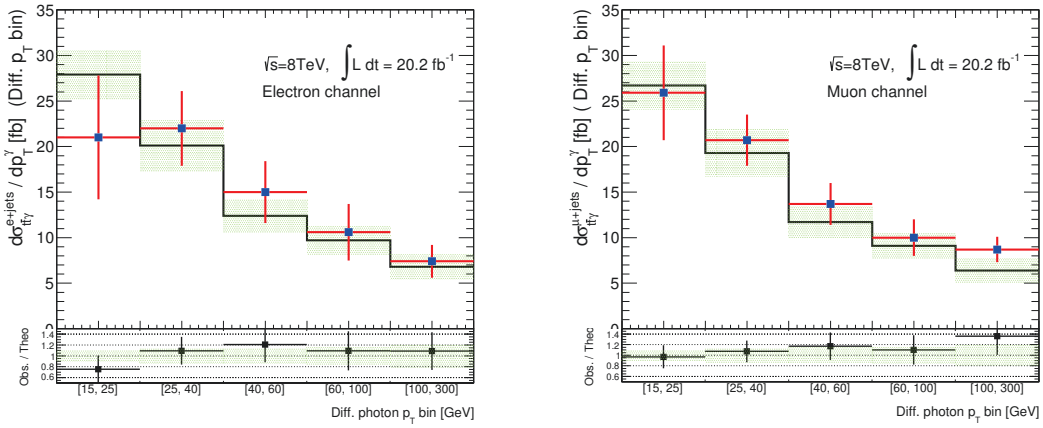

(a) (b)

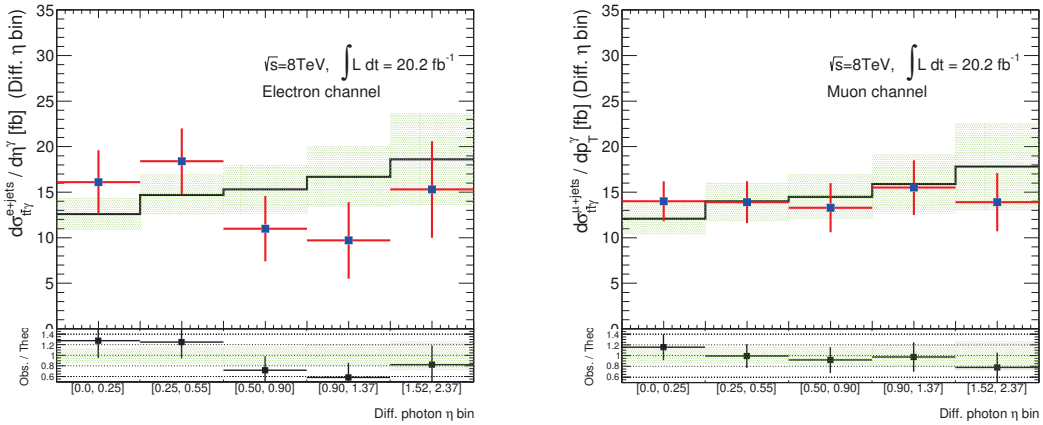

(c) (d)

Figure 10.8.: Post-fit photon isolation distributions for the p_T differential cross-section measurement for the electron channel.

Chapter 11

Summary and outlook

The measurement of the $t\bar{t}\gamma$ cross section is a first step for the understanding of the $t\gamma$ vertex and for testing the SM.

An inclusive and differential measurements of the $t\bar{t}\gamma$ process are presented. The measurements are performed in e+jets and μ+jets decay channels of the $t\bar{t}$ pair and within a certain fiducial space. The measurement analysed the full dataset recorded by the ATLAS detector during 2012 at a center-of-mass energy of 8 TeV.

Differential measurement, in general, is a sort of tool that provides a closer look to a so-called *region-of-interest* which is believed to be a possible window to new physics phenomena. The differential measurements, in this thesis, are performed as a function of photon transverse momentum and photon pseudo-rapidity since the objective of the thesis is $t\gamma$ vertex and since possible deviations of this vertex from the SM predictions would reveal them in the kinematic distributions of the photon.

The signal selection is optimised to select events enriched with $t\bar{t}\gamma$ events where photons are radiated off the top-quarks. Total number of $t\bar{t}\gamma$ candidates in the full 2012 dataset is found to be 3072, where 1256 of the total candidates are in electron channel and 1816 in the muon channel. In order to evaluate the number of signal and background events among these data candidates, various data driven and MC-based methods are developed. Modelling of the template that represents the signal events in the fit is performed using MC simulation, since a statistically satisfying prompt photon sample with the signal event topology is not possible to extract from data. Backgrounds with photons faked by hadrons and by photons from hadrons, and backgrounds with photons fakes by electrons are estimated from data. Backgrounds with prompt photons having minor contributions are estimated using MC simulations while W+jets+γ and multi-jet+γ backgrounds estimated from data by use of template fitting.

The fit result of the inclusive cross section measured for photons with a p_T >15 GeV and $|\eta|$ <2.37 reads 71.4 $\pm$ 13.0 fb for the $e$channel and 70.0 $\pm$ 9.8 fb for the μ+jets channel. The results are in agreement with the NLO SM predictions. The dominating systematic uncertainty on the cross section is the modelling shape systematics assigned to the template for the hadronic fake photons. The following dominating systematic uncertainty is the systematics assigned to the variation of the fit function used for the estimation of $e \to \gamma$ fake rates. The results for both p_T and η differential measurements are in agreement with the SM predictions within the uncertainties which can be interpreted as indication of no evidence for new physics in the $t\gamma$ vertex with the collisions at 8 TeV and the analysed statistics.

The chances for observing possible deviations from the SM prediction will increase

with the higher collision energy and higher statistics aimed in the future. These deviations can be observed by adopting a model-independent effective field theory approach in which any new model can be modelled by adding new higher-dimensional operators to the SM Lagrangian [93].

Appendices

Appendix A

Monte Carlo samples

A.1 Baseline samples

DSID	Description	Matrix Element	Parton Shower	σ [pb]	k-factor
117980	$t\bar{t}\gamma$ (scale m_t)	MADGRAPH	PYTHIA	1.5779	
117478	$t\bar{t}\gamma$ (scale $2m_t$)	MADGRAPH	PYTHIA	1.1907	1.9
117981	$t\bar{t}\gamma$ (scale $4m_t$)	MADGRAPH	PYTHIA	0.91973	

Table A.1.: $t\bar{t}\gamma$ samples

DSID	Description	Matrix Element	Parton Shower	σ [pb]	k-factor
110404	$t\bar{t}$	POWHEG	PYTHIA	114.47	1.1996

Table A.2.: $t\bar{t}$ samples

DSID	Description	Matrix Element	Parton Shower	σ [pb]	k-factor
110090	st (t-chan)	POWHEG	PYTHIA	17.520	1.0500
110091	st (t-chan)	POWHEG	PYTHIA	9.3932	1.0616
110140	st(Wt-chan)	POWHEG	PYTHIA	20.461	1.0933

Table A.3.: Single top samples

A.2 Samples for estimation of systematic uncertainties

DSID	Description	Matrix Element	Parton Shower	σ [pb]	k-factor
107100	WW Np0 (lnulnu)	ALPGEN	HERWIG	2.4970	1.2307
07101	WW Np1 (lnulnu)	ALPGEN	HERWIG	1.2491	1.2307
107102	WW Np2 (lnulnu)	ALPGEN	HERWIG	0.59200	1.2307
107103	WW Np3 (lnulnu)	ALPGEN	HERWIG	0.32847	1.2307
107104	WZ Np0 (incl.ll)	ALPGEN	HERWIG	0.80162	1.2785
107105	WZ Np1 (incl.ll)	ALPGEN	HERWIG	0.52407	1.2785
107106	WZ Np2 (incl.ll)	ALPGEN	HERWIG	0.29484	1.2785
107107	WZ Np3 (incl.ll)	ALPGEN	HERWIG	0.18258	1.2785
107108	ZZ Np0 (incl.ll)	ALPGEN	HERWIG	0.60660	1.3718
107109	ZZ Np1 (incl.ll)	ALPGEN	HERWIG	0.28893	1.3718
107110	ZZ Np2 (incl.ll)	ALPGEN	HERWIG	0.11853	1.3718
107111	ZZ Np3 (incl.ll)	ALPGEN	HERWIG	0.056223	1.3718

Table A.4.: Diboson samples

DSID	Description	Generator	σ [pb]	k-factor
126856	$\tau\nu\gamma$	SHERPA	162.96	1.
126739	$e\nu\gamma$	SHERPA	162.88	1.
126742	$\nu\mu\gamma$	SHERPA	162.89	1.

Table A.5.: $W + jet + \gamma$ samples

DSID	Description	Generator	σ [pb]	k-factor
126854	$\tau\tau\gamma$	SHERPA	32.317	1.
145161	$ee\gamma$	SHERPA	32.326	1.
145162	$\mu\mu\gamma$	SHERPA	32.326	1.

Table A.6.: $Z + jet + \gamma$ samples

DSID	Description	Generator	σ [pb]	k-factor
167740	$We\nu$ (BFilter)	SHERPA	140.34	1.1
167741	$We\nu$ (CJetFilterBVeto)	SHERPA	537.84	1.1
167742	$We\nu$ (CJetVetoBVeto)	SHERPA	10295.0	1.1
167743	$W\mu\nu$ (BFilter)	SHERPA	140.39	1.1
167744	$W\mu\nu$ (CJetFilterBVeto)	SHERPA	466.47	1.1
167745	$W\mu\nu$ (CJetVetoBVeto)	SHERPA	10368.0	1.1
167746	$W\tau\nu$ (BFilter)	SHERPA	140.34	1.1
167747	$W\tau\nu$ (CJetFilterBVeto)	SHERPA	506.45	1.1
167748	$W\tau\nu$ (CJetVetoBVeto)	SHERPA	10327.0	1.1

Table A.7.: $W + jet$ samples

DSID	Description	Generator	σ [pb]	k-factor
167749	Zee	SHERPA	31.046	1.12
167750	Zee	SHERPA	314.26	1.12
167751	Zee	SHERPA	764.41	1.12
167752	$Z\mu\mu$	SHERPA	31.036	1.12
167753	$Z\mu\mu$	SHERPA	314.80	1.12
167754	$Z\mu\mu$	SHERPA	764.48	1.12
167755	$Z\tau\tau$	SHERPA	31.008	1.12
167756	$Z\tau\tau$	SHERPA	314.49	1.12
167757	$Z\tau\tau$	SHERPA	764.57	1.12
185835	$Z\nu\nu$	SHERPA		

Table A.8.: $Z + jet$ samples

Bibliography

[1] Sir Karl Raimund Popper. *The Open Society and Its Enemies, Volume II. The High Tide of Prophecy: Hegel, Marx, and the Aftermath.* 1945.

[2] CDF Collaboration. "Observation of Top Quark Production in $\bar{p}p$ Collisions with the Collider Detector at Fermilab". In: *Phys. Rev. Lett.* 74 (14 Apr. 1995), pp. 2626–2631. DOI: 10.1103/PhysRevLett.74.2626. URL: http://link.aps.org/doi/10.1103/PhysRevLett.74.2626.

[3] D0 Collaboration. "Observation of the Top Quark". In: *Phys. Rev. Lett.* 74 (14 Apr. 1995), pp. 2632–2637. DOI: 10.1103/PhysRevLett.74.2632. URL: http://link.aps.org/doi/10.1103/PhysRevLett.74.2632.

[4] M. Kobayashi and T. Maskawa. "CP-Violation in the Renormalizable Theory of Weak Interaction". In: *Progress of theoretical physics* 49 (1973), pp. 652–657.

[5] J. Shu B. Lillie and T.M.P. Tait. "Top compositeness at the Tevatron and LHC". In: *JHEP 087* (2008).

[6] E. Simmons R. S. Chivukula and J. Terning. "A heavy top quark and the Z b anti-b vertex in noncommuting extended technicolor." In: *Phys. Lett. B* 331 (1994).

[7] D. Chang W.F. Changd and E. Ma. "Alternative interpretation of the Tevatron top events". In: *Phys. Rev. D* 59 (091503 1999).

[8] T.P.M Tait D. Choudhury and C.E.M. Wagner. "Beautiful mirrors and precision electroweak data." In: *Phys. Rev. D* 65 (053002 2002).

[9] ATLAS Collaboration. "Measurement of the $t\bar{t}\gamma$ production cross section in proton-proton collisions at $\sqrt{s}$ =8 TeV with the ATLAS detector". In: (). URL: arXiv:1706.03046%20[hep-ex].

[10] *The ATLAS Experiment at the CERN Large Hadron Collider*. 2008 JINST 3 S08003 http://iopscience.iop.org/article/10.1088/1748-0221/3/08/S08003/pdf. 2008.

[11] *Large Hadron Collider Machine*. 2008 JINST 3 S08004 http://iopscience.iop.org/article/10.1088/1748-0221/3/08/S08004/pdf. 2008.

[12] *The Durham HepData Project*. URL: http://hepdata.cedar.ac.uk/pdf/pdf3.html.

[13] Frank-Peter Schilling. "Top Quark Physics at the LHC: A Review of the First Two Years". In: *Int. J. Mod. Phys. A, Vol. 27, No. 17 1230016* (2012).

[14] Matteo Cacciari et al. *Top-pair production at hadron colliders with next-to-next-to-leading logarithmic soft-gluon resummation*. Tech. rep. CERN-PH-TH/2011-277, TTK-11-54. 2011.

[15] Peter Bärnreuther, Michal Czakon, and Alexander Mitov. "Percent Level Precision Physics at the Tevatron: First Genuine NNLO QCD Corrections to $q\bar{q} \to t\bar{t}$". In: *Phys. Rev. Lett.* 109 (13 2012), p. 132001. DOI: 10.1103/PhysRevLett.109.132001. URL: http://link.aps.org/doi/10.1103/PhysRevLett.109.132001.

[16] Michal Czakon and Alexander Mitov. "NNLO corrections to top-pair production at hadron colliders: the all-fermionic scattering channels". In: arXiv:1207.0236 [hep-ph] (2012).

[17] Michal Czakon and Alexander Mitov. "NNLO corrections to top pair production at hadron colliders: the quark-gluon reaction". In: arXiv:1210.6832 [hep-ph] (2012).

[18] Michal Czakon, Paul Fiedler, and Alexander Mitov. "The total top quark pair production cross-section at hadron colliders through $\mathcal{O}(\alpha_S^4)$". In: arXiv:1303.6254 [hep-ph] (2013).

[19] Particle Data Group. "Review of particle physics". In: *J. Phys. G37 (2010) 075021* ().

[20] URL: https://www-d0.fnal.gov/Run2Physics/top/top_public_web_pages/top_feynman_diagrams.html.

[21] ATLAS, CDF, CMS, D0 Collaborations. "First combination of Tevatron and LHC measurements of the top-quark mass". In: (2014). arXiv: 1403.4427v1 [hep-ex].

[22] URL: https://atlas.web.cern.ch/Atlas/GROUPS/PHYSICS/CombinedSummaryPlots/TOP/mtopSummary_TopLHC/mtopSummary_TopLHC.pdf.

[23] A. Sirlin. "Radiativecorrections in the $SU(2)_L \times U(1)$ theory: A simple renormalization framework". In: *Phys. Rev. D* 22 (4 1980).

[24] ALEPH, CDF, D0, DELPHI, L3, OPAL and SLD Collaborations. LEPEWWG, TEVEWWG, SLD, EW and HF groups. "Precision Electroweak Measurements and Constraints on the Standard Model". In: (2010). arXiv: 1012.2367 [hep-ex].

[25] Julian Schwinger. "The Theory of Quantized Fields I. Physical Review." In: *Physical Review 82 1951* ().

[26] ATLAS Collaboration. "Measurement of the mass difference between top and anti-top quarks in pp collisions at $\sqrt{s} = 7$ TeV using the ATLAS detector". In: *Phys. Lett. B728, 363 (2014).* ().

[27] U. Baur, M. Buice, L. H. Orr. "Direct Measurement of the Top Quark Charge at Hadron Colliders". In: *Phys. Rev. D64, 094019* (2001).

[28] D0 Collaboration, V. Abazov et al. "Experimental discrimination between charge 2e/3 top quark and charge 4e/3 exotic quark production scenarios". In: *Phys. Rev. Lett.* 98 (2007).

[29] CDF Collaboration, T. Aaltonen et al. "Exclusion of an Exotic Top Quark with -4/3 Electric Charge Using Soft Lepton Tagging". In: *Phys. Rev. Lett.* 105 (2010).

[30] ATLAS collaboration. "Measurement of the top quark charge in pp collisions at $\sqrt{s}$= 7 TeV with the ATLAS detector". In: *JHEP 11 (2013) 031* ().

[31] N. Cabibbo. "Unitary Symmetry and Leptonic Decays". In: *Phys. Rev. Lett.* 10 (1963), pp. 531–533.

[32] D0 Collaboration, V. Abazov et al. "Precision measurement of the ratio B(t -¿ Wb)/B(t -¿ Wq)". In: *Phys. Rev. Lett. 107 121802* (2007).

[33] ATLAS Collaboration. "Measurement of spin correlation in top - anti-top-quark events and search for top-squark oair production in *pp* collisions at $\sqrt{s}$= 8 TeV using the ATLAS detector". In: *Phys. Rev. Lett. 114 142001* (2015).

[34] A. Czarnecki, J. G. Korner and J. H. Piclum. "Helicity fractions of W bosons from top quark decays at NNLO in QCD". In: *Phys. Rev. D81, 111503* (2010).

[35] ATLAS Collaboration. "Measurement of the w-boson polarisation in $t\bar{t}$ events from *pp* collisions at 8 TeV in the single lepton channel with ATLAS". In: *Eur. Phys. J. C. 77, 264* (2017).

[36] W. Hollik et. el. "Top Dipole Form Factors and Loop-induced CP-violation in Supersymmetry". In: *Nucl. Phys. b551, 3,3407, [Erratum ibid. B557, 407 (1999)]* (1999).

[37] W. Hollik et. el. "Radiative Corrections in the Standard Model and Their Role for Precision Tests of the Electroweak Theory". In: *Fortsch. Phys. 38, 165* (1990).

[38] J. Bernabeu, D. Comelli, L. Lavoura and J. P. Silva. "Weak magnetic dipole moments in two-Higgs-doublet models". In: *Phys. Rev. D53, 5222 (1996)* (1996).

[39] Kirill Melnikov, Markus Schulze, and Andreas Scharf. "QCD corrections to top quark pair production in association with a photon at hadron colliders". In: *Phys. Rev.* D83 (2011), p. 074013. arXiv: 1102.1967 [hep-ph].

[40] URL: http://home.cern/about/member-states.

[41] URL: https://home.cern/about/experiments.

[42] URL: http://public-archive.web.cern.ch/public-archive/en/About/Nobels-en.html.

[43] URL: https://www.nobelprize.org/nobel_prizes/lists/all/index.html.

[44] URL: http://public-archive.web.cern.ch/public-archive/en/About/Web-en.html.

[45] URL: http://public-archive.web.cern.ch/public-archive/en/About/BasicScience9-en.html.

[46] *Large Hadron Collider Machine*. 2008 JINST 3 S08002 http://iopscience.iop.org/article/10.1088/1748-0221/3/08/S08002/pdf. 2008.

[47] *Large Hadron Collider Machine*. 2008 JINST 3 S08005 http://iopscience.iop.org/article/10.1088/1748-0221/3/08/S08005/pdf. 2008.

[48] Christiane Lefevre. "The CERN accelerator complex." Dec. 2008.

[49] O Adriani et al. *LHCf experiment: Technical Design Report*. Technical Design Report LHCf. Geneva: CERN, 2006.

[50] V Berardi et al. *Total cross-section, elastic scattering and diffraction dissociation at the Large Hadron Collider at CERN: TOTEM Technical Design Report. oai:cds.cern.ch:704349*. Technical Design Report TOTEM. Geneva: CERN, 2004.

[51] *Large Hadron Collider Machine*. 2008 JINST 3 S08001 http://iopscience.iop.org/article/10.1088/1748-0221/3/08/S08001/pdf. 2008.

[52] *Interim Summary Report on the Analysis of the 19 September 2008 Incident at the LHC*. URL: https://edms.cern.ch/ui/file/973073/1/Report_on_080919_incident_at_LHC__2_.pdf.

[53] URL: https://timeline.web.cern.ch/first-lhc-collisions-at-7-tev.

[54] URL: https://timeline.web.cern.ch/lhc-proton-run-for-2011-reaches-successful-conclus

[55] URL: https://timeline.web.cern.ch/record-collision-energy-of-8tev.

[56] URL: https://timeline.web.cern.ch/end-of-lhc-run-1-first-shutdown-begins.

[57] ATLAS Collaboration. *ATLAS Twiki Page: ATLAS Experiment Public Results (Luminosity)*. Jan. 2014. URL: https://twiki.cern.ch/twiki/bin/view/AtlasPublic/LuminosityPublicResults.

[58] *Object selection and calibration, background estimations and MC samples for the Winter 2013 Top Quark analyses with 2012 data*. Tech. rep. ATL-COM-PHYS-2013-088. Geneva: CERN, July 2013.

[59] *Calorimeter clustering algorithms: Description and performance*. Tech. rep. ATL-LARG-PUB-2008-002. Geneva: CERN, May 2008.

[60] Matteo Cacciari, Gavin P. Salam, and Gregory Soyez. "The anti-k_t jet clustering algorithm". In: arXiv:0802.1189v2 [hep-ph] (Apr. 2008).

[61] ATLAS Collaboration. "Jet energy measurement with the ATLAS detector in proton-proton collisions at $\sqrt{s} = 7\,\text{TeV}$". In: arXiv:1112.6426v1 [hep-ex] (Dec. 2011).

[62] *Selection of jets produced in proton-proton collisions with the ATLAS detector using 2011 data*. Tech. rep. ATLAS-CONF-2012-020. Geneva: CERN, Mar. 2012.

[63] URL: https://twiki.cern.ch/twiki/bin/view/AtlasProtected/HowToCleanJets2012.

[64] *Pile-up jet energy scale corrections using the jet-vertex fraction method*. Tech. rep. ATL-COM-PHYS-2009-180. Geneva: CERN, 2009.

[65] Performance of b-jet identification in the ATLAS Experiment. "ATLAS collaboration". In: *JINST 11 P04008 (2016), arXiv:1512.01094 [hep-ex]* ().

[66] *Electron efficiency measurements with the ATLAS detector using the 2012 LHC proton-proton collision data*. Tech. rep. ATLAS-CONF-2014-032. Geneva: CERN, June 2014.

[67] ATLAS Collaboration. *Electron performance measurements with the ATLAS detector using the 2010 LHC proton-proton collision data*. Tech. rep. Eur. Phys. J. C 72 1909. 2012.

[68] ATLAS Collaboration. "Expected Performance of the ATLAS Experiment - Detector, Trigger and Physics". In: arXiv:0901.0512 [hep-ex] (2008).

[69] ATLAS Collaboration. "Measurement of the photon identification efficiencies with the ATLAS detector using LHC Run-1 data". In: *Eur. Phys. J. C* 76 (2016). DOI: 10.1140/epjc/s10052-016-4507-9. arXiv: 1606.01813 [hep-ex].

[70] ATLAS Collaboration. *Electron and photon energy calibration with the ATLAS detector using LHC Run 1 data*. Tech. rep. Eur. Phys. J. C 74 3071. 2014.

[71] Johan Alwall et al. "MadGraph/MadEvent v4: the new web generation". In: 0709 (2007), p. 028. DOI: 10.1088/1126-6708/2007/09/028. arXiv: 0706.2334.

[72] Pumplin, J. and others. "New generation of parton distributions with uncertainties from global QCD analysis". In: *JHEP* 07 (2002), p. 012. arXiv: hep-ph/0201195.

[73] Torbjorn Sjöstrand, Stephen Mrenna, and Peter Z. Skands. "PYTHIA 6.4 Physics and Manual". In: *JHEP* 01 (2004). arXiv: 0603175 [hep-ph]. URL: http://arxiv.org/abs/hep-ph/0603175.

[74] P. Golonka and Z. Was. "PHOTOS Monte Carlo: A Precision tool for QED corrections in Z and W decays". In: *Eur. Phys. J.* C45 (2006), p. 97. DOI: 10.1140/epjc/s2005-02396-4. eprint: hep-ph/0506026.

[75] GEANT4 collaboration, S. Agostinelli et al., "GEANT4, a simulation toolkit". In: *Nucl. Instrum. Meth. A 506 (2003) 250* ().

[76] ATLAS collaboration. "The simulation principle and performance of the ATLAS fast calorimeter simulation FastCaloSim". In: *ATL-PHYS-PUB-2010-013 (2010)* (). URL: https://cds.cern.ch/record/1300517.

[77] T. Gleisberg et al. "Event generation with SHERPA 1.1". In: *JHEP* 0902 (2009).

[78] Carlo Oleari. *The Powheg-Box*. Tech. rep. Nucl.Phys.Proc.Suppl.205-206:36-41. 2010.

[79] Peter Zeiler Skands. *Tuning Monte Carlo Generators: The Perugia Tunes*. Tech. rep. Phys.Rev.D82:074018. 2010.

[80] Gennaro Corcella et al. "HERWIG 6: an event generator for hadron emission reactions with interfering gluons (including supersymmetric processes)". In: *Journal of High Energy Physics* 2001.01 (2001), p. 010. URL: http://stacks.iop.org/1126-6708/2001/i=01/a=010.

[81] J. M. Butterworth, J. R. Forshaw, and M. H. Seymour. *Multiparton Interactions in Photoproduction at HERA. Z. Phys.* Tech. rep. Z. Phys., C72:637-646. 1996.

[82] K. Cranmer et al. ROOT Collaboration. *HistFactory: a tool for creating statistical models for use with RooFit and RooStats*. Tech. rep. Tech. Rep. CERN-OPEN-2012-016, New York U., New York. 2012.

[83] Marcus Rammes. *Measurement of the pp → ttγInclusiveCrossSectioninthesemileptonicDecayChann* 2012.

[84] Oliver Rosenthal. *Evidence and Cross Section Measurement of the processes pp → ttγ at a center-of-mass energy of 7 TeV with the ATLAS experiment*. 2013.

[85] Frederick James. *Statistical Methods in Experimental Physics 2nd edition.* 2006.

[86] W. Verkerke. "Lecture on Practical Statistics at IN2P3 School of Statistics 2014." In: (). URL: https://cds.cern.ch/record/1300517.

[87] *Private communication with Yichen Li.*

[88] *Tracking Reconstruction Performance and Efficiency*. Tech. rep. Geneva: CERN, Oct. 2012. URL: http://atlas.web.cern.ch/Atlas/GROUPS/PHYSICS/IDTRACKING/PublicPlots/ATL-COM-PHYS-2012-1541/.

[89] *Estimation of non-prompt and fake lepton backgrounds in final states with top quarks produced in proton-proton collisions at $\sqrt{s}$ =8 TeV with the ATLAS detector*. Tech. rep. ATL-COM-PHYS-2014-058. Geneva: CERN, 2014.

[90] Duan Peng-Fei et al. "QCD corrections to associated production of $t\bar{t}\gamma$ at hadron colliders". In: (2009). arXiv: 0907.1324 [hep-ph].

[91] Kirill Melnikov, Markus Schulze, and Andreas Scharf. "QCD corrections to top quark pair production in association with a photon at hadron colliders". In: *Phys. Rev.* D83 (2011), p. 074013. arXiv: 1102.1967 [hep-ph].

[92] *Private communication with Mazuza Ghneimat.*

[93] O. Bessidskaia Bylund, F. Maltoni, I. Tsinikos, E. Vryonidou and C. Zhang. *Probing top quark neutral couplings in the Standard Model Effective Field Theory at NLO in QCD*. Tech. rep. JHEP 05 052, arXiv:1601.08193 [hep-ph]. 2016.

Hiermit verschiere ich, dass ich die vorliegende Dissertation selbstständig verfasst und keine anderen als die angegebenen Quellen und Hilfsmittel benuzt, sowie Zitate und Ergebnisse Anderer kenntlich gemacht habe.

Siegen, den 14.06.2017, Naim Bora Atlay